

## REVIEW

View Article Online  
View Journal | View IssueCite this: *J. Mater. Chem. A*, 2018, 6, 23127

## Metal-based nanostructured materials for advanced lithium–sulfur batteries

Juan Balach,<sup>a</sup> Julia Linnemann,<sup>b,c</sup> Tony Jaumann<sup>b</sup> and Lars Giebeler<sup>b</sup>

Since the resurgence of interest in lithium–sulfur (Li–S) batteries at the end of the 2000s, research in the field has grown rapidly. Li–S batteries hold great promise as the upcoming post-lithium-ion batteries owing to their notably high theoretical specific energy density of 2600 W h kg<sup>−1</sup>, nearly five-fold larger than that of current lithium-ion batteries. However, one of their major technical problems is found in the shuttling of soluble polysulfides between the electrodes, resulting in rapid capacity fading and poor cycling stability. This review spotlights the foremost findings and the recent progress in enhancing the electrochemical performance of Li–S batteries by using nanoscaled metal compounds and metals. Based on an overview of reported functional metal-based materials and their specific employment in certain parts of Li–S batteries, the underlying mechanisms of enhanced adsorption and improved reaction kinetics are critically discussed involving both experimental and computational research findings. Thus, material design principles and possible interdisciplinary research approaches providing the chance to jointly advance with related fields such as electrocatalysis are identified. Particularly, we elucidate additives, sulfur hosts, current collectors and functional interlayers/hybrid separators containing metal oxides, hydroxides and sulfides as well as metal–organic frameworks, bare metal and further metal nitrides, metal carbides and MXenes. Throughout this review article, we emphasize the close relationship between the intrinsic properties of metal-based nanostructured materials, the (electro)chemical interaction with lithium (poly)sulfides and the subsequent effect on the battery performance. Concluding the review, prospects for the future development of practical Li–S batteries with metal-based nanomaterials are discussed.

Received 26th July 2018  
Accepted 4th October 2018

DOI: 10.1039/c8ta07220e

rsc.li/materials-a

<sup>a</sup>Department of Chemistry, National University of Río Cuarto-CONICET, Route 36 Km 601, X5804ZAB, Río Cuarto, Argentina. E-mail: jbalach@exa.unrc.edu.ar<sup>b</sup>Leibniz Institute for Solid State and Materials Research (IFW) Dresden e.V., Helmholtzstr. 20, 01069 Dresden, Germany. E-mail: l.giebeler@ifw-dresden.de<sup>c</sup>Chair of Analytical Chemistry II – Electrochemistry & Nanoscale Materials Group, Ruhr-University Bochum, ZEMOS, Universitätsstr. 150, 44801 Bochum, Germany

Juan Balach received his bachelor and Ph.D. degree from National University of Río Cuarto, Argentina, in 2007 and 2011, respectively. After a post-doctoral research stay (2012) in the Department of Colloid Chemistry at the Max Planck Institute of Colloids and Interfaces, Germany, he joined the Leibniz Institute for Solid State and Materials Research (IFW) Dresden, Germany, during

2013–2016. Since 2016, he is a Research Associate of the National Scientific and Technical Research Council (CONICET) at the National University of Río Cuarto. His interests focus on energy materials, including porous nanocarbons and inorganic nanostructured materials for supercapacitors and next-generation batteries: Li–S batteries, Li–air batteries and aqueous batteries.



Julia Linnemann is a research assistant at the Chair of Analytical Chemistry II – Electrochemistry and Nanoscale Materials at the Ruhr-University Bochum, Germany. Supported by the German Academic Scholarship Foundation, she studied chemistry at the Technische Universität (TU) Dresden, Germany and the University of Wollongong, Australia. Following a short-term position at the Project House

Light & Electronics of Evonik Industries in Hsinchu, Taiwan, she received a dissertation fellowship of the German Federal Environmental Foundation in 2015 to conduct a doctoral research project on the electrochemical synthesis of metal–organic materials and films for energy storage applications at the Leibniz Institute for Solid State and Materials Research (IFW) Dresden, Germany.



# 1. Introduction

Our techno-society has crossed the “line of no return” altering traditional lifestyle. The forthcoming technological innovations, which embrace plug-in (hybrid) electric vehicles, aerospace transportation, smart-grid and Internet of Things (IoT) applications, are in relentless pursuit of high-energy rechargeable power sources with reliable/sustainable performance and safety tolerance beyond the state-of-the-art rechargeable lithium-ion (Li-ion) batteries.<sup>1,2</sup>

Undoubtedly, Li-ion battery advances have prompted an unprecedented growth in the portable-power industry. Li-ion battery technologies have been reliant on the usage of intercalation chemistry in transition metal-based lithium containing oxide/phosphate cathodes such as  $\text{Li}(\text{Ni}, \text{Mn}, \text{Co})\text{O}_2$  (NMC),  $\text{Li}(\text{Ni}, \text{Co}, \text{Al})\text{O}_2$  (NCA),  $\text{LiMn}_2\text{O}_4$  (LMO) and  $\text{LiFePO}_4$  (LFP), where their physical constraints in specific energy densities are less than  $400 \text{ W h kg}^{-1}$  on the cell level even with high-energy NMC (811) cathodes and silicon anodes.<sup>3</sup> This energy density is insufficient to meet the upcoming specific energy requirements for “green” electric vehicles and backup energy storage systems capable of coping with the fluctuations of supply from renewable sources (e.g. wind, tidal and solar energies).<sup>2</sup> Furthermore, the aforementioned intercalation-type cathodes present some critical downsides such as high costs and safety concerns that may restrict their further implementation in large-scale power source systems. Therefore, explorations of alternative electrochemical systems which offer higher specific capacity/energy density at low cost are dearly needed for a paradigm change in energy storage due to the ever-increasing demands.

Lithium-sulfur (Li-S) batteries have been touted as one of the most plausible platforms to fulfill the energy demand of tomorrow. The pairing of a high specific capacity lithium anode ( $3800 \text{ mA h g}^{-1}$ ) and sulfur cathode ( $1675 \text{ mA h g}^{-1}$ ) affords a remarkably high theoretical specific energy and volumetric energy of, respectively,  $2600 \text{ W h kg}^{-1}$  and  $2800 \text{ W h L}^{-1}$  (assuming a complete reaction between sulfur and lithium to

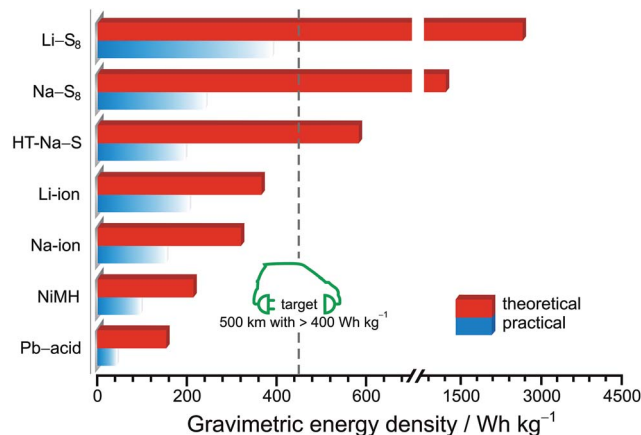


Fig. 1 Schematic comparison of the theoretical and practical gravimetric energy densities of various rechargeable battery systems. Expected mid-class to small electric car range based on reported Tesla Model S and Audi e-tron performances.<sup>11,12</sup> Adapted with permission from ref. 7. Creative Commons Attribution 2.0 International License (<http://creativecommons.org/licenses/by/2.0>).

form lithium sulfide ( $\text{Li}_2\text{S}$ )), outperforming by far existing Li-ion batteries as shown in Fig. 1.<sup>4–7</sup> In addition to its high specific capacity, sulfur as an active cathode material has a low environmental impact and it is daily produced in ton quantities as a by-product of the hydrodesulfurization process in crude-oil refineries, making it abundant and cost-effective for industrial applications on a large scale.<sup>8</sup> While emerging battery companies like Sion Power<sup>9</sup> and Oxis Energy<sup>10</sup> make their first steps in the field of sulfur-based energy systems, the Li-S battery technology faces numerous drawbacks leading to a poor service life that drastically hinders the step towards mass production and large-scale commercialization of the battery.

The overall redox reaction of Li/S coupling can be written as  $\text{S}_8 + 16\text{Li}^+ + 16\text{e}^- \leftrightarrow 8\text{Li}_2\text{S}$ , with the average voltage potential of the full cell being 2.15 V vs.  $\text{Li}/\text{Li}^+$ . However, the total conversion reaction hides a multielectron process with many equilibrium



Tony Jaumann earned his M. Sc. in Chemistry at the TU Dresden in collaboration with the University College London in 2013. He received his doctoral degree at the TU Dresden about silicon anodes in Li-ion and Li-S batteries in 2016. After a post-doctoral stay at the Leibniz Institute for Solid State and Materials Research (IFW) Dresden, Germany, until 2017, he currently works on batteries for industrial applications.



Dr. Lars Giebeler studied chemistry at the Universities of Gießen and Leipzig and received his doctoral degree from the Materials Sciences Institute at TU Darmstadt under supervision of Prof. Hartmut Fieß. After his postdoctoral research at the KU Leuven (Prof. Johan Martens) and at the TU Darmstadt (Prof. Christian Hess), he joined the Leibniz Institute for Solid State and Materials Research (IFW)

Dresden in 2009 and has become group leader in 2011. His research interests focus on active (nanosized) materials for technically relevant applications, operando diffraction and spectroscopy techniques.



reactions between sulfur and lithium polysulfide (LiPS) intermediates of various chain lengths (Fig. 2a).<sup>13</sup> During the initial discharge of the cell, the octet sulfur ( $S_8$ ) in its solid phase is gradually lithiated to form long-chain LiPSs ( $Li_2S_n$ ;  $4 \leq n \leq 8$ ) which are highly soluble in commonly used ether-based electrolytes. In the subsequent discharge process, long-chain LiPSs are reduced to insoluble and poorly conductive  $Li_2S_2$  and  $Li_2S$  species. Essentially, the discharge process described above involves the typical two-step sulfur reduction reactions corresponding to two plateaus in the voltage profile as displayed in Fig. 2b.<sup>14</sup> However, the formation of  $S_3^{\cdot-}$  radicals *via* disproportionation or decomposition reactions of  $S_6^{2-}$  anions has also been proposed.<sup>15</sup> The formation of soluble LiPS intermediates is one of the principal issues in the performance of sulfur-based rechargeable batteries since they are prone to escape out of the cathode scaffold driven by electric field and LiPS concentration gradient forces, leading to the loss of active sulfur material. Furthermore, the dissolved long-chain LiPSs easily diffuse through the polymeric porous separator to the negative electrode and they are reduced to  $Li_2S_2$  and further irretrievably

consumed to form solid  $Li_2S$  at the anode by a spontaneous reaction with metallic lithium, causing lithium anode contamination/passivation, active material loss and increase of cell resistance. The unreacted soluble LiPS species then diffuse back to the cathode side during cell charging and are oxidized again to long-chain LiPSs. This phenomenon generates a constant movement of sulfur species between the two electrodes that is generally known as the “shuttle effect”.<sup>16,17</sup> Although this LiPS shuttling is mainly responsible for the massive degradation of the battery life, there are other critical concerns inherent to the chemical features of sulfur. For instance, the insulating nature of elemental sulfur ( $\sigma = 5 \times 10^{-30} \text{ S cm}^{-1}$  at  $25^\circ\text{C}$ ) constrains its complete utilization. Another problem is the difference in density between sulfur ( $2.03 \text{ g cm}^{-3}$ ) and its reduced discharge product  $Li_2S$  ( $1.67 \text{ g cm}^{-3}$ ) which entails a large volumetric expansion ( $\approx 80\%$ ) during lithiation, leading to the degradation/pulverization of the positive electrode under mechanical strain.<sup>18</sup> Nazar and co-workers developed a breakthrough approach to physically encapsulate sulfur, enhance its redox kinetics and buffer the volumetric expansion of sulfur during lithiation which consists of infiltrating conductive mesoporous carbon with molten sulfur.<sup>19</sup> The encouraging improvements of the cell performance obtained by the encapsulation of sulfur into the pores/cavities of conductive carbon matrices have triggered intensive research on using diverse porous carbon (nano)structures as host matrices (carbon nanoparticles, microporous carbons, mesoporous carbons, hierarchical carbons, carbon spheres, hollow carbon spheres, carbon nanotubes (CNTs), carbon nanofibers (CNFs), graphene, reduced graphene oxide (rGO) and the mix of them).<sup>20–24</sup> However, the solid-to-liquid transformation of the active material and the weak interaction of non-polar pristine carbons with polar LiPSs often lead to the irremediable leak of LiPS species out of the cathode scaffold (specially at areal sulfur loadings higher than  $4 \text{ mg cm}^{-2}$ ),<sup>25</sup> losing the initial intimate contact with the carbon matrix and favoring the agglomeration of  $Li_2S$ /sulfur particles both at the separator/cathode interface and on the anode surface. Especially the latter reaction degrades the performance and the lifespan of the battery. Additionally, recent reviews have given a detailed overview on the functionality of almost all parts of a Li-S battery and how to improve them.<sup>26–30</sup>

The use of additives in ether-based electrolytes,  $LiNO_3$  for example, to form a passivation film on the lithium anode and suppress undesired side reactions,<sup>31,32</sup> the utilization of heteroatom-doped carbons and polymers (*e.g.*: poly(3,4-ethylenedioxythiophene) (PEDOT), polyaniline (PANI) and polypyrrole (PPy)) with combined ionic and electronic conductivity to enhance both physical and chemical confinement of sulfur-based species,<sup>4,33–35</sup> and the addition of conductive porous carbon interlayers between the separator and the cathode to intercept and re-activate migrating LiPS intermediates<sup>36</sup> have also been proven to be viable approaches to enhance the electrochemical performance of Li-S cells. However, these methods in fact retard the diffusion of soluble LiPS species but they do not tackle the root cause. Beyond the conventional encapsulation of active sulfur into porous carbonaceous host matrices, in

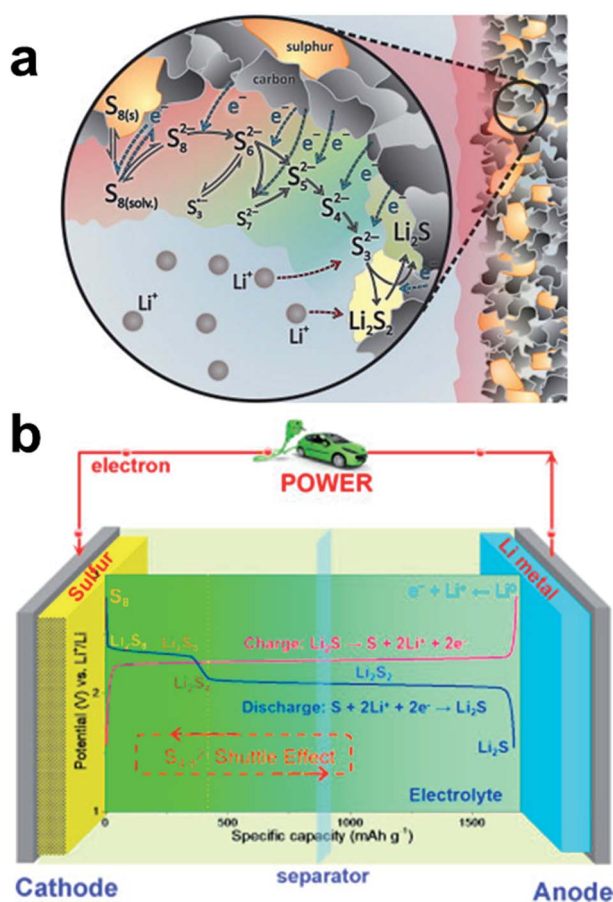


Fig. 2 (a) Stepwise reduction pathway of octet sulfur ( $S_8$ ) to solid  $Li_2S_2$  and  $Li_2S$  products, including intermediate LiPSs ( $Li_2S_n$ ;  $3 \leq n \leq 8$ ).<sup>17</sup> (b) Representative Li-S cell configuration and the characteristic charging/discharging voltage profile based on the stoichiometric redox chemistry between lithium and sulfur.<sup>22</sup> (a) Reproduced with permission from ref. 17. Copyright 2014, Elsevier. (b) Reproduced with permission from ref. 22. Copyright 2015, Elsevier.





the last few years significant advances have been made to address the challenges discussed by using diverse metal-based nanostructured materials with specific chemical affinity to lithium (poly)sulfides.<sup>37,38</sup> Metal-containing compounds with a tailored polar surface have been described as efficient “polar” or “chemisorptive” sulfur host materials to enhance the adsorption of LiPS intermediates, to intensify and achieve faster redox reactions.<sup>39,40</sup> These metal-based compounds can further function as redox mediators<sup>40</sup> possessing the ability to accelerate the kinetics of redox reactions of soluble LiPSs to insoluble  $\text{Li}_2\text{S}_2/\text{Li}_2\text{S}$  and *vice versa*, e.g. by reducing charge transfer resistance.

The scope of this review is to summarize the foremost findings and the recent progress towards achieving high sulfur utilization and long lifespan of Li-S batteries by using additives, sulfur hosts, and functional interlayers/hybrid separators comprising metal-based nanostructured materials, namely metal oxides, metal sulfides, metal-organic frameworks, metals, metal hydroxides, metal nitrides, metal carbides and MXenes. In particular, we emphasize the close relationships between the intrinsic properties of metal-based nanomaterials and the chemical interaction with lithium (poly)sulfides and the subsequent effect on the electrochemical performance of Li-S batteries. In an attempt to provide a guiding route towards the rational design of sulfur cathodes with high practical specific energy, the potential for the future development of practical Li-S batteries with metal-based nanomaterials is discussed.

## 2. Metal oxides

Metal oxides have been used for more than a decade to trap and arrest soluble LiPSs at the positive electrode and thus mitigate the inexorable diffusion of the active material between electrodes. The difference in electronegativity between oxygen and metal atoms induces a strong surface polarity in the metal oxide which serves to effectively interact, or even react *via* a thiosulfate mechanism, with polar LiPS species. The use of metal oxides as additives, sulfur hosts, and components in functional interlayers/hybrid separators as well as the relationship between their intrinsic properties and the electrochemical performance of Li-S cells are described in this section.

### 2.1 Metal oxides as additives

One of the early studies on using metal oxides as additives for improving the performance of Li-S batteries was reported by Ahn and co-workers in 2004.<sup>41</sup> The authors stated that by adding 15 wt% of nanosized  $\text{Mg}_{0.6}\text{Ni}_{0.4}\text{O}$  (particle size  $\approx 50$  nm; surface area  $\approx 8$  m<sup>2</sup> g<sup>-1</sup>) as an additive, the initial specific capacity of the Li-S cells increases by up to 60% in comparison to the cells without the additive (from 741 mA h g<sup>-1</sup> to 1185 mA h g<sup>-1</sup> at 0.1C) due to the improvement of the LiPS adsorption. Despite the initial high capacity achieved by the cell with the  $\text{Mg}_{0.6}\text{Ni}_{0.4}\text{O}$  additive, the capacity steadily decreases to around 1000 mA h g<sup>-1</sup> after 50 cycles revealing a relatively poor LiPS retention.

Later, Ahn and co-workers also used a similar strategy but employing  $\gamma\text{-Al}_2\text{O}_3$  nanoparticles as an additive.<sup>42</sup> By adding 10 wt% of  $\gamma\text{-Al}_2\text{O}_3$  nanoparticles ( $\approx 150$  nm in diameter) to sulfur cathodes (sulfur content = 50 wt%), the cells revealed an increase in specific capacitance (402 mA h g<sup>-1</sup> without the additive vs. 660 mA h g<sup>-1</sup> with the additive at 0.06C). This improvement was attributed to a LiPS adsorption effect between sulfur-related species and the porous  $\gamma\text{-Al}_2\text{O}_3$  nanoparticles.

Zhang *et al.* provided an interesting route to suppress the diffusion of LiPSs and enhance the performance of Li-S batteries by introducing  $\text{Mg}_{0.8}\text{Cu}_{0.2}\text{O}$  nanoparticles (ranging from 20 to 40 nm) into a crystalline  $\text{V}_2\text{O}_5$ /sulfur composite cathode.<sup>43</sup> The composite cathode containing 10 wt% of additive and a sulfur content of  $\approx 38$  wt% showed an initial specific capacity of 545 mA h g<sup>-1</sup> with a capacity retention of 77.5% after 30 cycles at a current density of 0.2 mA cm<sup>-2</sup>, while the cathode without the additive delivered only 227 mA h g<sup>-1</sup> after 30 cycles. The authors claimed that the  $\text{Mg}_{0.8}\text{Cu}_{0.2}\text{O}$  nanoparticles not only have a positive LiPS adsorption effect but also present a catalytic effect to promote the LiPS redox reaction. However, the role of the crystalline  $\text{V}_2\text{O}_5$  used as the sulfur host was not discussed in this study. Although the cyclability was relatively stable, the low sulfur utilization ( $\approx 32\%$ ) still needs to be improved for industrial applications.

Nazar and co-worker also studied the surface adsorption and pore absorption of LiPSs by using high-surface area mesoporous  $\text{SiO}_2$  and  $\text{TiO}_2$  as sorption reagents.<sup>44,45</sup> For instance, Ji *et al.* fabricated a cathode electrode comprised of elemental sulfur (60 wt%), mesoporous carbon (25 wt%), mesoporous silica (SBA-15; 10 wt%) and polyvinylidene difluoride (PVDF) binder (5 wt%) with a sulfur loading of 1.2 mg cm<sup>-2</sup>.<sup>44</sup> The Li-S cell containing SBA-15 demonstrates higher specific capacity and better capacity retention than the cell without the additive. The improved performance of the Li-S system was attributed to the resulting hydrophilic pores of mesoporous silica with Si-O groups which serve as weak binding sites to reversibly adsorb/absorb hydrophilic LiPS intermediates. The retained LiPSs are released near the end of discharge to further reduce them in the pores of the conductive mesoporous carbon network. In this way, the LiPSs remain immobilized in the positive electrode during almost all the discharge process, limiting the LiPS migration to the anode side and keeping the active material available for further utilization.

Subsequently, Evers *et al.* carried out further research studies to optimize the cathode composition by using three different morphologies of mesoporous  $\text{TiO}_2$  (anatase, brookite and rutile phases) as additives.<sup>45</sup> While the LiPS sorption/release mechanism of mesoporous  $\text{TiO}_2$  works in a similar manner to mesoporous  $\text{SiO}_2$ , the higher electropositivity of titania is more effective in adsorbing LiPSs than silica. As a consequence, an improved capacity retention was found for the Li-S cells with  $\alpha\text{-TiO}_2$  (rutile) as the additive (specific surface area = 275 m<sup>2</sup> g<sup>-1</sup>; pore size = 5.2 nm) compared to the cells containing SBA-15 (specific surface area = 918 m<sup>2</sup> g<sup>-1</sup>; pore size = 5.6 nm) at a low amount of additive (3.6 wt%).

Bearing in mind the properties of porous silica to adsorb/absorb soluble LiPS species, Lapornik *et al.* prepared



functionalized zeolite silicalite-1 as a two-in-one additive by integrating  $\text{Mn}_2\text{O}_3$  nanoparticles into a microporous silicate crystal framework (denoted as MnS-1).<sup>46</sup> The cathodes with the functionalized MnS-1 (sulfur content = 50 wt%; sulfur loading =  $2 \text{ mg cm}^{-2}$ ; additive content = 9 wt%) exhibited higher average discharge capacity and lower polarization in comparison to a cathode containing the mesoporous silica SBA-15 additive as a control system. Despite the significant differences in the physical properties (specific surface area, pore size and pore volume) between MnS-1 and SBA-15 additives, the improvement in electrochemical properties was ascribed to the influence of  $\text{Mn}_2\text{O}_3$  nanoparticles in the MnS-1. However, more studies are required to determine the main role if any of the  $\text{Mn}_2\text{O}_3$  in the silicate composite.

Recently, Ponraj *et al.* demonstrated that hydrophilic MgO nanoparticles ( $\approx 50 \text{ nm}$  in diameter) intrinsically functionalized with surface hydroxyl groups can serve as effective additives to capture soluble LiPSs and retain them within the cathode.<sup>47</sup> In comparison to Mn and Ti transition metals, Mg as an alkaline earth metal possesses higher electropositivity, which would aid the chemical binding to LiPS species. As a result of the strong chemical interaction between LiPS intermediates and MgO nanoparticles, sulfur cathodes prepared by simple mixing of elemental sulfur, MgO additive, Super P carbon and PVDF binder (sulfur content = 54–60 wt%; sulfur loading =  $1.8\text{--}2.0 \text{ mg cm}^{-2}$ ; additive content = 10 wt%) showed superior cycling stability, improved discharge capacity and better rate capability compared to cathodes without the additive.

If we consider that LiPS intermediates are heteropolar, an effective LiPS-catching additive should be a compound with polar surface properties. According to innovative work carried out by Xie *et al.*, the utilization of ferroelectric  $\text{BaTiO}_3$  nanoparticles with “spontaneous polarization” could solve the shuttle effect by trapping LiPS species owing to the induced charges on the surface of  $\text{BaTiO}_3$  nanoparticles.<sup>48</sup> In fact, the hollow carbon nanospheres/sulfur cathode with  $\text{BaTiO}_3$  nanoparticles (sulfur content = 42 wt%; sulfur loading =  $2.4 \text{ mg cm}^{-2}$ ) showed a notable improvement in the delivered capacity compared with its counterpart cathode without  $\text{BaTiO}_3$  ( $835 \text{ mA h g}^{-1}$  vs.  $407 \text{ mA h g}^{-1}$  after 100 cycles, respectively). However, the cells with the  $\text{BaTiO}_3$  additive also present a clear capacity fading during the initial cycles at a low current rate, usually observed in systems with polysulfide leakage.

Although the incorporation of metal oxide additives could be presented as a simple and straightforward method to improve both the specific capacity and lifespan of Li-S batteries, the noticeable and irreversible capacity decay reported in the aforementioned systems also indicates that the LiPS dissolution into the electrolyte still occurs, giving the possibility to LiPSs to diffuse out of the sulfur cathode and migrate to the lithium anode. Therefore, an alternative and more effective methodology to fully restrict the active sulfur material in the positive electrode is needed.

## 2.2 Metal oxides as sulfur host cathodes

The early research on the use of metal oxides as additives gave the kick start to highlight the notable properties of these metal

compounds to retain LiPSs at the cathode by chemical binding and hence improve the stability and performance of the positive electrode. Metal oxides with a certain structure and porosity can provide a dual function by serving as a sole sulfur host to accommodate the active material into their cavities/pores and also facilitating the chemisorption of formed soluble LiPS intermediates. In this regard, Cui and co-workers pioneered the utilization of  $\text{TiO}_2$  as a unique support to encapsulate sulfur for positive electrodes.<sup>49</sup> The cathode composite in question consists of a sulfur- $\text{TiO}_2$  yolk-shell structure with internal void space which possess the advantage of both enclosing the active material into the inner cavity and affording adequate space for alleviating the large volume changes of sulfur through cycling. To prepare the yolk-shell architecture, sulfur particles (800 nm) resulting from the reaction between  $\text{Na}_2\text{S}_2\text{O}_3$  and HCl were coated with a thin layer of  $\text{TiO}_2$  (15 nm) *via* alkaline hydrolysis of a titanium diisopropoxide bis(acetylacetonate) precursor, followed by a moderate sulfur dissolution with toluene to finally form the internal void space. Compared to a sulfur- $\text{TiO}_2$  core-shell (with no free internal space) and uncoated sulfur composite structures, the cathode with the sulfur- $\text{TiO}_2$  yolk-shell design (sulfur content  $\approx 53 \text{ wt\%}$ ; sulfur loading  $\approx 0.5 \text{ mg cm}^{-2}$ ) showed a high capacity retention with a capacity decay of 0.033% per cycle after 1000 cycles. The long lifespan was principally attributed to the intact integrity of the  $\text{TiO}_2$  shell, serving as an effective reservoir to retain sulfur compounds.  $\text{TiO}_2$ -based host materials with different structures have also been explored in order to promote sulfur utilization, prevent cathode degradation and enhance the kinetics of the Li/S redox reaction.<sup>50–52</sup> For example, Xie *et al.* embedded molten sulfur into/onto  $\text{TiO}_2$  nanotubes to finally produce a  $\text{TiO}_2$ /sulfur composite cathode (sulfur content  $\approx 45 \text{ wt\%}$ ; sulfur loading  $\approx 1.1 \text{ mg cm}^{-2}$ ), enabling a stable reversible capacity of  $851 \text{ mA h g}^{-1}$  after 100 cycles at a C-rate of 0.2 and a resultant capacity degradation of 0.068% per cycle.<sup>53</sup> To improve the ability of  $\text{TiO}_2$  to chemically immobilize sulfur-based species, Yang *et al.* prepared hydrogen reduced  $\text{TiO}_2$  microspheres as a promising host material.<sup>54</sup> The functionalized  $\text{TiO}_2$  microspheres with an increased polar surface area due to oxygen vacancies created during a mild hydrogenation process serve as surface-bound intermediates to strongly bind LiPSs. The resulting cathode (sulfur content  $\approx 40 \text{ wt\%}$ ; sulfur loading =  $0.8\text{--}1.3 \text{ mg cm}^{-2}$ ) showed a capacity of  $928 \text{ mA h g}^{-1}$  after 50 cycles at a current density of  $200 \text{ mA g}^{-1}$ , corresponding to a capacity degradation of 1.99% per cycle. Although the cycling performance was relatively stable, the lifespan of 50 cycles needs to be improved.

$\text{TiO}_2$  has proven to restrict the active material loss due to the adsorption effect of LiPSs. However, the semiconducting nature of  $\text{TiO}_2$  also lessens the conductivity of the cathode. To circumvent this hurdle, Nazar and co-workers<sup>54</sup> as well as Cui and co-workers<sup>55</sup> suggested almost at the same time to use the highly conducting Magnéli phase  $\text{Ti}_4\text{O}_7$  as a sulfur host material. The structure of metallic conductive Magnéli  $\text{Ti}_4\text{O}_7$  ( $\approx 2 \times 10^3 \text{ S cm}^{-1}$ )<sup>56</sup> is comprised of two-dimensional shear planes of Ti-O octahedral with polar O-Ti-O units, which can function as LiPS anchor sites (Fig. 3a). Nazar and co-workers prepared Magnéli  $\text{Ti}_4\text{O}_7$  by heating a titanium ethoxide-polyethylene



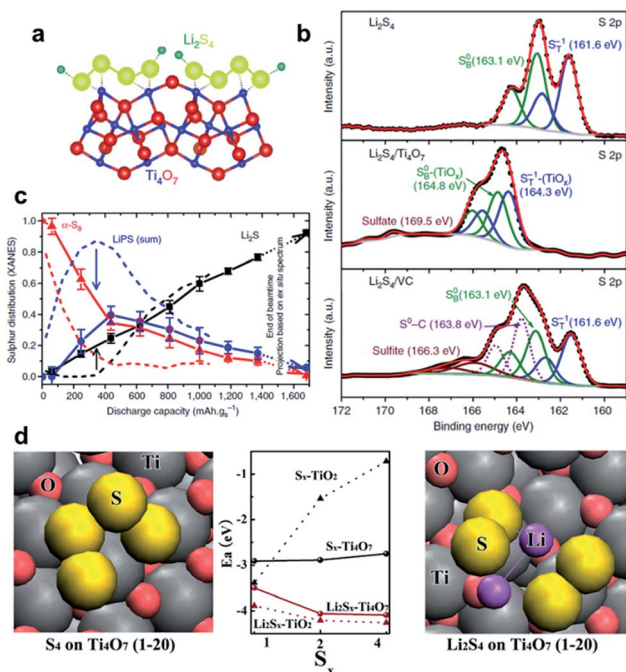


**Fig. 3** Magnéli titanium oxide as a sulfur host for Li-S batteries. (a) A schematic illustration of the electron density transfer between  $\text{TiO}_x$  and  $\text{Li}_2\text{S}_4$  (green = Li, yellow = S, blue = Ti, and red = O).<sup>54</sup> (b) High-resolution S 2p XPS spectra of  $\text{Li}_2\text{S}_4$  (top),  $\text{Li}_2\text{S}_4/\text{Ti}_4\text{O}_7$  (middle), and  $\text{Li}_2\text{S}_4/\text{VC}$  carbon (bottom). Black dotted line = experimental data, red line = fitted data, and solid/dotted lines in other colors = fitted individual components.<sup>54</sup> (c) Operando XANES results showing the distribution of sulfur species upon discharge for Li-S cells with  $\text{Ti}_4\text{O}_7/\text{S}-60$  (solid lines + symbols) and VC carbon/S-60 cathodes (dashed lines).  $\text{Ti}_4\text{O}_7/\text{S}-60$  presents a lower concentration of LiPS compared with VC carbon/S-60. Black =  $\text{Li}_2\text{S}$ ; blue = LiPS showed as the sum of  $\text{Li}_2\text{S}_6$  and  $\text{Li}_2\text{S}_4$ ; red = elemental sulfur.<sup>54</sup> (d) DFT optimized structures and adsorption energies of sulfur species on  $\text{Ti}_4\text{O}_7$  (1-20) and  $\text{TiO}_2$  (110) surfaces. Gray = Ti; pink = O; yellow = S; purple = Li.<sup>55</sup> (a-c) Reproduced with permission from ref. 54. Copyright 2014, Nature Publishing Group. (d) Reproduced with permission from ref. 55. Copyright 2014, American Chemical Society.

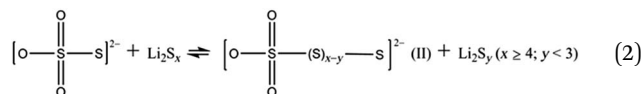
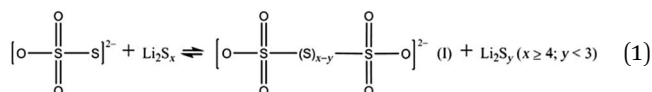
glycol mixture at 950 °C under an argon atmosphere.<sup>54</sup> X-ray diffraction investigation and elemental microanalysis revealed that the obtained sample is composed of  $\text{Ti}_4\text{O}_7$  as the primary crystalline phase together with 15.4 wt% of residual amorphous carbon. The  $\text{Ti}_4\text{O}_7$  sample also has a relatively high conductivity of  $\approx 3.2 \text{ S cm}^{-1}$  and a high specific surface area of  $290 \text{ m}^2 \text{ g}^{-1}$ , which are essential for electron/ $\text{Li}^+$ -ion transport and interfacial interaction with LiPSs, respectively. After melt-infiltration of sulfur, the  $\text{Ti}_4\text{O}_7$ -sulfur composite cathode (sulfur content = 48 wt%; sulfur loading  $\approx 0.825 \text{ mg cm}^{-2}$ ) provided an initial specific capacity of  $1070 \text{ mA h g}^{-1}$  with a reasonable capacity degradation of 0.08% per cycle after 250 cycles at 0.5C. This fade rate is half of the capacity degradation obtained for a cell with a Vulcan XC72 carbon-sulfur composite cathode used as a reference. Further X-ray photoelectron spectroscopy (XPS) and *in situ* X-ray absorption near-edge spectroscopy (XANES) studies determined that  $\text{Ti}_4\text{O}_7$  has a strong effect on decreasing the LiPS concentration in solution and also controls the gradual deposition of  $\text{Li}_2\text{S}$  onto  $\text{Ti}_4\text{O}_7$  particles *via* surface-mediated

reduction at the interface (Fig. 3b and c). This phenomenon electrocatalytically enhances the redox reaction of LiPSs and, thus, improves the overall electrochemical performance of the cells. On the other hand, Cui and co-workers synthesized semiconducting  $\text{Ti}_6\text{O}_{11}$  nanowires and metallic  $\text{Ti}_4\text{O}_7$  nanoparticles as oxygen-deficient  $\text{Ti}_n\text{O}_{2n-1}$  Magnéli phases by heating rutile  $\text{TiO}_2$  at, respectively, 950 and 1050 °C under a pure reducing hydrogen atmosphere.<sup>55</sup> In order to study the electronic conductivity effect of the Ti-based scaffolds on the cell performance,  $\text{TiO}_2$ -,  $\text{Ti}_6\text{O}_{11}$ -, and  $\text{Ti}_4\text{O}_7$ -sulfur composites were prepared by sulfur impregnation of the host samples and further heating at 155 °C in a vacuum oven. As a consequence of the highest conductivity of  $\text{Ti}_4\text{O}_7$  (relative conductivity order:  $\text{Ti}_4\text{O}_7 > \text{Ti}_6\text{O}_{11} > \text{TiO}_2$ ), the Li-S cells with  $\text{Ti}_4\text{O}_7$ -sulfur composite cathodes (sulfur content  $\approx 51 \text{ wt\%}$ ; sulfur loading =  $1-3 \text{ mg cm}^{-2}$ ) showed the best cycling performance with an initial capacity of  $1044 \text{ mA h g}^{-1}$  and an outstanding capacity retention of 99% over 100 cycles at 0.1C, which correspond to one of the lowest capacity degradation values (0.01% per cycle) reported so far.<sup>57-59</sup> Further density functional theory (DFT) calculations combined with XPS studies determined that the low-coordinated Ti sites of  $\text{Ti}_4\text{O}_7$  highly favor the adsorption of sulfur-based intermediates and selective  $\text{Li}_2\text{S}$  deposition (Fig. 3d). Therefore, Li-S cells with superior performance can be achieved by combining the unique polar surface and the inherent electronic conductivity of  $\text{Ti}_4\text{O}_7$  for, respectively, strong LiPS binding and kinetically enhanced redox electron transfer.<sup>54,55</sup>

More recently, Wei *et al.* proposed a cathode scaffold for Li-S batteries based on mesoporous Magnéli  $\text{Ti}_4\text{O}_7$  microspheres.<sup>60</sup> The relatively high surface area ( $197 \text{ m}^2 \text{ g}^{-1}$ ) and the interconnected mesopores (20.4 nm) of the Magnéli  $\text{Ti}_4\text{O}_7$  microspheres are able to accommodate up to 70 wt% of sulfur into their inorganic matrix. The ensuing  $\text{Ti}_4\text{O}_7$  microspheres/sulfur cathodes (sulfur content = 56 wt%; sulfur loading  $\approx 0.5 \text{ mg cm}^{-2}$ ) showed a high discharge capacity of  $1318 \text{ mA h g}^{-1}$  at a C-rate of 0.1 and a stable cyclability comprising a capacity degradation of 0.03% per cycle over 400 cycles at a rate of 0.2C.

Motivated by the interesting properties of metal oxides and aiming for a more effective material to catalyze the LiPS redox reaction, Nazar and co-workers were the first group to develop ultra-thin  $\delta\text{-MnO}_2$  nanosheets as a host material to confine LiPS intermediates at the cathode side by specific chemical interactions.<sup>61</sup> Based on XPS studies the authors established that, at the beginning of the discharge process,  $\text{MnO}_2$  nanosheets have the ability to oxidize the initially reduced higher-order LiPSs to thiosulfate groups at the surface of the host material. As the reduction process continues, the newly formed and soluble long-chain LiPSs are moored to the surface thiosulfate groups ( $\text{S}_2\text{O}_3^{2-}$ ) which serve as transfer mediators to form a slightly soluble, intermediate polythionate complex (I) and insoluble short-chain LiPSs (*i.e.*,  $\text{Li}_2\text{S}_2$  or  $\text{Li}_2\text{S}$ ) *via* an internal disproportionation reaction (eqn (1)). It is worth mentioning that a polythiosulfate complex (II) could also be generated through a similar reaction (eqn (2)).<sup>62,63</sup>





The authors suggested that the formation of the surface-bound polythionate complex lessens the active material loss during cycling by the early induced disproportionation conversion of higher-order LiPS intermediates to insoluble lower-order LiPS species. A visual confirmation of LiPS entrapment obtained at different depths of discharge further evidenced the strong affinity of  $\text{MnO}_2$  to sulfur-based species (Fig. 4d). At the end of discharge (after 12 h), the electrolyte solution of the optically accessible cell with a  $\text{MnO}_2$ -sulfur cathode presents a pale yellow color, while the solution of the cell in the absence of  $\text{MnO}_2$  turned bright greenish yellow due to solubilized LiPSs in the electrolyte (Fig. 4c). As a result,  $\text{MnO}_2$ -

containing cathodes (sulfur content  $\approx 56$  wt%; sulfur loading =  $0.7\text{--}1.0 \text{ mg cm}^{-2}$ ) demonstrated a high electrochemical performance with a low capacity decay rate of 0.032% per cycle over 2000 cycles at 2C (Fig. 4e).

Analogous to a sulfur-TiO<sub>2</sub> yolk-shell structure,<sup>49</sup> Liang *et al.* synthesized sulfur-MnO<sub>2</sub> yolk-shell composite cathodes by a mild redox reaction between sulfur and  $\text{KMnO}_4$  in an aqueous solution at room temperature, followed by a partial dissolution of the sulfur core with toluene.<sup>64</sup> The resultant high-performance cathodes with spherical-like sulfur particles (around 300–400 nm) and improved sulfur loading (sulfur content  $\approx 64$  wt%; sulfur loading  $\approx 1.6 \text{ mg cm}^{-2}$ ) demonstrated that it is possible to reach a high initial capacity of  $1380 \text{ mA h g}^{-1}$  at a low rate of 0.05C (82% of the theoretical capacity) and a reversible capacity of  $315 \text{ mA h g}^{-1}$  after 1700 cycles at 2C, being equivalent to a low capacity decay of 0.039% per cycle. This notable cell performance was ascribed to the distinctive features of the  $\text{MnO}_2$  shell to intrinsically adsorb LiPS species and chemically bind them by *in situ* formation of thiosulfate/polythionate groups as well as to the physical confinement provided by the yolk-shell nano-architecture.<sup>49,61</sup> Since the  $\text{KMnO}_4$  precursor used for producing  $\text{MnO}_2$  is less expensive than typical Ti-based precursors used for

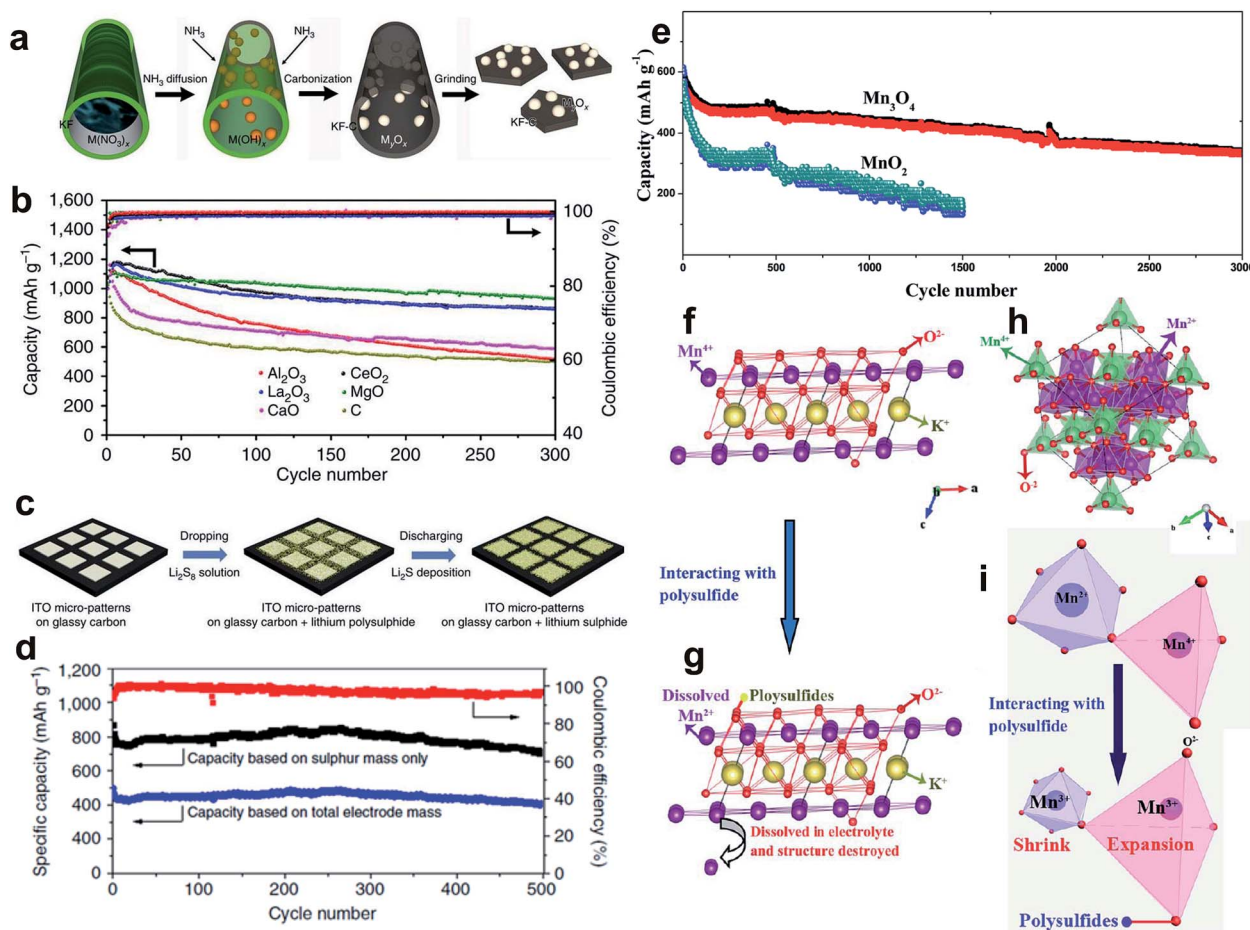


Fig. 4 Visual confirmation of LiPS trapping at different depths of discharge for (a) sulfur-Ketjen black and (b) sulfur-MnO<sub>2</sub> cells.<sup>61</sup> (c) Long-term cycling performance of the sulfur-MnO<sub>2</sub> nanosheet composite cathode.<sup>61</sup> (a–c) Reproduced with permission from ref. 61. Copyright 2015, Nature Publishing Group.

TiO<sub>2</sub>/Ti<sub>4</sub>O<sub>7</sub>, the proposed MnO<sub>2</sub>–sulfur composite cathode could be viable for large-scale production and practical application in Li–S batteries.

Wang *et al.* investigated the interaction of MnO<sub>2</sub> with octahedral sulfur and various Li<sub>2</sub>S<sub>n</sub> intermediates (with  $n = 1, 2, 4, 6$  and  $8$ ) by using theoretical calculations.<sup>65</sup> The authors found that even the fresh cathode forms relatively weak S=O chemical bonds between terminal S atoms from the opened S<sub>8</sub> ring and O atoms on the MnO<sub>2</sub> surface, while linear LiPS intermediates, formed upon lithiation, present stronger chemical bonds as a consequence of additional Li–O chemical bonds. Interestingly, due to the poor stability of Li<sub>2</sub>S, the subsequent decomposition into S and Li atoms with S=O and Li–O bonds was predicted after full lithiation of sulfur. However, this phenomenon has not been experimentally detected.

To shed light on the fundamental surface mechanism involved between metal oxides and sulfur species and further understand its correlation with the Li–S cell stability, Liang *et al.* conducted a series of electrochemical studies using high surface area transition metal oxides—Fe<sub>2</sub>O<sub>3</sub>, Co<sub>3</sub>O<sub>4</sub>, V<sub>2</sub>O<sub>3</sub>, NiO, Cu<sub>2</sub>O, CuO, CoO, VO<sub>2</sub>, MnO<sub>2</sub>, V<sub>2</sub>O<sub>5</sub> and NiOOH—to adsorb and/or activate (poly)sulfide intermediates *via* thiosulfate formation.<sup>66</sup> By combining cyclic voltammetry and surface spectroscopy studies, it was possible to elucidate that metal oxides with redox potentials between  $2.4 \text{ V} < E < 3.2 \text{ V}$  vs. Li/Li<sup>+</sup> oxidize LiPSs to active thiosulfate (such as CuO, VO<sub>2</sub> and MnO<sub>2</sub>) and those oxides with potentials higher than  $3.2 \text{ V}$  vs. Li/Li<sup>+</sup> (*e.g.* V<sub>2</sub>O<sub>5</sub> and NiOOH) additionally over-oxidize LiPSs to inactive sulfate, while metal oxides with redox potentials lower than  $2.1 \text{ V}$  vs. Li/Li<sup>+</sup> (Fe<sub>2</sub>O<sub>3</sub>, Co<sub>3</sub>O<sub>4</sub>, V<sub>2</sub>O<sub>3</sub>, NiO, Ti<sub>4</sub>O<sub>7</sub>, Cu<sub>2</sub>O, CoO and TiO<sub>2</sub>) only bind LiPSs by polar interactions rather than by oxidation of LiPS intermediates (Fig. 5a). To provide a proof-of-concept, three metal oxide–graphene-based sulfur cathodes (sulfur content = 60 wt%; sulfur loading around  $1.2\text{--}1.5 \text{ mg cm}^{-2}$ ) containing Co<sub>3</sub>O<sub>4</sub>, VO<sub>2</sub> and V<sub>2</sub>O<sub>5</sub> with different redox potentials (1.11, 2.79

and  $3.40 \text{ V}$  vs. Li/Li<sup>+</sup>, respectively) were electrochemically compared under long-term cycling tests (Fig. 5b). After 280 cycles at a C-rate of 0.5, the cell with a sulfur/VO<sub>2</sub>–graphene cathode displays the best cycling performance compared to sulfur/V<sub>2</sub>O<sub>5</sub>–graphene and sulfur/Co<sub>3</sub>O<sub>4</sub>–graphene cathodes. Unlike VO<sub>2</sub>, V<sub>2</sub>O<sub>5</sub> not only oxidizes LiPSs to thiosulfate/polythionate but also forms electrochemically inactive sulfate species which obstruct the access to the host surface and thereby lessen the reversible oxidation/reduction of active sulfur intermediates. In contrast, the sulfur/Co<sub>3</sub>O<sub>4</sub>–graphene exhibits the lowest capacity retention due to the lack of thio-sulfate/polythionate formation and actually the cell failed after 250 cycles. Furthermore, the authors demonstrated that the side sulfate formation could be avoided by restricting the charge potential to  $2.5 \text{ V}$  instead of the initially used  $3.0 \text{ V}$ . Further theoretical studies performed by Zhang *et al.* revealed that the resulting strong chemical bonds between V<sub>2</sub>O<sub>5</sub> and Li<sub>2</sub>S<sub>4</sub> can induce the destruction/decomposition of the Li<sub>2</sub>S<sub>4</sub> compound, lessening the capacity retention of the Li–S cell.<sup>67</sup> This theoretical observation correlates well with the above experimental results described for V<sub>2</sub>O<sub>5</sub>.<sup>66</sup>

Metal oxides, such as TiO<sub>2</sub>, Ti<sub>4</sub>O<sub>7</sub>, VO<sub>2</sub> and MnO<sub>2</sub>,<sup>68–71</sup> were proved to be an efficient intermediary to limit the dissolution of LiPSs through chemical interactions due to their polar properties. However, there are other oxides that have been considered as sulfur host materials with the aim to improve the stability of Li–S batteries, such as SiO<sub>2</sub>,<sup>72,73</sup> Mg<sub>0.6</sub>Ni<sub>0.4</sub>O,<sup>74,75</sup> CoO,<sup>76</sup> Co<sub>3</sub>O<sub>4</sub>,<sup>77,78</sup> NiCo<sub>2</sub>O<sub>4</sub>,<sup>79</sup> and MoO<sub>2</sub>.<sup>80</sup> As an example, Qu *et al.* proposed conductive, mesoporous MoO<sub>2</sub> as a sulfur-hosting oxide to enhance the performance of Li–S cells.<sup>80</sup> Combining the high conductivity and the physical properties of MoO<sub>2</sub> (relative conductivity  $\approx 190 \text{ S cm}^{-1}$ ;<sup>81</sup> surface area =  $70 \text{ m}^2 \text{ g}^{-1}$ ; pore size  $\approx 12 \text{ nm}$ ) together with the ability of the oxide to anchor LiPSs *via* strong S–O binding interactions, the sulfur-infiltrated mesoporous MoO<sub>2</sub> cathode (sulfur content = 30.4 wt%; sulfur loading  $\approx 1 \text{ mg cm}^{-2}$ ) exhibited a reversible capacity of  $570 \text{ mA h g}^{-1}$  after 250 cycles at a C-rate of 0.1C, which corresponds to a capacity decay rate of 0.19% per cycle. While conductive MoO<sub>2</sub> could be a promising oxide to limit the shuttle effect and activate sulfur species, the upsurges of both sulfur content and sulfur loading are highly required for practical cells.

While metal oxide-based host cathodes are very promising to confine LiPSs species and avoid their leak to the anode side, these materials still present some concerns in terms of their inherent low electrical conductivity and high relative density.

### 2.3 Metal oxide/porous carbon hybrid scaffolds

Metal oxide-derived host materials capable of binding LiPSs through chemical interactions are, indeed, very promising candidates for enhancing the stability and electrochemical properties of Li–S batteries. However, their general insulating nature and high relative density drastically decrease the capacity retention and energy density of the cells, respectively, when they are used as sole sulfur host materials. It is worth mentioning that in spite of using metal oxide materials as unique supports to store sulfur, most of the studies described in

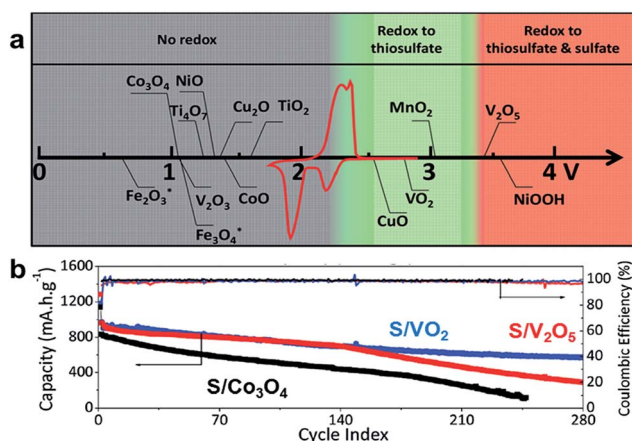


Fig. 5 (a) Chemical reactivity of different metal oxides with LiPSs displayed as a function of the redox potential vs. Li/Li<sup>+</sup>.<sup>66</sup> (b) Comparison of the cycling performance at 0.5C for S/V<sub>2</sub>O<sub>5</sub>/graphene (red), S/VO<sub>2</sub>/graphene (blue), and S/Co<sub>3</sub>O<sub>4</sub>/graphene (black) cathodes.<sup>66</sup> (a and b) Reproduced with permission from ref. 66. Copyright 2015, Wiley-VCH.





Subsection 2.2 also utilized some conductive additives (*e.g.* carbon black). A more attractive approach to effectively encapsulate sulfur without compromising the conductivity of the cathode matrix could be the integration of metal oxides into conductive and (porous) carbonaceous materials. In the last few years, several studies have shown improvements of the cathode performance by modifying all types of conductive carbon substrates (*i.e.* carbon black, CNTs, CNFs, graphene, rGO, porous carbons, heteroatom-doped carbons, *etc.*)<sup>24,82</sup> with diverse metal oxides, such as  $\text{La}_2\text{O}_3$ ,<sup>83,84</sup>  $\text{SiO}_2$ ,<sup>85–87</sup> indium tin oxide (ITO),<sup>88</sup>  $\text{TiO}_2$ ,<sup>89–98</sup>  $\text{TiO}$ ,<sup>99,100</sup>  $\text{Ti}_4\text{O}_7$ ,<sup>101</sup>  $\text{MnO}_2$ ,<sup>102–112</sup>  $\text{Mn}_3\text{O}_4$ ,<sup>59,113</sup>  $\text{MgO}$ ,<sup>84,114</sup>  $\text{VO}_2$ ,<sup>115</sup>  $\text{V}_2\text{O}_3$ ,<sup>116</sup>  $\text{Co}_3\text{O}_4$ ,<sup>117</sup>  $\text{CeO}_2$ ,<sup>84,118,119</sup>  $\text{ZrO}_2$ ,<sup>120–122</sup>  $\text{Nb}_2\text{O}_5$ ,<sup>123</sup>  $\text{SnO}_2$ ,<sup>124</sup>  $\text{ZnO}$ ,<sup>125,126</sup>  $\alpha\text{-Fe}_2\text{O}_3$ ,<sup>127</sup>  $\text{Fe}_3\text{O}_4$ ,<sup>128</sup>  $\text{NiO-NiCo}_2\text{O}_4$ ,<sup>129</sup>  $\text{NiFe}_2\text{O}_4$ ,<sup>58</sup>  $\text{MoO}_2$ ,<sup>130</sup>  $\text{MoO}_3$ ,<sup>131</sup>  $\text{Mo}_4\text{O}_{11}$ ,<sup>132</sup>  $\text{Al}_2\text{O}_3$ ,<sup>84</sup>  $\text{CaO}$ ,<sup>84</sup>  $\text{Y}_2\text{O}_3$ ,<sup>133</sup> and  $\text{Nd}_2\text{O}_3$ ,<sup>134</sup> and complex perovskites like  $\text{Ba}_{0.5}\text{Sr}_{0.5}\text{Co}_{0.8}\text{Fe}_{0.2}\text{O}_{3-\delta}$ .<sup>135</sup> Table 1 summarizes the most significant studies on metal oxide–conductive carbon composites used as sulfur host materials for Li–S batteries in terms of sulfur cathode parameters (sulfur content and areal sulfur loading) and electrochemical performance.

In general, the use of an insulating material (*i.e.*, metal oxides) should increase the resistance of the electrode due to a deficiency in electron transport. Actually, if the metal oxide has the ability to strongly trap insulating LiPS species, it is expected to encounter an accumulation in electronically inactive zones which should reduce the utilization of the active material

and also the capacity retention. However, despite the insulating nature of most metal oxides, several studies have reported significant improvements in the electrochemical performance of ternary metal oxide/carbon/sulfur electrodes compared with conventional sulfur/carbon composite electrodes. Therefore, the initially adsorbed LiPSs should be later transferred from the oxide surface to the conductive substrate to finally undergo the electrochemical reaction. Intrigued by this observation, Cui and co-workers studied the competitive processes of adsorption of LiPS species on oxides and diffusion of LiPSs from the oxide surface to the conductive carbon matrix.<sup>84</sup> To fabricate the oxide/porous carbon flake nanostructures, Kapok tree fibers (KFs) were used as both the bio-template and carbon source (Fig. 6a). While various nonconductive oxides were used in this study, the MgO- and  $\text{La}_2\text{O}_3$ -containing carbon material/sulfur composite electrodes showed the best electrochemical performance with high capacities and good capacity retention over 300 cycles (Fig. 6b). As an oxide selection criterion for the design of LiPSs/oxide interfaces for advanced Li–S batteries, the authors proposed polar sulfur hosts with strong binding to LiPS intermediates, a high surface area and, preferably, good surface diffusion properties. An interesting approach in terms of high performance and long cycling stability at high sulfur loading ( $>3 \text{ mg cm}^{-2}$ ) was reported by Yao *et al.* They used conductive tin-doped indium oxide—also well known as ITO—nanoparticles to decorate a carbon nanofiber (CNF) host material (Fig. 6c).<sup>88</sup> For

**Table 1** Summary of the most significant studies on metal oxide–conductive carbon composites as sulfur host materials for Li–S batteries

Metal oxide–conductive carbon	Initial capacity [mA h g <sup>−1</sup> ]	Reversible capacity [mA h g <sup>−1</sup> ]	Current rate <sup>a</sup>	Cycle number	Degradation rate per cycle [%]	Sulfur content <sup>b</sup> [wt%]	Sulfur loading [mg cm <sup>−2</sup> ]	Ref.
$\text{La}_2\text{O}_3/\text{N-doped meso-carbon}$	1241	≈ 880 <sup>c</sup>	0.2C	100	≈ 0.291 <sup>c</sup>	48	N/A	83
$\text{La}_2\text{O}_3\text{-Kapok tree fibers}$	1013 <sup>c</sup>	870 <sup>c</sup>	0.5C	300	0.047	63–70	0.7–1.2	84
$\text{SiO}_2\text{-mildly reduced GO}^d$	≈ 1425 <sup>c</sup>	763	0.1C	50	≈ 0.929 <sup>c</sup>	N/A	N/A	72
ITO-carbon nanofiber mat	1136	1000	0.2C	300	0.040	40	2.0	88
ITO-carbon nanofiber mat	866	710	0.2C	500	0.036	57	4.0	88
$\text{TiO}_2$ nanowire-graphene	N/A	1053	0.2C	200	N/A	62	3.2	89
Hollow carbon nanofiber@ $\text{TiO}_2$	1040	650	0.5C	200	0.187	54	1.6	90
Hollow carbon nanofiber@ $\text{TiO}_2$	970	380	1C	500	0.122	54	1.6	90
$\text{TiO}_2/\text{graphene}$	871	732	1C	400	0.040	44	1.0	91
$\text{TiO}_2/\text{N-doped graphene}$	1069	918	1C	500	0.028	59	1.3–1.8	92
$\text{TiO@hollow carbon spheres}$	1066	630	0.5C	500	0.082	56	1.5	99
$\text{MnO}_2/\text{hollow carbon fibers}$	1147	≈ 840 <sup>c</sup>	0.2C	100	≈ 0.268 <sup>c</sup>	50	3.5–3.9	102
$\text{MnO}_2\text{-GO-CNTs}^e$	1150	964	0.2C	100	0.162	64	2.8	104
$\text{Mn}_3\text{O}_4\text{-carbon cloth}$	593	355	2C	3000	0.013	≈ 62	2.8	59
MgO-Kapok tree fibers	≈ 1035 <sup>c</sup>	≈ 930 <sup>c</sup>	0.5C	300	0.034	63–70	0.7–1.2	84
$\text{V}_2\text{O}_3\text{-carbon microspheres}$	1177	921	0.5C	100	0.217	≈ 45	1.5–1.6	116
$\text{CeO}_2/\text{Ketjen black carbon}$	905	710	1C	300	0.072	60	N/A	118
$\text{Nb}_2\text{O}_5\text{-meso-carbon}$	1289	913	0.5C	200	0.146	48	1.5	123
$\text{Mo}_4\text{O}_{11}\text{-graphene}^f$	≈ 1190 <sup>c</sup>	≈ 880 <sup>c</sup>	0.1C	80	≈ 0.323 <sup>c</sup>	49	0.5	132
$\alpha\text{-Fe}_2\text{O}_3/\text{graphene}$	≈ 670 <sup>c</sup>	≈ 370 <sup>c</sup>	2C	500	0.090	48	0.6	127
Yolk-shell carbon@ $\text{Fe}_3\text{O}_4$	1104	855	0.1C	200	0.113	64	5.5	128
$\text{ZrO}_2\text{-holey CNTs}$	1138	878	0.5C	200	0.114	36	N/A	121
$\text{NiFe}_2\text{O}_4\text{-CNTs}$	890	850	1C	500	0.009	54.7	1.0–1.2	58
$\text{Nd}_2\text{O}_3\text{-RFC}^g$	1168	907	0.5C	300	0.074	44.6	2.2–3.0	134
$\text{Ba}_{0.5}\text{Sr}_{0.5}\text{Co}_{0.8}\text{Fe}_{0.2}\text{O}_{3-\delta}/\text{CNT}$	793	632	0.5C	400	0.062	70	2.6–5.3	135

<sup>a</sup> 1C = 1674 mA g<sup>−1</sup>. <sup>b</sup> Mass percentage of sulfur on the whole cathode excluding the Al or Ni substrate. <sup>c</sup> Capacity degradation rate is estimated from the figure since authors did not provide the specific value in the reference. <sup>d</sup> GO = graphene oxide. <sup>e</sup> CNTs = carbon nanotubes. <sup>f</sup> LiNO<sub>3</sub>-free electrolyte was used for the tested battery. <sup>g</sup> RFC = resorcinol-formaldehyde carbon.



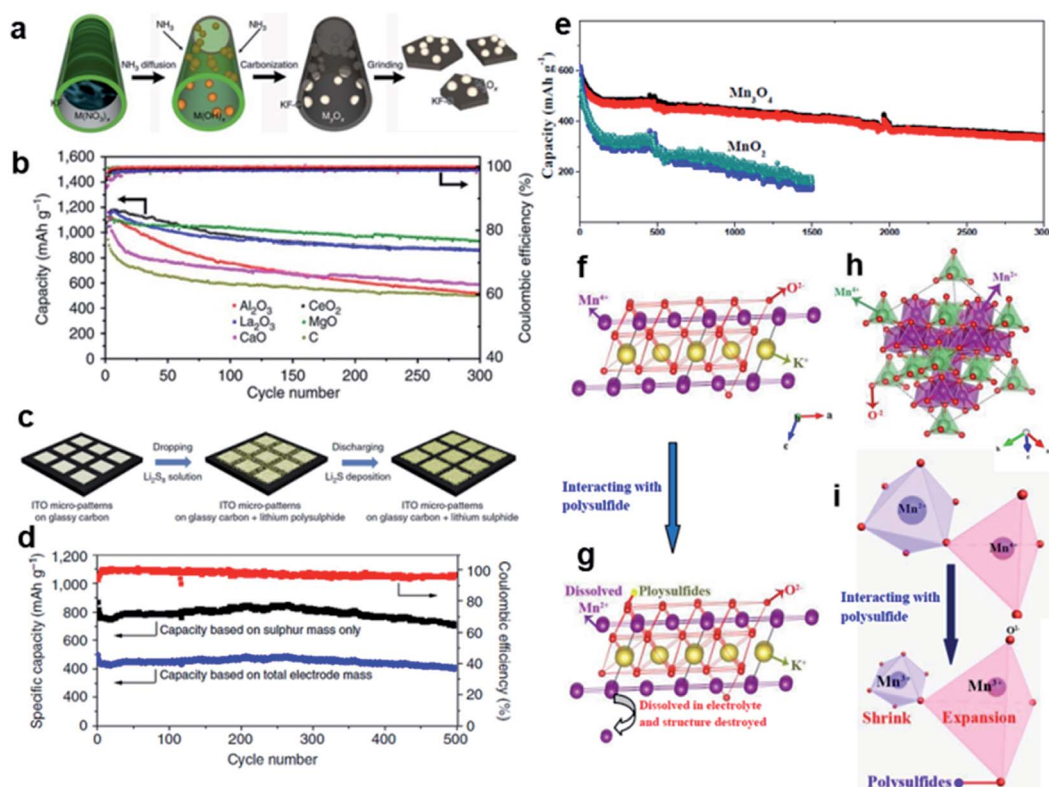


**Fig. 6** (a) A schematic illustration of biotemplated fabrication of oxides/carbon nanostructures using the Kapok tree fibers as both template and carbon sources. (b) Cycling performance of various metal oxides/KF/S composite electrodes at 0.5C.<sup>84</sup> (c) A schematic illustration of the preparation of a LiPS-ITO micropattern glassy carbon cathode showing the LiPS deposition. (d) Cycling performance at 0.5C of an ITO-CNF/Li<sub>2</sub>S<sub>8</sub> catholyte hybrid electrode.<sup>88</sup> (e) Long-term cycling performance of MnO<sub>2</sub>- and Mn<sub>3</sub>O<sub>4</sub>@carbon cloth/sulfur cathodes. (f–i) A scheme showing the structural changes of both MnO<sub>2</sub> and Mn<sub>3</sub>O<sub>4</sub> crystals upon interaction with LiPS.<sup>59</sup> (a and b) Reproduced with permission from ref. 84. Creative Commons Attribution 4.0 International License (<http://creativecommons.org/licenses/by/4.0/>). (c and d) Reproduced with permission from ref. 88. Copyright 2014, Nature Publishing Group. (e–i) Reproduced with permission from ref. 59. Copyright 2017, The Royal Society of Chemistry.

the cathode preparation, a dissolved Li<sub>2</sub>S<sub>8</sub> polysulfide solution commonly termed as the catholyte was used as the starting material instead of conventional solid sulfur or Li<sub>2</sub>S components.<sup>136–138</sup> Preliminary surface analysis using energy dispersive X-ray (EDX) spectroscopy and scanning electron microscopy (SEM) showed that Li<sub>2</sub>S and intermediate LiPSs deposited preferentially on ITO instead of carbon substrates during, respectively, discharge and charge processes, indicating stronger affinity of LiPSs to polar oxygen-rich ITO than to nonpolar carbon. As a consequence of the controlled nucleation and deposition of solid sulfur/Li<sub>2</sub>S species, ITO-CNF/Li<sub>2</sub>S<sub>8</sub> catholyte hybrid electrodes (sulfur content = 40 wt%; sulfur loading = 2.0 mg cm<sup>-2</sup>) revealed an enhanced electrochemical performance with a low capacity decay rate of 0.040% per cycle over 300 cycles at 0.2C. It was also shown that when combining solid sulfur and the Li<sub>2</sub>S<sub>8</sub> catholyte, the hybrid cathode with a high sulfur loading (4.0 mg cm<sup>-2</sup>) can deliver a reversible capacity of 710 mA h g<sup>-1</sup> after 500 cycles (Fig. 6d), representing a low capacity decay rate of 0.036% per cycle. Another representative example was reported by Li *et al.*, who proposed the preparation of a rationally designed hybrid host composite by filling highly conductive hollow CNFs with polar MnO<sub>2</sub> nanosheets (MnO<sub>2</sub>@HCNFs).<sup>102</sup> For such a purpose, SiO<sub>2</sub>-coated

MnO<sub>2</sub> nanowires and resorcinol-formaldehyde resins were used as the hard template and carbon source, respectively. After pyrolysis of the composite and subsequent NaOH-etching of the SiO<sub>2</sub> coating, sulfur was infiltrated into the hollow MnO<sub>2</sub>@HCNF host *via* the melt-diffusion route, while the outer conductive and porous carbon layer aids in driving electron and Li<sup>+</sup> ion transport during charge/discharge cycling. The polar cavity filled with MnO<sub>2</sub> nanosheets serves as a specific polysulfide container capable of mitigating the polysulfide dissolution and also promoting the sulfur-based redox activity. The electrochemical evaluation of the sulfur-infiltrated MnO<sub>2</sub>@HCNF cathode (sulfur content ≈ 50 wt%; sulfur loading = 3.5–3.9 mg cm<sup>-2</sup>) revealed an initial discharge capacity of 1147 mA h g<sup>-1</sup> and stable cycling performance for over 100 cycles at 0.2C. Furthermore, the extended cycling performance of sulfur-MnO<sub>2</sub>@HCF at 0.5C proved a good areal capacity retention of 2.3 mA h cm<sup>-2</sup> after 300 cycles. The integrated structure of MnO<sub>2</sub>-filled HCNFs certainly improves the lifespan of the cells by chemical binding of sulfur-intermediates to the MnO<sub>2</sub> nanosheets.

Nanocrystalline NiFe<sub>2</sub>O<sub>4</sub> is a soft magnetic material with an inverse spinel structure.<sup>139</sup> This kind of ferrite material has been explored as an anode material for LIBs owing to its



electrochemical ability to react with 8 moles of Li, delivering a high theoretical capacity of  $915 \text{ mA h g}^{-1}$ .<sup>140</sup> In 2015, Fan *et al.* used a hybrid CNT/NiFe<sub>2</sub>O<sub>4</sub>/sulfur cathode material for the first time.<sup>58</sup> The one-dimensional CNTs and two-dimensional NiFe<sub>2</sub>O<sub>4</sub> nanosheet components confer, respectively, electron conductivity and LiPS anchor sites to the designed three-dimensional (3D) host material. The latter sulfur nanoparticles (5–20 nm) attached onto the CNT/NiFe<sub>2</sub>O<sub>4</sub> surface serve as the active energy storage component. The resulting 3D hybrid CNT/NiFe<sub>2</sub>O<sub>4</sub>/sulfur composite cathode (sulfur content  $\approx 54 \text{ wt\%}$ ; sulfur loading  $\approx 1.1 \text{ mg cm}^{-2}$ ) delivered a high initial capacity of  $1350 \text{ mA h g}^{-1}$  at 0.1C and a capacity of  $\approx 850 \text{ mA h g}^{-1}$  over 500 cycles at 1C with only 0.009% capacity loss per cycle, one of the best values reported so far.<sup>55,57,59</sup> Although the capacity retention was outstanding, the low sulfur loading in the hybrid cathode needs to be increased to meet the standard for practical applications. It is noted here, that, despite the promising benefits showed by the NiFe<sub>2</sub>O<sub>4</sub> nanosheets, no further studies on NiFe<sub>2</sub>O<sub>4</sub>-containing sulfur cathodes have been reported up to now.

Recently, Li *et al.* suggested an interesting ternary-type MnO<sub>2</sub>/graphene oxide/carbon nanotube (MnO<sub>2</sub>/GO/CNT) scaffold with a three-dimensional architecture and synergistic functions.<sup>104</sup> The proposed sulfur cathode complex consists of (i) innermost one-dimensional CNTs serving as the conductive backbone for the composite, (ii) two-dimensional petal-like MnO<sub>2</sub>/GO nanosheets attached on the sidewalls of the CNT-based backbone having dual-efficient polysulfide-adsorption capability,<sup>61,141</sup> and (iii) outmost nanosized sulfur-active components fixed onto the MnO<sub>2</sub>/GO surface. The hybrid sulfur cathode (sulfur content = 64 wt%; sulfur loading  $\approx 2.8 \text{ mg cm}^{-2}$ ) demonstrated discharge specific capacities of 1500, 1300, 1150 and 1048 mA h g<sup>-1</sup> at, respectively, 0.05, 0.1, 0.2 and 0.5C, a reasonable capacity decay of 0.162% per cycle after 100 cycles, and high coulombic efficiency ( $\approx 99\%$ ). The authors attributed the enhanced performance of the Li-S cells to the features and synergistic effects of the components in the ternary composite, such as the relatively high specific surface area ( $\approx 156 \text{ m}^2 \text{ g}^{-1}$ ) able to tolerate the volume changes caused by discharged products, the conductive CNT-frame for long-range electron transport and the strong chemisorption of the MnO<sub>2</sub> to LiPSs. More recently, Guo *et al.* proposed a Mn<sub>3</sub>O<sub>4</sub> composite with nano-wall arrays as a sulfur-hosting material.<sup>59</sup> The binder-free Mn<sub>3</sub>O<sub>4</sub>@carbon cloth/S cathode (sulfur content  $\approx 62 \text{ wt\%}$ ; sulfur loading =  $2.8 \text{ mg cm}^{-2}$ ) was prepared by the direct growth of Mn<sub>3</sub>O<sub>4</sub> nanoparticles on a carbon cloth *via* an impregnation-hydrothermal decomposition route using KMnO<sub>4</sub> as both Mn and O source and subsequent sulfur melt diffusion at 155 °C. High reversible specific capacities of  $\approx 1000$  and 950 mA h g<sup>-1</sup> are achieved at rates of 0.1 and 0.5C, respectively. Notably, the battery showed a high coulombic efficiency (higher than 98%) and outstanding capacity retention (60%) over 3000 cycles at 2C with a decay as low as  $\approx 0.013\%$  per cycle, one of the longest cycle lives reported so far.<sup>61,142</sup> In contrast, the control cell with a MnO<sub>2</sub>@carbon cloth/S cathode exhibited a capacity retention of 24% after 1500 cycles, under similar cell conditions (Fig. 6e). Such stable cell operation at relatively high sulfur loading was attributed to the good stability of the Mn<sub>3</sub>O<sub>4</sub>

structure upon cycling. As illustrated in Fig. 8 and Fig. 6f, Mn<sup>4+</sup> cations in a MnO<sub>2</sub> crystal are reduced to Mn<sup>2+</sup> upon interaction with LiPS species. The resulting oxide with Mn<sup>2+</sup> cations might be dissolved into the electrolyte during cell cycling (Fig. 6g), weakening the structure of MnO<sub>2</sub> and thus losing the capability to retain the active material. On the other hand, the Mn<sub>3</sub>O<sub>4</sub> structure (Fig. 6h) consists of edge sharing MnO<sub>6</sub> octahedra (Mn<sup>2+</sup>) that are corner linked to MnO<sub>4</sub> tetrahedra (Mn<sup>4+</sup>). Based on SEM and XPS analyses and considering minimal reorganization theory, the authors proposed a simultaneous MnO<sub>4</sub> tetrahedral expansion and a MnO<sub>6</sub> octahedral contraction by the respective reduction of Mn<sup>4+</sup> and oxidation of Mn<sup>2+</sup> to Mn<sup>3+</sup> upon LiPS interaction rather than the formation of Mn<sup>2+</sup> ions (Fig. 6i). Thus, the Mn<sub>3</sub>O<sub>4</sub> structure is less prone to suffer from damage/disintegration.

## 2.4 Metal oxides in functional interlayers and separator coatings

If we consider the number of publications on the topic of Li-S batteries, most of the studies are dedicated to the engineering design of sulfur cathodes using diverse host matrices and the synthesis of novel electrolytes that prevent the diffusion of LiPSs—around 65% and 13% of the Li-S battery-based publications, respectively.<sup>143–145</sup> Although previous studies have made great advances in understanding the chemistry involved in the Li/S couple and thus maximized Li-S cell's performance, the inexorable dissolution of high-order LiPSs in conventional ether-based electrolytes and their further diffusion/migration towards the lithium anode seem to be barely avoidable.

In an effort to tackle the LiPS leakage, Manthiram's group proposed in 2012 the modification of the cell configuration by the insertion of a free-standing carbon interlayer between the separator and the sulfur cathode as a LiPS-trapping conductive membrane.<sup>146,147</sup> The novelty of this “interlayer” concept resides in the multiple functionalities that are present at the conductive and porous membrane. Firstly, the porous interlayer works as a reservoir to intercept and retain the dissolved LiPS in the cathode side. Secondly, due to its high electrical conductivity, it serves as an upper-current collector to reduce the resistance of the cathode by boosting the electron/ion transport. Thirdly, its accessible porous structure offers a physical space to shock-absorb the huge volume changes of the trapped sulfur-based species during cell cycling, preventing interlayer and cathode degradation.<sup>36,148</sup> In other words, the interlayer acts as a secondary sulfur (unfilled) cathode or as an extension of the primary sulfur cathode whose functions are triggered during cell operation by the early capture and storage of the migrating sulfur species and further reutilization of the sequestered active material. Inspired by this pioneering work, two years later the same group used a similar *in situ* LiPS-trapping concept by integrating a carbon interlayer in a commercial polypropylene separator.<sup>149–151</sup> The designed functional carbon-coated separators not only incorporate the features shown by free-standing carbon interlayers but also the manufacturing coating process allows to decrease the thickness and, thus, the weight of the carbon layer, resulting in a cell with higher specific energy





density. In comparison with the conventional Li-S cell configuration, the innovative Li-S cells containing an interlayer or a separator coating produced from conductive carbon nanostructures (*i.e.*, CNTs, graphene oxide, rGO, *etc.*),<sup>152–156</sup> porous (doped) carbons<sup>157–162</sup> or conducting polymers<sup>163–167</sup> have considerably improved sulfur utilization, capacity retention and cycle life. However, since bare carbon materials only provide for weak interaction with polar LiPS species, in the past few years, there has been increased interest to incorporate diverse metal oxide nanomaterials as one of the components of the functional separator coatings/interlayers in order to improve the LiPS affinity/utilization *via* chemisorption and/or electrocatalytic effects. The explored metal oxides include TiO<sub>2</sub>,<sup>168–174</sup> SnO<sub>2</sub>,<sup>175,176</sup> MnO<sub>2</sub>,<sup>142,177</sup> MnO,<sup>178</sup> BaTiO<sub>3</sub>,<sup>179</sup> RuO<sub>2</sub>,<sup>180</sup> CeO<sub>2</sub>,<sup>181</sup> Mg<sub>0.6</sub>Ni<sub>0.4</sub>O,<sup>182</sup> Li<sub>4</sub>Ti<sub>5</sub>O<sub>12</sub>,<sup>183</sup> LiAlO<sub>2</sub>,<sup>184</sup> V<sub>2</sub>O<sub>5</sub>,<sup>185,186</sup> SiO<sub>2</sub>,<sup>187</sup> La<sub>2</sub>O<sub>3</sub>,<sup>188</sup> Y<sub>2</sub>O<sub>3</sub>,<sup>189</sup> and NiO.<sup>190</sup> A summary of representative metal oxide-containing functional interlayers/hybrid separators developed recently is shown in Table 2. The values of this table should be taken with care as the capacity and reversibility strongly depend on the applied cell parameters such as the amount and type of electrolyte, electrode thickness, sulfur mass loading, sulfur composition, binder and separator. In order to provide a comparable picture we added some important parameters such as the mass loading of the interlayer/coating, sulfur ratio within the whole cathode (excluding the Al or Ni substrate), sulfur mass loading and C-rates.

V<sub>2</sub>O<sub>5</sub> was one of the first polar metal oxides to be introduced into an interlayer for Li-S cells. Li *et al.* deposited electronically conductive V<sub>2</sub>O<sub>5</sub> onto one side of commercial polypropylene battery separators (Celgard 3401 and 3501).<sup>185</sup> The V<sub>2</sub>O<sub>5</sub> interlayer acts as both a solid-state Li<sup>+</sup> ion conductor and a polysulfide anion barrier. By blocking the LiPS diffusion to the Li anode, the cell composed of a nanoporous carbon foam-sulfur composite cathode (sulfur content  $\approx$  60 wt%; sulfur loading = 3.0 mg cm<sup>-2</sup>) attested a stable cyclability for over  $\approx$  1 year with an average capacity of 800 mA h g<sup>-1</sup> representing an estimated degradation rate of 0.040% per cycle. Instead of a free-standing interlayer or a separator coating, Xiao *et al.* directly coated the surface of a porous CNTs/sulfur cathode with a porous graphene/TiO<sub>2</sub> layer.<sup>168</sup> The added interlayer corresponds to 7.8 wt% of the whole cathode. While the porous graphene provides an electrically conductive network able to physically trap soluble and escaping sulfur species, the TiO<sub>2</sub> in the interlayer further promotes the chemical anchorage of LiPSs *via* S-Ti-O interactions.<sup>50,63</sup> Using this advanced cathode with a coupled graphene/TiO<sub>2</sub> interlayer (sulfur content = 51.2 wt%; sulfur loading = 0.51 mg cm<sup>-2</sup>), cells cycled over 1000 times exhibited ultralow capacity decay rates of 0.010 and 0.018% per cycle, at C-rates of 2 and 3C, respectively.<sup>55,57–59</sup> Similar to Li *et al.*,<sup>104</sup> Wang and co-workers also employed a ternary MnO<sub>2</sub>/GO/CNT nanostructured architecture. In this case the designed ternary system was layered onto a polypropylene separator (Celgard 2400), acting as a LiPS-trapping shield (Fig. 7a).<sup>142</sup> The ultrathin functional interlayer denoted as G/M@CNT (thickness of 2  $\mu$ m and areal density of 0.104 mg cm<sup>-2</sup>) facilitates electron transport through the high conductivity CNTs and enables the chemisorption of migrating LiPS intermediates by strong

interactions between LiPSs with polar oxygen groups in the GO sheets and MnO<sub>2</sub> nanoparticles. The improved Li-S cell with a functional interlayer@pristine separator (Table 2) demonstrated a notable cycling performance over 2500 cycles with a low capacity degradation of 0.029% per cycle at 1C, while the cell with a pristine separator only reached  $\approx$  700 cycles before cell failure (Fig. 7b).

Among typically used metal oxides (*e.g.* V<sub>2</sub>O<sub>5</sub>, TiO<sub>2</sub>, and MnO<sub>2</sub>), in the last few years, new metal oxides have been proposed to confine and re-use the sulfur active material. For instance, electrically conductive and catalytically active RuO<sub>2</sub> nanoparticles ( $\approx$  2 nm) were used to improve the LiPS redox reaction kinetics and hence the sulfur (re)utilization.<sup>180</sup> As a proof of concept, a multifunctional RuO<sub>2</sub> nanoparticle-decorated mesoporous carbon-coated hybrid separator (denoted as RuO<sub>2</sub>-MPC-HS) was used to boost the electrochemical performance of Li-S batteries (Fig. 7c). The hybrid separator not only provides an electron transport network but also serves as an effective LiPS-net to early trap and retain the active material in the positive electrode. As a consequence of the electrocatalytic effect resulting from the RuO<sub>2</sub> nanoparticles, a simple-mixed sulfur/carbon black cathode (sulfur content  $\approx$  63 wt%; sulfur loading  $\approx$  2.0 mg cm<sup>-2</sup>) delivered a high initial capacity of 1276 mA h g<sup>-1</sup> at 0.1C and remarkable cycling stability with a low degradation rate of 0.022% per cycle over 200 cycles at 0.5C (Fig. 7c). Dipole-aligned BaTiO<sub>3</sub> particles, already used as an additive in Li-S cells,<sup>48</sup> were utilized by Yim *et al.* to coat one side of a commercial poly(ethylene) separator with the aim to reject polar LiPS species during migration to the lithium anode (Fig. 7d).<sup>179</sup> Li-S cells with a LiNO<sub>3</sub>-free electrolyte comprising a poled BaTiO<sub>3</sub>-coated separator, previously activated in an electric field, demonstrated a notable reduction of the overcharging behavior typically observed during charge processes, providing an initial coulombic efficiency of 79.6%, while cells with an non-poled BaTiO<sub>3</sub>-coated separator and a pristine separator exhibited coulombic efficiencies of 42.3 and 26.3%, respectively. Such behavior was also visualized by a LiPS rejection test (Fig. 7e). The enhanced coulombic efficiency in the absence of the LiNO<sub>3</sub> additive is explained by the poling effect of the BaTiO<sub>3</sub>-coating which effectively repels negatively charged LiPSs by electrostatic repulsion. A cycling performance investigation carried out at 0.5C exposed an initial capacity of 1122 mA h g<sup>-1</sup> for the cell with a poled BaTiO<sub>3</sub>-coated separator (cathode sulfur content = 41 wt%; sulfur loading = 3.9 mg cm<sup>-2</sup>). It is noted that the test was limited to only 50 cycles revealing an ending capacity of 929 mA h g<sup>-1</sup>. Additionally, the BaTiO<sub>3</sub>-coating also avoids thermal shrinkage of the polymeric separator at high temperatures, improving cell's safety. A Li-S cell with a flexible, freestanding ternary hollow NiO/rGO-Sn interlayer sandwiched between the separator and sulfur cathode was recently proposed by Li *et al.*<sup>190</sup> In this multifunctional interlayer each component synergistically serves a specific purpose: (i) the rGO constructs a 3D highly conductive network, (ii) the hollow NiO tightly wrapped by rGO nanosheets provides a physical place to store soluble LiPSs and buffers volume changes and (iii) the Sn, in tandem with NiO, chemically interacts with LiPS intermediates to immobilize them in the





**Table 2** Summary of representative metal oxide-containing functional interlayers/hybrid separators used for Li–S batteries

Metal oxides in interlayers	Reversible				Degradation rate per cycle [%]	Interlayer mass [mg cm <sup>-2</sup> ]	Sulfur content <sup>b</sup> [wt%]	Sulfur loading [mg cm <sup>-2</sup> ]	Ref.
	Initial capacity [mA h g <sup>-1</sup> ]	Reversible capacity [mA h g <sup>-1</sup> ]	Current rate <sup>a</sup>	Cycle number					
CNT@TiO <sub>2</sub>	1258	541	0.5C	1000	0.055	0.7	37	1.7	173
CNT@TiO <sub>2</sub>	969	783	0.2C	100	0.192	0.7	39	3.0	173
TiO <sub>2</sub> -CNFs	1238	770	0.2C	300	0.126	1.6	45	3.0	174
SnO <sub>2</sub> @hollow carbon spheres	996	832	0.5C	100	0.165	0.2	≈ 48	≈ 2.0	175
V <sub>2</sub> O <sub>5</sub> -CNFs	816	576	3C	1000	0.029	1.0	≈ 52	≈ 2.0	186
NiO/rGO	1500	700	0.1 A g <sup>-1</sup>	150	0.355	1.06	≈ 51	4.0	190
NiO/rGO-Sn	1690	868	0.1 A g <sup>-1</sup>	150	0.324	1.4	≈ 47	4.0	190

Metal oxides in separator coatings	Reversible				Degradation rate per cycle [%]	Interlayer mass [mg cm <sup>-2</sup> ]	Sulfur content <sup>b</sup> [wt%]	Sulfur loading [mg cm <sup>-2</sup> ]	Ref.
	Initial capacity [mA h g <sup>-1</sup> ]	Reversible capacity [mA h g <sup>-1</sup> ]	Current rate <sup>a</sup>	Cycle number					
TiO <sub>2</sub> /carbonized bacterial cellulose	1000 <sup>c</sup>	752	0.5C	100	0.248 <sup>c</sup>	N/A	70*	2.5	171
MnO <sub>2</sub> /GO/CNTs	1025	293	1C	2500	0.029	0.1	60–80	1.1–2.4	142
Hollow CNF@MnO <sub>2</sub>	800 <sup>c</sup>	593	1C	400	0.065	N/A	70*	2.1	177
MnO-Ketjen black carbon	1059	901	1C	200	0.075	0.125	≈ 57	1.5–2.0	178
BaTiO <sub>3</sub>	1122	929	0.5C	50	0.344	2.4	41	3.0	179
RuO <sub>2</sub> -mesoporous carbon	695	665	0.5C	200	0.022	0.3	≈ 63	≈ 2.0	180
CeO <sub>2</sub> -Ketjen black carbon	1004	625	1C	500	0.075	0.3	≈ 49	≈ 1.9	181
V <sub>2</sub> O <sub>5</sub> <sup>d</sup>	890 <sup>c</sup>	800 <sup>c</sup>	C/15	250	0.040	N/A	60*	3.0	185
SiO <sub>2</sub> nanoparticles	937	603	0.2C	200	0.178	0.124	48	≈ 1.3	187
La <sub>2</sub> O <sub>3</sub> -Ketjen black carbon	966	720	1C	200	0.127	0.4	42	1.5	188
Y <sub>2</sub> O <sub>3</sub> -Ketjen black carbon	1054	816	1C	200	0.113	N/A	60*	1.3	189

<sup>a</sup> 1C = 1674 mA g<sup>-1</sup>. <sup>b</sup> Mass percentage of sulfur on the whole cathode including the interlayer weight. Those values with asterisk represent the sulfur content without the interlayer weight since the authors did not provide such information in the paper. <sup>c</sup> Capacity/degradation rate was estimated from the figure since the authors did not provide the specific number in the paper. <sup>d</sup> The battery was tested in a pouch cell configuration.

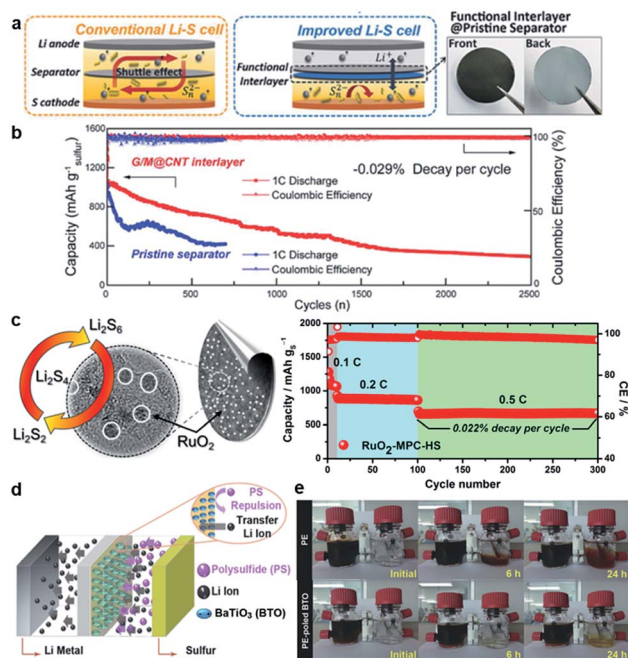


Fig. 7 (a) Schematic configuration of the Li-S cells with a pristine separator (left) and a G/M@CNT-coated separator (middle). Photographs of the G/M@CNT-coated separator (right). (b) Long-term cycling performance of cells with pristine and G/M@CNT-coated separators.<sup>142</sup> (c) A schematic illustration of the RuO<sub>2</sub>-MPC-HS structure (left) and the combined cycling performance of the Li-S cell with RuO<sub>2</sub>-MPC-HS (right).<sup>180</sup> (d) A schematic diagram of the poled BaTiO<sub>3</sub> (BTO) effect toward LiPS rejection. (e) LiPS diffusion test. PE-poled BTO separator showed a better rejection of Li<sub>2</sub>S<sub>8</sub> solution (left bottle) compared with the PE separator.<sup>179</sup> (a and b) Reproduced with permission from ref. 142. Copyright 2017, Wiley-VCH. (c) Reproduced with permission from ref. 180. Copyright 2016, The Royal Society of Chemistry. (d and e) Reproduced with permission from ref. 189. Copyright 2016, Wiley-VCH.

interlayer, as concluded according to XPS analyses. The cell with the ternary interlayer showed a slight improvement in capacity compared with the control cell containing a NiO/rGO interlayer (Table 2). Note, however, that the added Sn increases the mass of the ternary interlayer by roughly 32%, which is detrimental to the whole sulfur content and hence cell's energy density.<sup>158,191</sup>

Undoubtedly, the reconfiguration of the Li-S battery by either integrating a functional interlayer or using a hybrid functional separator is a promising approach to hinder the migration of soluble LiPS intermediates, to indirectly protect the lithium anode from side reactions, to reactivate dead sulfur-based species, to decrease internal cell resistance and thus to enhance the overall electrochemical performance of the Li-S batteries. Nonetheless, special attention should be paid to the added weight of the interlayer/separator coating since this parameter could be counter-productive in terms of energy density.

In summary, the use of metal oxides improves the Li-S cell performance by constraining the LiPS shuttle phenomenon. Further screening of novel nanostructured metal oxides for advanced sulfur composite cathodes and, most importantly, the fundamental understanding of how LiPS species chemically

interact with these oxide materials are critical to make a significant leap forward to high-performance Li-S batteries.

### 3. Metal sulfides

(Transition) metal sulfides (TMSs) are the most reported metal chalcogenides as co-components in Li-S batteries. Many of them are widely available and exhibit unique properties such as semi-metallic to metallic characteristics, magnetic moments and polar bonds within the molecular structure. Their adsorption capabilities for many gases are well known in heterogeneous catalysis, in particular for hydrodesulfurization.<sup>192</sup> TMSs are also used in many other applications such as magnetism, fuel cells, electrochemical water splitting and battery electrode materials. Metal (di)sulfides (Fe, Co, Ni, Mo, Cr, W, Cu, and Mn)<sup>193,194</sup> have been studied as both intercalation and conversion electrodes for positive and negative electrodes in secondary lithium batteries.<sup>195</sup> There are some excellent reviews focusing on metal chalcogenides as electrode materials themselves.<sup>196,197</sup> Herein, we will review the beneficial interaction of LiPSs with metal sulfides as co-components to improve the electrochemical performance of Li-S batteries.

At the beginning of this decade, metal sulfides found their way as additive, coating or host materials for sulfur composite cathodes and for functional separators to improve the active material utilization and cycle life of Li-S batteries. They are supposed to enhance electronic and ionic conductivity within the electrode, improve charge transfer processes and most importantly exhibit the capability to capture sulfur species and thus prevent shuttling between the cathode and anode. It is believed that the adsorption of LiPSs and their redox-reaction on the conductive electrode surface can govern the overall reaction kinetics, in particular when the LiPS concentration is very high like in high-energy batteries and thus diffusion processes are very fast.<sup>198</sup>

If the electrode surface is non-polar as it is for conventional carbon, the adsorption of polar LiPS intermediates is energetically unfavorable and slow. In this regard, the addition of polar/ionic compounds by doping carbon (*i.e.* with nitrogen) was proven to enhance the electrochemical performance. The adsorption on a metal sulfide is thereby best described by Lewis base-acid interactions where the LiPSs provide a free electron pair binding to the metal cation (Lewis acid). After successful LiPS adsorption, charge transfer reactions and the reversal oxidation of Li<sub>2</sub>S to Li<sub>2</sub>S<sub>n</sub> may be the rate determining step. The decomposition of Li<sub>2</sub>S during charging was proven to be successfully catalyzed by several metal sulfides<sup>199</sup> and the potential for catalysis may be somehow related to the electronic conductivity of the metal sulfide. A demonstrative scheme for the catalytic sulfur reduction with CoS<sub>2</sub> as the catalyst is shown in Fig. 8a and b in which the rate controlling step is highlighted as the charge transfer to the adsorbed LiPSs.<sup>198</sup> Zhou *et al.* proposed a similar scheme in which the catalytic decomposition and oxidation of Li<sub>2</sub>S was found to be an important step to reach high efficiency and reversibility (Fig. 8c and d).<sup>199</sup>

It was shown for TiO<sub>x</sub> that the electronic conductivity of the co-component can improve the cycle life and the efficiency of





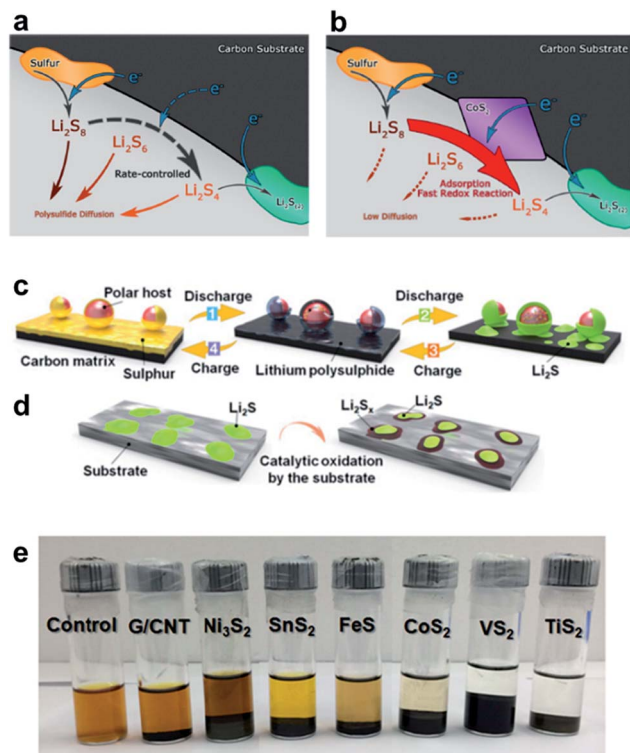


Fig. 8 Scheme for the redox-reaction of sulfur to  $\text{Li}_2\text{S}_n$  on the electrode surface (a) without and (b) with the  $\text{CoS}_2$  catalyst.<sup>198</sup> A general scheme for the decomposition and oxidation of  $\text{Li}_2\text{S}$  to form soluble  $\text{Li}_2\text{S}_n$  (c) without and (d) with the catalyst, and (e) a visual adsorption capability of different metal sulfides to capture LiPSs.<sup>199</sup> (a and b) Reproduced with permission from ref. 198. Copyright 2016, American Chemical Society. (c and d) Reproduced with permission from ref. 199. Copyright 2016, National Academy of Sciences.

the sulfur cathode.<sup>55</sup> It is thus important to consider the physical properties of chalcogenides and to study both effects: (i) capability to adsorb LiPSs and (ii) electronic conductivity to accelerate charge transport processes. Further improvement of ionic conductivity may play a critical role. Very often the capability to capture LiPSs is evaluated visibly or with spectroscopy based on the adsorption of a brownish LiPS solution with and without the sulfide (Fig. 8e). However, a standardized procedure to measure the adsorption capability of LiPSs (*i.e.* in mg  $\text{Li}_2\text{S}_n$  per mg host material), as conducted by Pang *et al.*, is still not well established but could simplify the identification of promising metal sulfide additives for sulfur cathodes.<sup>200</sup> Table 3 provides an overview of the electronic conductivity and the affinity of some chalcogenides to  $\text{Li}_2\text{S}_4/\text{Li}_2\text{S}$  determined through first principles DFT calculations from various reports. Considering all reports, the highest binding energy to  $\text{Li}_2\text{S}$  is found for  $\text{TiS}_2$  and  $\text{VS}_2$ . As a comparison, graphitic carbon which is frequently used to encapsulate or make an electrical contact with sulfur exhibits only low capability to capture short and long chained LiPSs. These findings conform to a recent study from Chen *et al.* who found the strongest anchoring effect for  $\text{VS}_2$  followed by  $\text{TiS}_2$  based on theoretical calculations.<sup>201</sup> In a comparative study, Zhou *et al.* experimentally confirmed the best performance with  $\text{VS}_2$  followed by  $\text{TiS}_2$  and  $\text{CoS}_2$ .<sup>199</sup> Although  $\text{VS}_2$  seems to offer superior properties as an additive in sulfur cathodes, most reports deal with  $\text{TiS}_2$  and  $\text{CoS}_2$ . Interestingly,  $\text{MoS}_2$  also shows strong affinity to  $\text{Li}_2\text{S}$  at the edge of the crystal facet and exceeds the values of all other metal sulfides, whereas the terrace side of  $\text{MoS}_2$  exhibits only low capability. This dependency of the exposed side of the crystal facet to the LiPS adsorption was experimentally and theoretically studied by Wang *et al.* using differently shaped  $\text{MoS}_2$  crystals to boost LiPS redox-reactions.<sup>202</sup> In addition, Zhou *et al.*

Table 3 The electrical conductivity of some metal sulfides, their affinity to LiPSs based on first principles DFT calculations and their electrochemical behavior *versus* lithium metal

Material	Electrical conductivity, $\sigma$ [ $\text{S cm}^{-1}$ ]	Binding energy to $\text{Li}_2\text{S}_4/\text{Li}_2\text{S}$ determined by DFT calculations [eV]	Mechanism of lithium storage in the range, 1.5–2.6 V vs. $\text{Li}/\text{Li}^+$	Ref.
Graphite	1–1000	0.34 ( $\text{Li}_2\text{S}_4$ ) 0.29 ( $\text{Li}_2\text{S}$ )	No reaction	198, 209 and 210
$\text{WS}_2$	6.7	0.8 ( $\text{Li}_2\text{S}_4$ ) 1.45 ( $\text{Li}_2\text{S}$ )	No reaction	211, 193 and 207
$\text{NiS}_2$ (111)	2–55	2.06 ( $\text{Li}_2\text{S}_4$ )	Intercalation/conversion < 1.8 V	212
$\text{TiS}_2$	30–50	2.99 ( $\text{Li}_2\text{S}$ )	Intercalation < 2.5 V	213 and 214
$\text{ZrS}_2$	1.32	2.7 ( $\text{Li}_2\text{S}$ )	Intercalation/conversion	214 and 215
$\text{VS}_2$	0.1	2.94 ( $\text{Li}_2\text{S}$ )	Intercalation	214 and 216
$\text{FeS}_2$	0.6	N/A	N/A	217
$\text{SnS}_2$ (001)	$1.8 \times 10^{-4}$ (semiconductor)	1.26 ( $\text{Li}_2\text{S}_4$ )	Intercalation	218 and 219
$\text{Bi}_2\text{S}_3$ (001)	$1.8 \times 10^{-7}$	2.52 ( $\text{Li}_2\text{S}_4$ )	Conversion < 1.73 V	220 and 221
$\text{MoS}_2$	1000	0.87 terrace site 4.48 Mo-edge ( $\text{Li}_2\text{S}$ )	No reaction	220 202
$\text{CoS}_2$ (111)	6–5000	1.97 ( $\text{Li}_2\text{S}_4$ )	No reaction	217, 222, 198 and 208
$\text{Co}_9\text{S}_8$	290	2.74 ( $\text{Li}_2\text{S}$ ) (002) 1.71 ( $\text{Li}_2\text{S}_4$ ) (002)	No reaction	222 200
$\text{CuS}$	870	N/A	N/A	223
$\text{Cu}_2\text{S}$	6700	N/A	N/A	217
$\text{ZnS}_2$	$1 \times 10^{-6}$	N/A	N/A	217



proposed that the Li atom within the  $\text{Li}_2\text{S}_4$  molecule binds to the negatively polarized sulfide within the  $\text{CoS}_2$  structure while the LiPSs are nucleophilic and bind to the Co atom.<sup>203</sup> These findings prove that the exposed interfacial facet of the nano-crystal is highly important and may open pathways to tailor the adsorption capabilities of LiPSs not only by the type of metal sulfide but also by engineering the crystal shape.

In order to understand the interaction of sulfur species with TMSs, it is also of high importance to consider the structural changes of the metal sulfide during lithium insertion within the potential range of sulfur (1.7–2.6 V vs.  $\text{Li}/\text{Li}^+$ ) as they significantly affect the physical properties. Some metal sulfides (*i.e.*  $\text{VS}_2$  and  $\text{TiS}_2$ ) intercalate lithium ions up to a certain potential, some undergo a conversion reaction (*i.e.*  $\text{FeS}_2$ ,  $\text{NiS}_2$ , and  $\text{MoS}_2$ )<sup>204–206</sup> often to  $\text{Li}_2\text{S}$  and metal cations and some merely show a reaction as in the case of  $\text{WS}_2$  and  $\text{CoS}_2$ .<sup>207,208</sup> The different types of lithium insertion are presented in Table 3.

Metal sulfides were found to be efficient compounds to enhance the adsorption of LiPSs and enhance and afford faster redox reactions. A brief overview of the achievements in improving Li–S batteries with different TMSs is shown in Table 4. Again, the values reported in this table should be taken with care as the capacity and reversibility strongly depend on the applied cell parameters such as the amount and type of electrolyte, electrode thickness, sulfur mass loading, sulfur composition, binder and separator. In order to provide a comparable picture we added some important parameters such as the sulfur ratio within the electrode, mass loading and C-rates. As concluded from Table 4, most reports deal with cobalt sulfides and titanium sulfides likely because of their wide availability, high electronic conductivity and high affinity to LiPS species. The properties of these metal sulfides were proven

to lower the overpotential for  $\text{Li}_2\text{S}$  oxidation and to enhance energy efficiency compared to other metal sulfides such as  $\text{FeS}$ ,  $\text{SnS}_2$  and  $\text{Ni}_2\text{S}_3$ .<sup>199</sup> Both, cobalt and titanium sulfides as co-components will be reviewed first.

### 3.1 Cobalt sulfide

There are several known Co–S phases with different crystal structures (*i.e.*  $\text{CoS}$ ,  $\text{CoS}_2$ ,  $\text{Co}_3\text{S}_4$  and  $\text{Co}_9\text{S}_8$ ). Their unique physical properties such as high electrical conductivity (up to  $5000 \text{ S cm}^{-1}$  at room temperature)<sup>222</sup> and magnetic moment lead to applications in (electro)-catalysis,<sup>224–226</sup> as an anode material for lithium ion batteries, in magnetic applications and secondary alkaline batteries.<sup>208</sup>

The application of various cobalt sulfides as co-components in sulfur cathodes recently gained increasing attention. Until now,  $\text{CoS}_2$ ,  $\text{Co}_3\text{S}_4$  and  $\text{Co}_9\text{S}_8$  supported sulfur cathodes have been reported.<sup>198,200,203,227–233</sup> Yuan *et al.* prepared  $\text{CoS}_2$  (cattierite type) particles (20–200 nm) through a hydrothermal method deposited in graphene layers as a sulfophilic host material for sulfur cathodes with  $\text{CoS}_2$  compositions ranging from 0–30 wt%.<sup>198</sup> It was shown that an increasing amount of  $\text{CoS}_2$  accelerates the electrochemical reaction, decreases liquid–solid polarization and positively affects the LiPS redox kinetics. Furthermore, the adsorption capability of LiPSs was visually proven. The best performance was achieved with 15 wt%  $\text{CoS}_2$  at an initial discharge capacity of  $1368 \text{ mA h g}^{-1}$  and  $1005 \text{ mA h g}^{-1}$  after 150 cycles (75 wt% sulfur loading at 0.5C) while the discharge capacity without  $\text{CoS}_2$  was only  $843 \text{ mA h g}^{-1}$  and  $513 \text{ mA h g}^{-1}$  after 150 cycles. DFT calculations with  $\text{Li}_2\text{S}_4$  molecules confirmed the strong interfacial interaction of  $\text{CoS}_2$  and LiPSs rather than chemical adsorption (Table 4). The calculations also

Table 4 Summary of some selected reports using a TMS as a co-component in Li–S batteries<sup>a</sup>

Material	Initial capacity [ $\text{mA h g}^{-1}$ ]	Degradation rate per cycle [%]	Sulfur content <sup>b</sup> [wt%]	Sulfur loading [ $\text{mg cm}^{-2}$ ]	Ref.
$\text{CoS}_2$ interlayer	1240 at 0.2C	0.17 at 0.2C	64	1.55	227
$\text{Co}_9\text{S}_8$ host	1130 at 0.05C	0.045 at 0.5C	75	1.5	200
$\text{Co}_3\text{S}_4$ host	1012 at 0.2C	0.079 at 1C	53	4.7	228
$\text{CoS}_2$ additive	1368 at 0.5C	0.034 at 2C	75	0.5	198
$\text{CoS}_2$ additive	1326 at 0.1C	0.047 at 1C	56	2.3	203
$\text{Co}_9\text{S}_8$ -Celgard	1385 at 0.1C	0.039 at 1C	70	2.0	233
$\text{TiS}_2$ additive	1000 per g (S + $\text{TiS}_2$ ) at 0.1C	0.1 at 0.1C	48	N/A	235
$\text{TiS}_2$ additive	1000 per g (S + $\text{TiS}_2$ ) at 0.1C	1.3 at 0.1C	45	N/A	238
$\text{TiS}_2$ encapsulation	1156 at 0.2C	0.058 at 0.5C	35	2	214
$\text{MoS}_2$ additive	1270 at 0.2C	0.07 at 0.2C	38	3.9	246
$\text{MoS}_2$ additive	1339 at 0.2C	0.08 at 0.5C	N/A	2	202
$\text{MoS}_2$ coating	950 at 0.2C	0.083 at 0.5C	65	N/A	247
$\text{SnS}_2$ additive	1237 at 0.2C	0.127 at 0.2C	51	N/A	249
$\text{SnS}_2$ additive	1400 at 0.1C	0.058 at 0.5C	62	2.4	219
$\text{Bi}_2\text{S}_3$ additive	1480 at 0.1C	0.028 at 0.5C	46	2.2–3.3	221
$\alpha$ - $\text{NiS}_2$ host	1540 at 0.067C	0.019 at 0.33C	50	2	251
$\text{NiS}_2$	1203 at 0.1C	0.04 at 2C	39	2.0–3.3	212
$\text{WS}_2$ host	1581 at 0.1C	0.0072 at 2C	55	2	57
$\text{WS}_2$ interlayer	1454 at 0.02C	0.055 at 0.5C	70	4	254

<sup>a</sup> 1C =  $1674 \text{ mA g}^{-1}$ . For clarification: interlayer is placed between the cathode and separator, coating was placed onto the separator, host corresponds to the carrier material for sulfur and additive means simple addition to the sulfur cathode composite. <sup>b</sup> Mass percentage of sulfur on the cathode excluding current collector substrate.



indicated enhanced charge transfer processes on the molecular level when  $\text{Li}_2\text{S}_4$  was adsorbed to the (111)  $\text{CoS}_2$  plane. Pang *et al.* report about a graphene-like metallic  $\text{Co}_9\text{S}_8$  nano-sheet structure as a host material for a high sulfur content.<sup>200</sup>  $\text{Co}_9\text{S}_8$  with a surface area of  $108 \text{ m}^2 \text{ g}^{-1}$  was prepared through microwave solvothermal methods. Capacities up to  $1130 \text{ mA h g}^{-1}$  at C/20 were achieved and the rate capability was very high with almost no capacity drop from 0.5 to 2C even though the sulfur content was as high as 75 wt% in the cathode highlighting the positive effect of  $\text{Co}_9\text{S}_8$ . After 400 cycles at 2C, about 75% of the capacity is retained (Fig. 9a). The intrinsic adsorptivity of  $\text{Co}_9\text{S}_8$  (normalized to the surface area) for LiPSs is almost five times higher than that observed for materials such as  $\text{Ti}_4\text{O}_7$  or meso- $\text{TiO}_2$  frequently reported as LiPS capturing materials (Fig. 8d). In fact, DFT calculations showed that at the (008) facets, only positively charged Co atoms are exposed. The binding energy of  $\text{Li}_2\text{S}_2$  can reach to 6.06 eV, one of the highest values reported so far. Furthermore, a high mass loading of  $4.5 \text{ mg cm}^{-2}$  at a C-rate of 0.5 with a reversible areal capacity of  $2.5 \text{ mA h cm}^{-2}$  was demonstrated. These results highlight the large potential of  $\text{Co}_9\text{S}_8$  and cobalt sulfides in general as additives for sulfur-cathodes. Zhou *et al.* synthesized N-doped carbon hosts with and without embedded Co or  $\text{CoS}_2$  nanoparticles by carbonization of a metal-organic framework (ZIF-67).<sup>203</sup> A capacity of  $1326 \text{ mA h g}^{-1}$  at 0.1C (56 wt% sulfur) and the best reversibility was achieved with  $\text{CoS}_2$  nanoparticles (Fig. 9b). After 250 cycles the electrode with  $\text{CoS}_2$  shows a capacity of  $702 \text{ mA h g}^{-1}$  while the electrode with Co/N-doped carbon exhibits  $589 \text{ mA h g}^{-1}$  and the bare carbon host only  $446 \text{ mA h g}^{-1}$ . The enhanced performance of the sulfur cathode is attributed to the synergistic effect of  $\text{CoS}_2$  and N-doping within a porous carbon material to accelerate sulfur redox coupling which was clearly evidenced by the visual adsorption of LiPSs. Even after a short exposure of 1 h of the  $\text{CoS}_2$ -carbon composite to a LiPS solution, the entire LiPS solution turned colorless whereas the Co-

carbon or carbon host needed about 72 h to anchor the LiPS species (Fig. 9c). Instead of the preparation of  $\text{CoS}_2$  composite cathodes, Ma *et al.* inserted interlayers between the cathode and separator, made of hydrophilic porous carbons and  $\text{CoS}_2$ , in order to prevent the diffusion of LiPS intermediates to the anode and, thus, to reduce the shuttle effect.<sup>227</sup> The cycle stability could be significantly improved due to lower charge transfer resistance and the adsorption capability of the modified  $\text{CoS}_2$  interlayer.

Xu *et al.* prepared hollow  $\text{Co}_3\text{S}_4$  polyhedra with a porous shell as a host material for sulfur within free-standing activated carbon nanofibers (ACNFs) (Fig. 9d).<sup>228</sup> By comparing ACNFs with and without  $\text{Co}_3\text{S}_4$  polyhedra as a sulfur host, enhanced rate capability, reversibility and smaller polarization were confirmed. A high areal capacity of  $13 \text{ mA h cm}^{-2}$  at  $13.5 \text{ mg cm}^{-2}$  sulfur mass and a current rate of 0.3C was achieved (Fig. 9e and f).

According to Song *et al.*, an areal capacity higher than  $4 \text{ mA h cm}^{-2}$  is required for Li-S batteries to outperform commercial Li-ion batteries.<sup>234</sup> Furthermore, a capacity of  $953 \text{ mA h g}^{-1}$  at 1C and  $610 \text{ mA h g}^{-1}$  after 450 cycles with a relatively high loading of  $2.5 \text{ mg cm}^{-2}$  were demonstrated. Here again, the outperforming electrochemical performance was mainly attributed to the physical properties of  $\text{Co}_3\text{S}_4$ .

### 3.2 Titanium sulfide

Among the several titanium compounds to capture LiPSs, the most frequently reported compounds are titanium oxides which undergo strong Ti-S interactions. As discussed above, this material was already successfully employed as a performance enhancing additive in many Li-S batteries.<sup>50,51,53</sup> In recent years,  $\text{TiS}_2$  also turned out to be a promising additive for Li-S batteries.<sup>235</sup>  $\text{TiS}_2$  is already known since the 1970s as a layered intercalation cathode material for rechargeable lithium

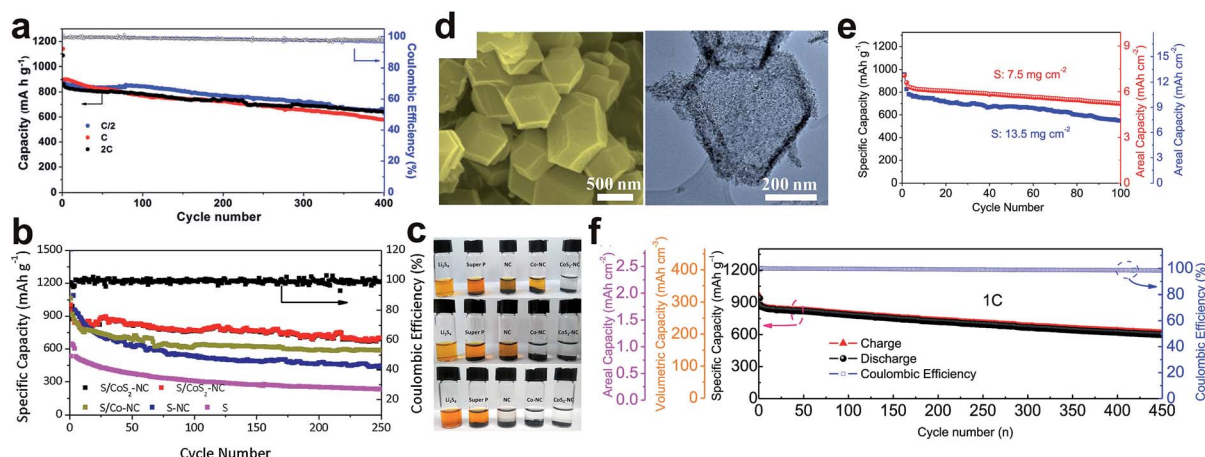


Fig. 9 Some chosen studies dealing with cobalt sulfides in sulfur cathodes: (a) Galvanostatic cycling of a  $\text{Co}_9\text{S}_8/\text{S}$  (75 wt% S) composite.<sup>200</sup> (b) Galvanostatic cycling at 0.5C (within the 56 wt% S cathode) and (c) the capability to adsorb LiPSs of different carbon host materials with and w/o  $\text{CoS}_2$ .<sup>203</sup> (d) SEM and TEM pictures of carbon/ $\text{Co}_3\text{S}_4$  polyhedra as a host material for sulfur and their electrochemical performance at (e) high mass loading and (f) long-term cycling (53 wt% S within the cathode).<sup>228</sup> (a) Reproduced with permission from ref. 200. Copyright 2016, The Royal Society of Chemistry. (b and c) Reproduced with permission from ref. 203. Copyright 2016, Elsevier. (d–f) Reproduced with permission from ref. 228. Copyright 2017, Elsevier.





batteries<sup>236</sup> and was already commercialized in the first generation of Li-ion batteries.<sup>237</sup>  $\text{TiS}_2$  exhibits semi-metallic to metallic behavior depending on the state of lithiation and therewith fulfills the requirements as an additive for sulfur composites: (i) polarity and (ii) high electrical conductivity.

As one of the first groups, Garsuch *et al.* tested ball-milled sulfur/carbon/ $\text{TiS}_2$  composite electrodes and observed improvements in the cycle life with the addition of  $\text{TiS}_2$ .<sup>235</sup> The optimum composition was found to be 20 wt% of  $\text{TiS}_2$ . However, the specific capacity normalized to the active mass was reduced when  $\text{TiS}_2$  was added. It was proposed that the addition of  $\text{TiS}_2$  can enhance ionic and electrical conductivity in the cathode composite, but the surface needs to be tailored to electrically contact all sulfur. Su *et al.* also partially replaced the carbon additive by  $\text{TiS}_2$  within sulfur composite electrodes.<sup>238</sup> Similar to the observations made by Garsuch *et al.*,<sup>235</sup> the capacity based on the active mass was reduced by  $\text{TiS}_2$  addition, but the cycling stability increased.

Seh *et al.*<sup>214</sup> used a different design to incorporate  $\text{TiS}_2$  in  $\text{Li}_2\text{S}$  cathodes. They encapsulated  $\text{Li}_2\text{S}$  (particle size < 1  $\mu\text{m}$ ) in  $\text{TiS}_2$  with different thicknesses ranging from 10–50 nm through an *in situ* reaction of  $\text{TiCl}_4$  with  $\text{Li}_2\text{S}$  particles followed by a heat treatment to crystallize  $\text{TiS}_2$ . It was found that the charge transfer resistance and the potential barrier in the first charging process significantly decreased with  $\text{TiS}_2$  encapsulation. The initial capacity increased from 708  $\text{mA h g}^{-1}$  to 806  $\text{mA h g}^{-1}$  compared to bare  $\text{Li}_2\text{S}$  particles with an average capacity loss of 0.058% per cycle. The reason was found to be the high conductivity of  $\text{TiS}_2$  and the high affinity of  $\text{Li}_2\text{S}/\text{Li}_2\text{S}_n$  to  $\text{TiS}_2$  by several experimental techniques and DFT theoretical calculations. They also encapsulated  $\text{Li}_2\text{S}$  with  $\text{ZrS}_2$  and  $\text{VS}_2$ . The performance of the materials was comparable to the one with  $\text{TiS}_2$  indicating that these materials also show high affinity for LiPS species. The resulting electronic conductivities were  $4.0 \times 10^{-9}$  and  $3.8 \times 10^{-9} \text{ S cm}^{-1}$ , whereas the  $\text{Li}_2\text{S}@ \text{TiS}_2$  structure showed the highest conductivity of  $5.1 \times 10^{-3} \text{ S cm}^{-1}$ .

Ma *et al.*<sup>239</sup> prepared a  $\text{TiS}_2$  foam infiltrated with sulfur by an *in situ* reaction of a commercially available Ti metal foam with sulfur at 700 °C in a sealed quartz tube. The structure of the final electrode material can be sub-divided into three parts: a Ti metal core surrounded by a  $\text{TiS}_2$  film and sulfur. The 3D hybrid structure can store up to 40  $\text{mg cm}^{-2}$  of sulfur and exhibits a capacity of up to 30  $\text{mA h cm}^{-2}$  at a total electrode weight (including the current collector) and about 260  $\text{mA h g}^{-1}$  as a cathode composite. The capacity retention under these conditions was still impressively high and accounts to less than 0.3% per cycle.

Matsuyama *et al.* prepared amorphous  $\text{TiS}_3/\text{S}/\text{C}$  composite electrodes and found poor performance in Li-S batteries with liquid electrolytes when adding  $\text{TiS}_3$  to the electrode.<sup>240</sup> It was attributed to LiPS dissolution which is in contrast to other reports<sup>214,235–239</sup> as it evidences that the capability of  $\text{TiS}_3$  to capture LiPSs seems to be very low. However, a remarkable improvement could be achieved with solid electrolytes.

### 3.3 Molybdenum sulfide

Another promising metal sulfide additive is  $\text{MoS}_2$  offering high electrical conductivity and the binding energies of  $\text{Li}_2\text{S}$  to the

Mo-edge in the  $\text{MoS}_2$  structure of up to 4.48 eV (Table 3).<sup>202,220,241–245</sup> Note that  $\text{MoS}_2$  is not active in the potential range of sulfur (1.8–2.6 V vs.  $\text{Li}/\text{Li}^+$ ). Dirlam *et al.* fabricated sulfur/ $\text{MoS}_2$  and sulfur copolymer/ $\text{MoS}_2$  composite electrodes by facile dispersion of 2D  $\text{MoS}_2$  sheets in molten sulfur and ball milling.<sup>246</sup> A considerably enhanced cycle life and sulfur utilization were found with the composite prepared through dispersion in molten sulfur. Ghazi *et al.* coated  $\text{MoS}_2$  onto the separator instead of a direct addition to the sulfur cathode.<sup>247</sup> The modified side of the separator faced a conventional sulfur cathode, a mixture of carbon and sulfur, during cell tests vs.  $\text{Li}/\text{Li}^+$ . Greatly improved reversibility with a decay of only 0.083% per cycle at 0.5C was achieved exceeding the performance of a reference separator made of graphene oxide.

$\text{MoS}_2$  itself is also considered as a promising intercalation cathode as well as a conversion anode material. Recently, some groups used molybdenum sulfides as the initial precursor material to form a sulfur-based composite material after the first initial discharging process.<sup>194,206</sup> Balach *et al.* studied the irreversible electrochemical decomposition of  $\text{MoS}_2$  to  $\text{Li}_2\text{S}$  and Mo nanoparticles as a sulfur-based cathode showing typical sulfur electrochemical characteristics and performed *ex situ* measurements.<sup>206</sup> In contrast to commonly used ether-based electrolytes for Li-S batteries, the group successfully conducted reversible cycling in carbonate-based electrolytes which are actually well known to be incompatible with LiPSs. Despite using a cathode with an ultrahigh  $\text{Li}_2\text{S}$  loading of 10.7  $\text{mg cm}^{-2}$ , the cell delivered an average areal capacity of 7.5  $\text{mA h cm}^{-2}$  at a C-rate of 0.1. Furthermore, the  $\text{MoS}_2$ -derived  $\text{Li}_2\text{S}$  cathode was coupled with a lithiated silicon anode to assemble a Li-S full-cell providing an initial capacity of 780  $\text{mA h g}^{-1}$ . It was found that the polymeric gel-like solid-electrolyte interface (SEI) formed during the initial discharging process keeps LiPSs tightly embedded in the Mo/carbon matrix and thereby prevents the formed LiPSs from a dissolution into the electrolyte and finally a diffusion to the metal anode. This strategy may allow the usage of carbonate-based electrolytes which may allow the application of (safe) alternative anode materials (*i.e.* Si and Sn) instead of lithium metal.

Wang *et al.*<sup>202</sup> showed that the atomic sites on the crystal surface of a metal sulfide additive are highly important to capture LiPSs. They prepared differently shaped crystal surfaces with varying amounts of terrace or edge sites with  $\text{MoS}_2$  nanostructures (nanoparticles and vertically aligned 2D sheets) on CNFs and studied their electrochemical behavior as a positive current collector for LiPSs. It was experimentally found that the exposed crystal facet (Mo-rich or S-rich edge) of the  $\text{MoS}_2$  particle is highly important for an improved operation mode of Li-S batteries and as a catalyst. The best performance was achieved with vertically aligned  $\text{MoS}_2$  sheets which contain high amounts of Mo-rich edges. This observation was confirmed by DFT calculations. The high affinity of  $\text{Li}_2\text{S}$  to the Mo-edge of the  $\text{MoS}_2$  structure with a binding energy of 4.48 eV was reported while the sulfur-edge only offered 0.87 eV.

### 3.4 Other metal sulfides

There are several other metal sulfides which were investigated to boost the electrochemical performance of Li-S batteries, such



as  $\text{SnS}_2$ ,<sup>219,248,249</sup>  $\text{FeS}_2$ ,<sup>250</sup>  $\text{Bi}_2\text{O}_3$ ,<sup>221</sup>  $\text{NiS}_2$ ,<sup>212,251,252</sup>  $\text{NbS}_2$ ,<sup>253</sup>  $\text{WS}_2$ ,<sup>57,254</sup>  $\text{MnS}$ ,<sup>255</sup>  $\text{CuS}$ ,<sup>223</sup>  $\text{VS}_2$ ,<sup>256,257</sup> and  $\text{ZnS}$ .<sup>258</sup> Very interesting results have been obtained recently with  $\text{WS}_2$  independently by two different groups (Fig. 10). Using  $\text{WS}_2$  as a host or an additive in Li-S batteries, remarkable reversibility and sulfur utilization (about 95%) were reported by Lei *et al.*<sup>57</sup> (Fig. 10a–c) and Park *et al.*<sup>254</sup> (Fig. 10d and e), respectively. Lei *et al.* used  $\text{C@WS}_2$  as a host material for sulfur and obtained a discharge capacity of  $1581 \text{ mA h g}^{-1}$  at 0.1C with only 0.0072% capacity loss per cycle over 1500 cycles, the best degradation rate value reported so far.<sup>57</sup> By conducting DFT calculations, they found that particular short chain sulfides ( $\text{Li}_2\text{S}_2$  and  $\text{Li}_2\text{S}$ ) chemically interact with  $\text{WS}_2$ . For example, the binding energy of  $\text{Li}_2\text{S}_4$  is just 0.8 eV whereas for  $\text{Li}_2\text{S}$  1.45 eV was determined. Since these binding energies are lower compared to other metal sulfides (Table 4), sulfides with moderate binding energies in the range of  $0.8 \text{ eV} < E_b < 2.0 \text{ eV}$  were proposed to be the best choice for high performance Li-S batteries. This description is in agreement with the work of Park *et al.*,<sup>254</sup> who proposed a disproportion of long-chain PSs to short-chain PSs after trapping at the edge sites of  $\text{WS}_2$ . Both groups experimentally confirmed the high adsorption capability for LiPSs by visualization in a glass vial (Fig. 10c).

Li and co-workers prepared hollow carbon spheres filled with sulfur and different compositions of  $\text{SnS}_2$  nanoparticles ranging from 5 to 7 nm in size.<sup>249</sup> It was found that  $\text{SnS}_2$  nanoparticles enhance the life time of the cell, decrease charge transfer resistance, increase the diffusion of  $\text{Li}^+$  ions in the  $\text{Li}_2\text{S}$  composite and anchor LiPSs within the cathode. The optimum  $\text{SnS}_2$  concentration was found to be 10 wt%. Li *et al.* prepared both  $\text{SnS}_2/\text{S}/\text{C}$  and  $\text{SnO}_2/\text{S}/\text{C}$  composite electrodes.<sup>219</sup> The  $\text{SnS}_2$ -based composite showed considerably higher capacity and

slightly enhanced reversibility than the  $\text{SnO}_2$ -based composite, although the DFT calculated binding energy of  $\text{Li}_2\text{S}_4$  is higher to  $\text{SnO}_2$  than to  $\text{SnS}_2$  which is actually an indication of better reversibility. As a reason it was stated that the binding energy between  $\text{Li}_2\text{S}_4$  and  $\text{SnO}_2$  of 3.25 eV may have been too high causing the disruption of the  $\text{Li}_2\text{S}_4$  molecule which has been suggested by other groups as well.<sup>57</sup> The charge transfer resistance was lower in the case of  $\text{SnS}_2$  highlighting that strong interaction/adsorption may not be the most important parameter to enhance the electrochemical performance. More importantly, a balance between electrical conductivity, the charge transfer process and moderate LiPS adsorption may be crucial for improving the cell performance.

Another interesting metal sulfide used in Li-S batteries is  $\text{FeS}_2$ . It is widely available, very cheap and can retain the low cost advantage of Li-S batteries. For example, Zhang *et al.* showed that  $\text{FeS}_2$  used as an additive can chemically adsorb LiPSs and prevent diffusion to the anode.<sup>250</sup> It was evidenced that the binding of LiPSs involves the formation of a  $\text{Li}_2\text{FeS}_{2+n}$  complex through a radical reaction. By increasing the amount of  $\text{FeS}_2$  from 0 to 15 wt% within the electrode composite, the cycle life of the Li-S battery could be increased from 50 cycles to 200 cycles, which is attributed to the efficient adsorption of LiPSs within the  $\text{FeS}_2$ -containing cathode.

$\text{Bi}_2\text{S}_3$  was tested by Li *et al.* in sulfur composite electrodes for Li-S batteries prepared through a melting technique at  $280^\circ\text{C}$ .<sup>221</sup> It was found that this compound also seems to have very good capability to capture LiPSs, thereby anchoring LiPSs within the composite. The excellent affinity of LiPSs to  $\text{Bi}_2\text{S}_3$  was confirmed by first principles DFT calculations. They studied different amounts in the range of 10–20 wt% of  $\text{Bi}_2\text{S}_3$  and found the optimal performance in terms of capacity retention at 14

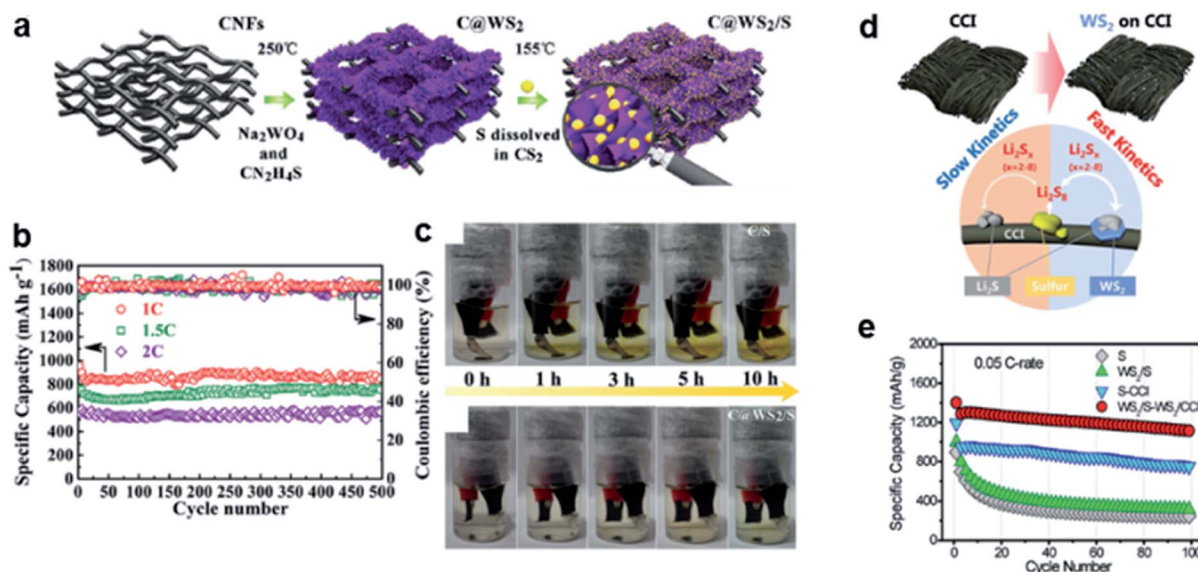


**Fig. 10** (a) Schematic illustration of the preparation of the CNFs/ $\text{WS}_2$  host material for sulfur, (b) its electrochemical performance (55 wt% sulfur;  $2 \text{ mg cm}^{-2}$ ; 1.7–2.7 V vs.  $\text{Li}/\text{Li}^+$ ) and (c) a visual demonstration of the adsorption capability for LiPSs with (bottom) and without  $\text{WS}_2$  (top) over galvanostatic discharge.<sup>57</sup> (d) Schematic illustration of the faster reaction kinetics with the  $\text{WS}_2$  support and (e) the electrochemical performance with and without the  $\text{WS}_2$  support in various cell configurations.<sup>254</sup> (a–c) Reproduced with permission from ref. 57. Copyright 2016, Wiley-VCH. (d and e) Reproduced with permission from ref. 254. Copyright 2017, Wiley-VCH.



and 19 wt% of  $\text{Bi}_2\text{S}_3$ . The first discharge capacity was up to  $1500 \text{ mA h g}^{-1}$  at 0.1C. However, it should be noted that  $\text{Bi}_2\text{S}_3$  contributes to the capacity in the chosen voltage window.

There are further studies dealing with  $\text{NiS}_2$ ,<sup>212,251</sup>  $\text{MnS}$ ,<sup>255</sup>  $\text{CuS}$ <sup>223</sup> and  $\text{ZnS}$ <sup>258</sup> as additive or host materials for sulfur composite electrodes. Except for  $\text{CuS}$ , all of these studies reported enhanced electrochemical performance in the presence of these metal sulfides. Among these reports,  $\text{NiS}_2$  seems to be a promising co-component for sulfur cathodes. In the same manner, it is mostly attributed to capturing LiPSs and anchoring them within the cathode. The major physical properties and their effect in sulfur composite electrodes are summarized in Tables 3 and 4, respectively.

It should be noted that chalcogenides also comprise selenides and tellurides. However, to the best of our knowledge, no reports about metal selenides and tellurides appeared yet utilizing these kinds of chalcogenides as hosts, additives or interlayers in sulfur cathodes or Li-S cells to enhance sulfur redox-reactions or anchoring LiPSs. This area may be worth exploring in the future.

## 4. Transition metal carbides (TMCs) and nitrides (TMNs) including 2-dimensional materials (MXenes)

### 4.1 Transition metal carbides (TMC)

In most transition metal carbides (TMCs) based on metals of the groups 6–8 of the periodic table of elements, carbon atoms are placed in interstitial sites in the metallic lattice. Thus, TMCs like *e.g.*  $\text{TiC}$ ,<sup>259–265</sup>  $\text{WC}$ <sup>261,266</sup> and  $\text{NbC}$ <sup>267</sup> exhibit metallic properties such as high electronic conductivity in the order of  $10^4 \text{ S cm}^{-1}$  and were recently investigated to enhance the performance of Li-S batteries. In this context, the effect of TMCs on the homogenous deposition of insoluble  $\text{Li}_2\text{S}$  at the sulfur electrode scaffold during discharging is regarded as a crucial issue.<sup>259,262,265</sup>

In 2016, titanium carbide nanoparticles started to be applied in sulfur electrodes.<sup>259–261</sup> In that regard, Salem *et al.* proposed that TMCs offer superior properties for electron transfer reactions involving LiPSs compared to transition metal oxides due to the greater density of states near the Fermi level as a result of the favorable interaction of d-electrons of the metal with the sp-electrons of the carbon.<sup>261</sup> Accordingly, WC and TiC nanoparticles with a diameter of 100 nm were investigated as an electrocatalyst for the LiPS reaction by experimental and theoretical methods. The improvement of the corresponding batteries was found to be based on the enhanced electron transfer reaction and the capability to adsorb LiPS intermediates, with better results for TiC than for WC. Experimental studies comparing  $\text{TiO}_2$ /carbon composites to analogous TiC/carbon composites confirmed the advantage of TiC over  $\text{TiO}_2$  components.<sup>259,263</sup> Using graphene or nanoparticle/graphene composites as a sulfur host, Peng *et al.* observed an increased number of nucleation sites of  $\text{Li}_2\text{S}$  with  $\text{TiO}_2$  nanoparticles but inhibited lateral growth.<sup>259</sup> However, TiC nanoparticles enabled a high number of nucleation sites and full surface coverage with  $\text{Li}_2\text{S}$  films of increased thickness due to enhanced radial growth

of  $\text{Li}_2\text{S}$ . Furthermore, reduced charge transfer resistance and a shift in the peak potential in cyclic voltammetry were measured suggesting that conductive TiC facilitates both the liquid–liquid transformation of LiPSs and the liquid–solid nucleation/growth of  $\text{Li}_2\text{S}$ . After 100 cycles at 0.2C, a reversible capacity of  $670 \text{ mA h g}^{-1}$  was obtained for a considerable sulfur loading of  $3.5 \text{ mg cm}^{-2}$ . Besides TiC nanoparticle/graphene host<sup>259</sup> and interlayer<sup>264</sup> materials, TiC nanoparticles were combined with CNFs<sup>262,265</sup> and mesoporous CMK-3<sup>263</sup> for application as sulfur host materials.

Cai *et al.* synthesized nanocrystalline NbC by a magnesiothermic reaction at  $600^\circ\text{C}$  and coated the material on a membrane to employ it as an interlayer in Li-S batteries.<sup>267</sup> Using a cathode with a sulfur loading of  $1.5 \text{ mg cm}^{-1}$ , a reversible capacity of  $988 \text{ mA h g}^{-1}$  was achieved after 100 cycles at 0.2C and a capacity of  $\approx 500 \text{ mA h g}^{-1}$  after 1500 cycles at 2C, corresponding to a degradation rate of 0.04% per cycle. WC was used as an additive for the positive electrode and compared to  $\text{WO}_3$  showing that batteries with WC exhibit a much higher discharge capacity in the region of the second voltage plateau and an improved cycling stability.<sup>266</sup> The difference in the capacity becomes even more distinct for higher current rates. The authors concluded that WC promotes the disproportionation of LiPSs and thus enables the repeated utilization of “recycled” long-chain LiPSs in the reduction process. This catalytic property is attributed to strong sulfophilic surface moieties capturing soluble LiPS species by representing tungsten disulfide-like surfaces because nanoscale layers of specifically adsorbed S atoms on WC were evidenced by XPS measurements. A comparative study on TMC nanoparticle/CNF electrodes revealed the superior performance of tungsten semicarbide ( $\text{W}_2\text{C}$ ), reaching a capacity of  $1128 \text{ mA h g}^{-1}$  after 200 cycles at 0.2C and a degradation rate of 0.07% per cycle, over  $\text{Mo}_2\text{C}$  and TiC.<sup>265</sup> In line with DFT calculations of stable configurations of  $\text{Li}_2\text{S}_6$  on the three metal carbides,  $\text{W}_2\text{C}$  nanoparticles are assumed to function as an oxidation and reduction catalyst, where  $\text{Li}_2\text{S}_n$  diffusion from the active sites to the carbon matrix is facilitated by a moderate adsorption energy of  $\text{W}_2\text{S}$  to sulfidic species, resulting in the homogenous deposition of sulfur species on the entire carbon matrix.

### 4.2 2-Dimensional carbides of the MXene class

The materials class of MXenes comprises 2-dimensional (2D) transition metal carbides, carbonitrides and nitrides, which often exhibit hydrophilic surfaces containing exposed redox-active transition metal atoms and electrical conductivity in the range of  $10^4 \text{ S cm}^{-1}$ .<sup>268</sup> The name MXene refers to the similarities to graphene and the precursor phases of layered ternary carbides and nitrides (MAX phases).<sup>269</sup> MXenes are described by the general formula  $\text{M}_{n+1}\text{X}_n\text{T}_x$  ( $n = 1–3$ ), where M represents group 4 to 6 transition metals, X carbon and/or nitrogen and T terminal surface groups, mostly hydroxyl ( $-\text{OH}$ ), oxo ( $-\text{O}$ ) or fluoro ( $-\text{F}$ ) groups, with  $n+1$  layers of M covering  $n$  layers of X. The mixture of  $-\text{OH}$ ,  $-\text{O}$  and  $-\text{F}$  terminations on the surface results from the synthesis methods of selective etching of





certain metal atoms forming layers which interleave the layers of TMC and TMN, in which hydrofluoric acid is applied.<sup>268</sup>

Liang *et al.* proposed the use of 2D  $\text{Ti}_2\text{C}$  as a host material for sulfur for the first time and demonstrated promising results.<sup>270</sup> Exfoliated and delaminated  $\text{Ti}_2\text{C}$  nanosheets were prepared with surface areas of  $20.2 \text{ m}^2 \text{ g}^{-1}$  and  $67.9 \text{ m}^2 \text{ g}^{-1}$ , respectively. Compared to conventional porous carbon hosts, this surface area is very low and intuitively a poor electrochemical performance would be expected as a good electrical contact cannot be established with sulfur. However, the delaminated  $\text{Ti}_2\text{C}$  with infiltrated sulfur shows an excellent electrochemical performance. The discharge capacity was measured to up to  $1400 \text{ mA h g}^{-1}$  at  $0.05\text{C}$  (sulfur content = 56 wt%; sulfur loading =  $1 \text{ mg cm}^{-2}$ ) and the decay rate over 650 cycles at  $0.5\text{C}$  was only 0.05% per cycle. The authors attributed the superior performance to the chemisorption of LiPS intermediates on the  $\text{Ti}_2\text{C}$  surface which creates S–Ti–C bonds facilitating electron transfer and redox reaction kinetics. This assumption was confirmed by XPS measurements showing evidence for such redox behavior. It is important to note that host materials with low surface areas are able to provide high rate performance for sulfur cathodes. These materials are attractive for high energy batteries as they help to increase the tap density and therewith the volumetric as well as specific energy density. Following up on the work of Liang *et al.*, several other studies investigated MXenes and corresponding composites as a sulfur host material,<sup>271–274</sup> separator coating<sup>275,276</sup> or applied MXenes in both functions.<sup>277</sup>

Bao *et al.* reported a  $\text{TiC@mesoporous carbon}$  composite infiltrated with sulfur for positive electrodes of Li–S batteries.<sup>271</sup> High discharge capacities of up to  $1225 \text{ mA h g}^{-1}$  (at  $0.5\text{C}$  and 58 wt% sulfur within the entire cathode) were achieved with a capacity loss of 0.19% per cycle at  $0.5\text{C}$ . The enhanced performance compared to the control electrode was explained by the hydrophilic surface characteristics of  $\text{Ti}_3\text{C}_2\text{T}_x$ . However, Liang *et al.* proposed in a continued work to their first paper about MXenes that the strong interaction of LiPSs and the surface groups is more complex and originates from a dual mode mechanism.<sup>274</sup> Initially, a cleavage of Ti–OH occurs and results in the formation of thiosulfates. The created vacancies on  $\text{Ti}_3\text{C}_2$  are filled by a Lewis-base reaction of LiPSs to form Ti–S bonds. A demonstrative representation is shown in Fig. 11a.

For the application as a sulfur host material, the utilization of the functional surfaces of 2D exfoliated MXene materials may be interfered by the usually observed stacking of the metal carbide sheets through van der Waals forces and hydrogen bonding. Accordingly, rGO nanosheets were employed as spacers yielding a 3D morphology with accessible 2D surfaces of multilayer  $\text{Ti}_3\text{C}_2\text{T}_x$  nanosheets sandwiched between rGO layers. After solution infiltration of sulfur, the composite achieved an initial capacity of  $1144 \text{ mA h g}^{-1}$  at  $0.5\text{C}$  which decreased to  $878 \text{ mA h g}^{-1}$  after 300 cycles corresponding to a degradation rate of 0.08% per cycle.<sup>273</sup> Furthermore, the same group reported a crumpled N-doped MXene nanosheet host material which was synthesized by thermal annealing of a coagulated precipitate of  $\text{Ti}_3\text{C}_2\text{T}_x$  flakes and positively charged melamine as an N-source and spacer. With a high sulfur loading of  $5.1 \text{ mg cm}^{-2}$ , the reversible capacity and the degradation rate after 500 cycles at

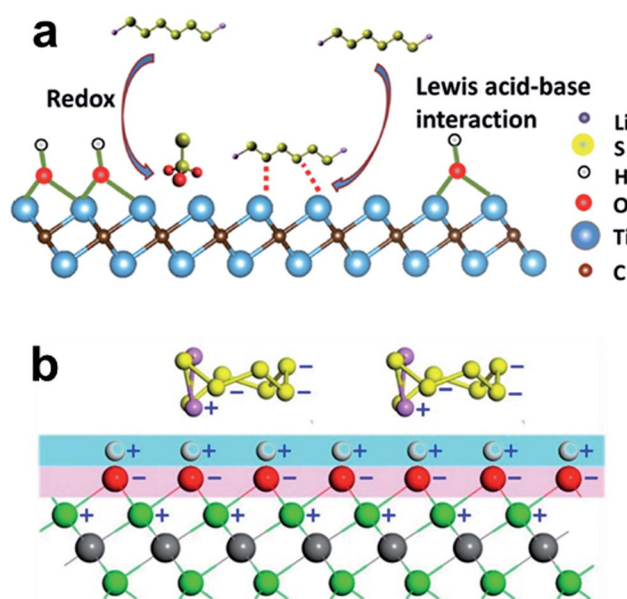


Fig. 11 (a) A schematic representation of the dual mode mechanism of the strong interaction of LiPSs on  $\text{Ti}_3\text{C}_2\text{OH}$  MXenes<sup>274</sup> and (b) scheme of charged atoms in LiPS and MXenes, where “+” represents the electropositive atoms and “–” represents the electronegative atoms with Ti: green, S: yellow, Li: Purple, O or F: red and H: white.<sup>278</sup> (a) Reproduced with permission from ref. 274. Copyright 2016, Wiley-VCH. (b) Reproduced with permission from ref. 278. Copyright 2017, American Chemical Society.

$0.2\text{C}$  were  $588 \text{ mA h g}^{-1}$  and 0.05% per cycle. The interaction of Li- and N-atoms was proven by XPS measurements conducted after the discharge.<sup>272</sup> The suggestion to use MXenes for separator coatings in Li–S batteries is based on the ability to obtain very thin and homogenous closed layers of electrically conducting 2D nanosheets with highly polar surface sites.<sup>275,276</sup> Comparing a  $\text{Ti}_3\text{C}_2\text{T}_x$  covered glass fiber separator to a graphene coated one, Lin *et al.* observed a higher initial discharge capacity for the graphene layer but lower cycling stability.<sup>275</sup> Corresponding *ab initio* calculations showed that  $\text{Ti}_3\text{C}_2$  exhibits much stronger interactions with LiPSs than graphene, whereas the Ti–S interactions are, however, weakened due to strongly polar F- or OH-functions. Therefore, the authors expect an additional performance improvement, if the number of such functional groups would be reduced.

Further computational studies applying DFT calculations enabled a more differentiated view on the role of surface functionalities on MXenes for Li–S batteries.<sup>278–282</sup> For bare  $\text{Ti}_2\text{C}$  surfaces, Rao *et al.* calculated distances of S atoms of LiPS and Ti atoms of MXenes in the range of Ti–S bond lengths in  $\text{TiS}_2$  crystals, corresponding to strong interactions.<sup>278</sup> Moreover, it was found for defect sites (representing the surface partially uncovered with functional groups) that the interaction of Ti and S atoms is strong enough to break the covalent S–S bond that constitutes the S chain of LiPS.<sup>280,281</sup> In contrast to Lin *et al.*,<sup>275</sup> this was interpreted as a drawback because active sulfur material is irreversibly lost.<sup>280,281</sup> However, continued trapping of sulfur is not assumed as the adsorption energy of a second S atom adsorbed on the previously trapped S atom is smaller than



the formation energy of octet sulfur.<sup>280</sup> The strong attraction of Ti and S is reduced for O- and F-termination groups as the repulsive force from O and F, which have more electrons around their surfaces, increases.<sup>278</sup> As seen in Fig. 11b, the repulsive forces will be slightly shielded by H atoms, if the surface is functionalized with OH groups.<sup>278</sup> However, H atoms can be relatively easily replaced in line with the known behavior of an increasing number of O groups and a decreasing number of OH groups observed, if long-chain LiPS are introduced. While the interaction of LiPS with F terminations is relatively weak suggesting an anchoring mechanism, the interaction with  $\text{Ti}_2\text{CO}_2$  is certainly stronger due to attractions between Li and O atoms leading to elongation of Li-S bonds.<sup>281</sup> The electronic conductivity of MXenes is not affected by LiPS adsorption as the band gaps do not obviously change or are even narrowed as for F-doped surfaces.<sup>278</sup>

In summary, 2D MXene materials are very promising for application in Li-S batteries as they combine the properties of high electrical conductivity and surfaces suitable for anchoring or decomposing LiPS species. In this regard, it would be interesting to investigate the potential electrocatalytic function of MXenes towards the conversion of LiPS intermediates. The nanosheet morphology of MXene materials enables their use for thin separator coatings and to achieve a high exposure of their functional surface to the sulfur species, if restacking is omitted. Until now, nearly all reports employing MXenes for Li-S batteries have dealt with titanium carbide-based materials. So, for future research, 2D derivatives of further TMCs, transition metal carbonitrides and nitrides might be highly interesting. Accordingly, the following section discusses “conventionally” nanostructured representatives of the latter material's class.

### 4.3 Transition metal nitrides (TMNs)

Transition metal nitrides (TMN) of the groups 4 to 6 of the periodic table of elements, are, similar to the discussed TMCs, interstitial compounds with high electronic conductivity, good chemical stability and polar metal-nitride (M-N) bonds. In particular, TiN<sup>283–294</sup> and VN<sup>295–301</sup> have recently gained considerable attention and were investigated with promising results. In 2016, Mosavati *et al.* suggested to apply TiN nanoparticle powder as a material for the positive electrode to promote LiPS conversion reactions achieving a capacity of 1040 mA h g<sup>-1</sup> after 100 cycles at 0.1C.<sup>283</sup> Goodenough and co-workers prepared a mesoporous TiN host material with a specific surface area of 70 m<sup>2</sup> g<sup>-1</sup> through reduction of ZnTiO<sub>3</sub> with hot ammonia gas.<sup>284</sup> The TiN host material was infiltrated with sulfur and tested in Li-S batteries. For comparison, a TiO<sub>2</sub> host material was prepared in a similar way and infiltrated with sulfur. A high capacity of 1121 mA h g<sup>-1</sup> at 0.1C (50 wt% sulfur content in the cathode) and a decay rate of 0.07% per cycle over 500 cycles were achieved with TiN exceeding the performance of the TiO<sub>2</sub> reference cathode. The results were mainly attributed to the excellent electronic conductivity, robust host framework and good adsorption capabilities for LiPSs.<sup>284</sup> Deng *et al.* prepared hollow, porous TiN tubes through a sol-gel process and tested the final cathodes with a sulfur loading of 1 mg cm<sup>-2</sup> at 52 wt%

sulfur content.<sup>285</sup> An initial capacity of 1481 mA h g<sup>-1</sup> at 0.1C was observed and a reversible capacity of 1020 mA h g<sup>-1</sup> at a C-rate of 0.2 was demonstrated. The capacity loss per cycle was reported to be 0.015%, which is one of the best reported values so far.<sup>55,57–59</sup> Hao *et al.* prepared TiN/S composite electrodes by simple mixing of 30 nm TiN nanoparticles with sulfur.<sup>286</sup> The demonstrated electrochemical performance was not as good as reported in other studies, but the simplicity of the approach makes it relatively attractive. A heterogeneous catalytic effect of TiN to promote the redox kinetics of LiPSs was proposed by Jeong *et al.* in a combined computational and experimental study.<sup>288</sup> The very strong interaction of a cyclooctasulfur molecule on the TiN surface accounting to 6.6 eV was calculated, which is far higher than that reported for various TiO<sub>x</sub> modifications. TiN was furthermore applied for separator coatings<sup>287,290,291</sup> in combination with TiO<sub>2</sub><sup>290</sup> or rGO, yielding a reversible capacity of 550 mA h g<sup>-1</sup> at 2C after 1000 cycles in the latter case.<sup>287</sup>

Mosavati *et al.* tested various TMNs including WN nanoplates, Mo<sub>2</sub>N nanorods and VN nanoparticle as additives within the sulfur cathode to boost the performance of Li-S batteries.<sup>296</sup> The differently shaped TMNs were synthesized through a wet chemical process and an annealing step. Interestingly, results at an ultrahigh sulfur loading of up to 12 mg cm<sup>-2</sup> were demonstrated which makes the study attractive for practical application. Best performance was obtained using WN which was attributed to strong S-W-N interactions. In contrast, VN showed a quite poor performance. However, Ma *et al.* reported a VN host material with a highly porous hollow structure delivering a capacity of 837 mA h g<sup>-1</sup> after 1000 cycles at 1C for a sulfur loading of 1.2 mg cm<sup>-2</sup>.<sup>298</sup> Further studies on VN/carbon host materials researched carbon encapsulated VN nanowires,<sup>297</sup> porous carbon/VN fibers,<sup>300</sup> and composites of VN nanoentities and N-doped carbon.<sup>299,301</sup> Sun *et al.* measured a reversible capacity of 1252 mA h g<sup>-1</sup> after 100 cycles at 0.2C for a porous VN nanoribbon/graphene composite due to fast redox reaction kinetics.<sup>295</sup> Ren *et al.* also intended to utilize the properties of a functional catalyst in Li-S batteries and synthesized cobalt-doped VN yolk-shell nanospheres encapsulated in a thin layer of N-doped carbon.<sup>299</sup> Investigating a third TMN species, mesoporous Co<sub>4</sub>N spheres achieved by nitridation of Co<sub>3</sub>O<sub>4</sub> were applied as a host material giving a capacity of 1100 mA h g<sup>-1</sup> at 0.5C after 100 cycles for a sulfur content of 72 wt%.<sup>302</sup>

Undoubtedly, TMNs, TMCs and, specially, MXenes for sulfur cathodes are a very young topic with raising interest.<sup>263</sup> We believe that this material class is an attractive candidate to improve the capacity retention and lifespan of Li-S batteries.

## 5. Metal-organic frameworks (MOFs) and other metal-complex based compounds

Metal complexes consist of a metallic center and surrounding ligands typically having a lone pair of electrons to form coordinative bonds to metal ions or atoms. In MOF structures, a network of repeating coordination entities features (potential)

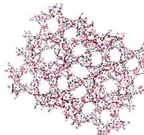
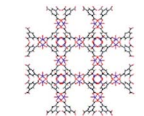
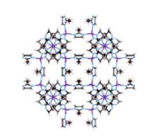
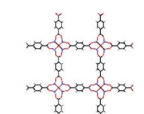
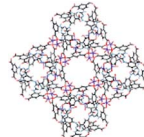


spatial voids, called pores, in a thermally stable crystalline framework structure comprising metal ions or metal complexes as centers and organic ligands, called linkers, with two or more functional groups to form coordinative bonds to several centers.<sup>303</sup> The shape and possible chemical functionalities of the highly regular MOF pores depend on the particular metallic center(s), the organic linker(s) and the resulting framework structure and thus, these properties are designable. Due to its large pores with small apertures and the polar character of the metal center–ligand bonds, Demir-Cakan *et al.* used a mesoporous chromium trimesate denoted as MIL-100(Cr) (Table 5) as the first example of a MOF-based sulfur host in Li–S batteries.<sup>304</sup> In this study, the cycling stability increases remarkably compared to mesoporous carbon or polar silica materials as the confinement in the MOF pores strongly suppresses the diffusion of LiPS from the host matrix. Further research also focuses on utilizing the Lewis acid function of coordinately unsaturated metal sites of certain MOFs to interact with LiPS anions<sup>305–309</sup> as well as the Lewis base function of certain linker molecules to interact with Li<sup>+</sup> cations.<sup>308,310,311</sup> In this section, we will summarize recent findings concerning the use of MOFs and other metal complexes in Li–S batteries

highlighting remarkable achievements regarding the cycle life and the underlying mechanistic principles of general relevance in understanding the role of metal-containing compounds in Li–S batteries. In this regard, the highly ordered and tunable framework structure allows for well-designed systematic studies. Table 5 aims to give an overview on widely researched compounds of this material class and their structural properties related to performance parameters achieved in Li–S batteries. Moreover, we discuss application-relevant aspects regarding the thermal, chemical and electrochemical stability of MOFs as well as their electrically insulating nature with respect to the influence of particle size and conjunction to conductive additives or matrices in composite materials on capacity and rate capability.

In Li–S batteries, MOFs are mostly employed as a sulfur host material. In this regard, it is important to introduce sulfur properly into the pores of a MOF which is commonly realized by melt diffusion into an activated MOF material. In some cases, vapor phase infusion,<sup>318</sup> infiltration of sulfur dissolved in CS<sub>2</sub><sup>313</sup> or encapsulation of sulfur nanoparticles by MOF synthesis in solution<sup>314</sup> have been used. Wang *et al.* observed a much lower cycling stability, if they use HKUST-1 (copper benzene tri-carboxylate)<sup>305</sup> or ZIF-8 (zeolitic imidazolate framework)<sup>315</sup> as

**Table 5** Selected MOF compounds studied for the application as a sulfur host material in Li–S batteries. Framework structure representations were prepared with VESTA software (©2006–2018, Koichi Momma and Fujio Izumi)

Metal-organic framework (MOF)	Framework structure	Surface area and pore volume	Initial capacity [mA h g <sup>−1</sup> ]	Reversible capacity [mA h g <sup>−1</sup> ]	Current rate <sup>a</sup>	Cycle number	Degradation rate per cycle [%]	Sulfur content <sup>b</sup> [wt%]	Sulfur loading [mg cm <sup>−2</sup> ]	Ref.
MIL-100 (Cr): [Cr <sub>3</sub> F(H <sub>2</sub> O) <sub>3</sub> O(BTC) <sub>2</sub> ] <sub>n</sub>		1485 m <sup>2</sup> g <sup>−1</sup> 0.95 cm <sup>3</sup> g <sup>−1</sup>	1580	450	0.1C	60	1.2	N/A	N/A	304
HKUST-1(Cu): [Cu <sub>3</sub> (BTC) <sub>2</sub> ] <sub>n</sub>		1500 m <sup>2</sup> g <sup>−1</sup> 0.67 cm <sup>3</sup> g <sup>−1</sup>	1498	500	0.1C	170	0.39	20	0.5	305
		N/A	431	286	0.5C	300	0.11	30	N/A	312
		1263	1263	681	0.2C	500	0.09	40	1.0	313
		143 m <sup>2</sup> g <sup>−1</sup> 0.16 cm <sup>3</sup> g <sup>−1</sup>	≈ 1050	≈ 780	0.2C	1000	≈ 0.03	N/A	N/A	314
ZIF-8 (Zn): [Zn(MeIm) <sub>2</sub> ] <sub>n</sub>		N/A	≈ 1200	510	0.1C	100	≈ 0.6	14	N/A	315
		0.70 cm <sup>3</sup> g <sup>−1</sup>	738	553	0.5C	300	0.083	30	N/A	312
		1309 m <sup>2</sup> g <sup>−1</sup> 0.64 cm <sup>3</sup> g <sup>−1</sup>	1600	380	0.05C/0.1C	25	2.5	N/A	N/A	316
		N/A	≈ 1200	598	0.2C	50	≈ 1.0	40	10	313
		919 m <sup>2</sup> g <sup>−1</sup> 0.70 cm <sup>3</sup> g <sup>−1</sup>	≈ 1250	750	0.2C	1000	≈ 0.04	N/A	N/A	314
MOF-5 (Zn): [Zn <sub>4</sub> O (BDC) <sub>3</sub> ] <sub>n</sub>		684 m <sup>2</sup> g <sup>−1</sup> 0.42 cm <sup>3</sup> g <sup>−1</sup>	1476	609	0.2C	200	0.29	35	0.6	317
		N/A	≈ 1200	746	0.2C	50	≈ 0.76	40	1.0	313
Cu-TDPAT: [Cu <sub>3</sub> (TDPAT)(H <sub>2</sub> O) <sub>3</sub> ] <sub>n</sub>		1473 m <sup>2</sup> g <sup>−1</sup> 0.55 cm <sup>3</sup> g <sup>−1</sup>	820	745	1C	500	0.02	40	1.2	308

<sup>a</sup> 1C = 1674 mA g<sup>−1</sup>. <sup>b</sup> Current collector substrate excluded.





MOF-based additives by just mechanically mixing them with sulfur instead of applying the melt diffusion process, suggesting sulfur confined inside the framework pores as a key aspect for increasing the cycle life. In line with these conclusions, the ability of the positive electrode to confine LiPSs was found to be more relevant than the electrode conductivity by comparing a Ni-MOF to an isostructural Co-MOF.<sup>306</sup> While these MOFs only differ in the metal ions, the interaction of the Ni ions and LiPSs is stronger than that for Co ions as investigated by DFT calculations leading to improved cycling performance for the Ni-MOF host (under similar initial capacities) even though the electronic conductivity of the Co-MOF is higher. This finding suggests that performance enhancement due to electrocatalytic processes related to enhanced charge transfer, as reported for other metal-containing materials discussed in this review, does not apply to MOF hosts.

As mentioned earlier, the electrical conductivity of MOFs is generally very low. Therefore, it is assumed that MOF host cathodes are based on electron tunneling through an insulating layer with a thickness of several nanometers to a conductive carbon matrix.<sup>304</sup> Thus, a threshold amount of conductive additive or the use of MOF/conductive matrix composite materials is necessary. Electrochemical processes involving charge transfer only occur near the interface of MOF particles and conductive material, where electrons, sulfur and Li<sup>+</sup> ions from the electrolyte are available.<sup>312</sup> A rotating-ring disk electrode (RRDE) study on the mechanism of the conversion reaction in Li-S batteries conducted by Lu *et al.* reveals how the MOF host electrodes may possibly work.<sup>319</sup> They show that the electrochemical steps of the sulfur reduction exhibit fast reactions kinetics with 4 to 5 transferred electrons accounting for about one quarter of the total capacity. The complete conversion can be only achieved *via* chemical reactions, such as disproportionation and chain growth, which reform the electrochemically reducible LiPS species and exhibit slow reaction kinetics. In this respect, low-dielectric solvents as 1,3-dioxolane/dimethoxyethane mixtures and the related poor stabilization of certain ionic species play a significant role. Likely, the electrochemical processes occur near the MOF/conductive material interface while the chemical processes can also occur further away utilizing the electronically uncontacted sulfur located in the host matrix. However, the strong confinement of LiPSs in the MOF host ensures that the chemical conversion steps occur at the cathode. Thus, re-generated reducible LiPSs diffuse to interfaces at the conductive material where such species are consumed by electrochemical reduction during discharge. In other words, LiPSs diffuse following the concentration gradient within the MOF host to the electrochemical reaction interface while the competing diffusion process to the bulk electrolyte outside the host matrix is suppressed due to the stabilizing interactions between LiPSs and the MOF matrix. Accordingly, in various articles, an initial fade in capacity over the first cycles is ascribed to sulfur on the outer surface of MOF crystals which was not introduced into the pores and therefore causes un-confined LiPS.<sup>306,313,315</sup> Nevertheless, an activation process with increasing capacity in the initial period until reaching a maximum also often occurs

and is attributed to proceeding wetting of the MOF interior by dissolved LiPSs.<sup>306,312,320,321</sup>

The mechanistic understanding also explains further characteristics observed in investigations on MOFs as sulfur hosts. For instance, cathode composites made from MOFs grown on CNTs showed higher capacities, especially at high current rates, compared with conventional mixed sulfur-infused MOFs/CNT positive electrodes.<sup>313,316</sup> The MOF/conductive additive conjunction and thus the contact area determine the capacity at certainly high enough current rates at which the kinetical limitation caused by slow chemical reactions restricts sulfur utilization. According to the described mechanism, the rate capability is enhanced, if a high interfacial area of the sulfur-hosting MOF phase and electron conducting phase is provided and short diffusion lengths are realized, ensuring fast transport of LiPSs to further sulfur species inside the MOFs for chemical reactions as well as fast transport of re-formed reducible LiPSs to the electron transferring interface. Thus, improved capacity and rate capability are obtained for smaller MOF crystal sizes or an increased amount of conductive additive.<sup>304,312,313,320</sup> Furthermore, Zhou *et al.* reported that the considerably varying charge transfer resistance for different MOF hosts does not affect the performance of Li-S batteries.<sup>312</sup> This observation emphasizes the rate-determining role of chemical reactions and transport in the inner MOF pores further off the interface. In conclusion, the proper functioning of a sulfur electrode based on a MOF host material especially relies on the superior trapping ability of MOF pores enabling high capacity by confining soluble chemically reactive LiPSs and re-formed reducible LiPSs close to both the MOF-based host matrix and the electrochemical reaction interface. The physical and chemical LiPS-trapping abilities of the MOF structure are able to prevent LiPS leakage even in the presence of large quantities of such species due to increased and fast formation of LiPSs, which have to undergo slow chemical reactions to provide for further discharge. Therefore, an excellent recovery after applying high current rates can be achieved.

Besides the physical confinement of LiPSs in MOF pores, Wang *et al.* intended to make use of the Lewis acidic function of coordinatively unsaturated (open) Cu<sup>2+</sup> sites of a well-known copper benzene tricarboxylate (Cu-BTC) framework (HKUST-1, Table 5) to bind LiPS anions.<sup>305</sup> The initial capacity of  $\approx 1500$  mA h g<sup>-1</sup> decreased to 500 mA h g<sup>-1</sup> after 50 cycles at 0.1C and remained at around 500 mA h g<sup>-1</sup> for another 120 cycles, corresponding to an overall degradation rate of 0.4% per cycle. Later, it was also shown that a high density of Cu-rich surface defects improves the capacity and the long term stability.<sup>322</sup> A comprehensive study on Ni-BTB-BP (BTB = benzene-1,3,5-tribenzoate; BP = 4,4'-bipyridyl), a MOF with a high pore volume of 2.15 cm<sup>3</sup> g<sup>-1</sup> and well-connected meso- (diameter: 2.8 nm) and micropores (diameter: 1.4 nm), was reported by Xiao and co-workers.<sup>306</sup> Ni-BTB-BP with Ni<sup>2+</sup> centers coordinates LiPS anions as axial ligands achieving a degradation rate of 0.11% per cycle for 100 cycles at 0.1C. XPS measurements revealed a lowered binding energy of Ni<sup>2+</sup> due to interaction with LiPS anions, while DFT investigations showed that a sulfur atom on one end of the LiPS chain coordinates to Ni<sup>2+</sup> centers of the



MOF with binding energies increasing with the chain length.<sup>306</sup> By computational screening of 16 metal-substituted analogues of MOF-74 (with a 2,5-dioxido-1,4-benzenedicarboxylate base), which are known for the highest density of open metal sites, a Ni-organic framework (MOF-74 (Ni)) was identified as a promising sulfur host regarding the ability to anchor  $\text{Li}_2\text{S}_4$  and  $\text{Li}_2\text{S}$  species.<sup>323</sup> As seen in Fig. 12, the sulfur atoms of the LiPSs interact with the metal ion centers of MOFs while terminal Li atoms are localized adjacent to oxygen atoms which are the nearest neighbors of the unsaturated metal sites. As the interactions of LiPSs and the MOFs are much stronger than that of elemental sulfur and the MOFs, Lewis acid-base interactions are assumed for LiPSs and van der Waals interactions for  $\text{S}_8$ .<sup>323</sup> Accordingly, the shifting of the  $\text{S}_{2p}$  signal to lower energies in XPS measurements, a higher sublimation temperature of sulfur, and color changes of the infused MOF powders in experimental investigations have been reported for sulfur-MOF composite cathodes.<sup>304,305,308,317,318</sup> Wang *et al.* investigated the effect of the number of available Lewis acidic sites.<sup>307</sup> They used mixed metal-organic frameworks (MMOFs) consisting of  $\text{Zr}_6(\text{OH})_4\text{O}_4$  clusters linked by porphyrin ligands which then can contain additional metal ions chelated by planar N atoms of the porphyrin molecules. Thus, three MOF compounds only differing in the porphyrin center were tested as sulfur hosts providing no, one ( $\text{FeCl}$ ) or two ( $\text{Cu}^{2+}$ ) Lewis acidic sites. For the Fe- and Cu-containing MMOFs, high cycling stability, rate capability and recovery after applying higher C-rates were obtained. Yet,  $\text{Cu}^{2+}$  and its two Lewis acidic sites per ion were shown to be superior to  $\text{FeCl}$  and achieved a capacity degradation of 0.07% per cycle from the 10<sup>th</sup> to the 200<sup>th</sup> cycle at 0.5C with a reversible capacity of 704  $\text{mA h g}^{-1}$ . In addition to MOFs, the Lewis acidic sites of other coordination compounds, such as  $\text{Na}_2\text{Fe}[\text{Fe}(\text{CN})_6]$ ,<sup>324</sup> a Prussian blue analogue, make these compounds interesting as sulfur host materials.<sup>324,325</sup>

Besides the Lewis acidic functionality, the LiPS trapping capability of MOFs can be tuned by introducing Lewis base properties due to the organic linker molecules. Park *et al.* compared isostructural zirconium-organic frameworks MOF-867 (Table 5),<sup>310</sup> achieving 790  $\text{mA h g}^{-1}$  reversible capacity, and UiO-67, achieving only 600  $\text{mA h g}^{-1}$ , which are based on

a similar linker comprising two  $\text{sp}^2$  nitrogen atoms (MOF-867) or no nitrogen atoms (UiO-67). The same trend was observed for IRMOF-10 compounds with and without N-containing linkers. In an *in situ* spectroelectrochemical investigation, the adsorption intensities for the N-containing MOF-867 host cathode increased during discharge and returned to their initial intensities during charging while the adsorption intensities of the UiO-67 cathode remains unchanged during the whole time. XPS and FTIR measurements provided further proof for the Lewis acid-Lewis base interactions of Li ions of  $\text{Li}_2\text{S}_4$  and  $\text{sp}^2$ -hybridized nitrogen atoms of the organic ligand. The concept of Lewis base ligands for chemical adsorption of LiPSs was also applied to functional separator coatings<sup>311,326,327</sup> in Li-S batteries, *e.g.* using a 2D coordination framework comprising phosphate groups.<sup>311</sup> Regarding MOFs as a sulfur host material, the combination of both open metal sites and N-containing linkers in the cage-like Cu-TDPAT (TDPAT = 2,4,6-tris(3,5-dicarboxylphenylamino)-1,3,5-triazine) framework (Table 5) achieved an outstanding cycling stability with a reversible capacity of 745  $\text{mA h g}^{-1}$  at 1C after 500 cycles, corresponding to a degradation rate of  $\approx 0.02\%$  per cycle.<sup>308</sup> The MOF host material was filled with  $\approx 50$  wt% of sulfur which results in a sulfur content of 40 wt% in the cathode (excluding the current collector) and a sulfur loading of 1.2  $\text{mg cm}^{-2}$ .

Zhou *et al.*<sup>312</sup> reported that the capacity fading in Li-S batteries employing MOF hosts had seem to be directly related to the aperture of the pores with enhanced stability for smaller "pore entrances" (ZIF-8 (Zn): 3.4 Å,<sup>328</sup> MOF-5 (Zn): 8.0 Å,<sup>329</sup> MIL-53 (Al): 8.5 Å,<sup>330</sup> and HKUST-1 (Cu): 9.0 Å<sup>331</sup>). However, the examined MOF materials also differ in other properties, *e.g.* structure type, metallic center, linker molecules and crystal size. Moreover, in contrast, Mao *et al.* observed a reduced cycle life for ZIF-8 (Zn) and MOF-5 (Zn) compared to HKUST-1 (Cu) based electrodes associated with more sulfur dispersed on the external MOF surface of ZIF-8 (Zn) and MOF-5 (Zn) crystals ascribed to obstructed sulfur infiltration during material processing due to small pore apertures.<sup>313</sup> Thus, the comprehensive understanding of the influence of the size of MOF pore windows remains unclear at this time. Concerning the particle size of MOF host materials, an optimum size of 200 nm was found for ZIF-8 balancing capacity and cycling stability (Fig. 13).<sup>320</sup> Opposing size dependencies are observed for these properties, as a high capacity depends on high sulfur utilization during the conversion reactions while high cycle life requires moderate crystal sizes to diminish the significance of leaching of sulfur species at the external crystal surface. Morphological and also structural properties may also play a significant role regarding the potential sulfur loading.

As elucidated when describing the mechanism of conversion in MOF-based sulfur cathodes, interfacial processes at the conductive component profoundly affect the rate capability and the battery capacity. For instances, Mao *et al.* fabricated self-standing, binder-free cathodes by introducing sulfur into MOF crystals synthesized by chemical conversion of metal hydroxide entities at a 3D conductive network of CNTs.<sup>313</sup> Employing HKUST-1 (Cu), with a sulfur loading of 1  $\text{mg cm}^{-2}$ , an initial capacity of 1263  $\text{mA h g}^{-1}$  at 0.2C is achieved with a fading rate

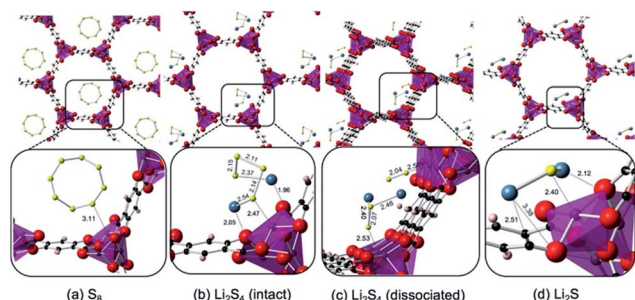


Fig. 12 Lowest energy structures for adsorbed (a)  $\text{S}_8$ , (b) intact and (c) dissociated  $\text{Li}_2\text{S}_4$ , and (d)  $\text{Li}_2\text{S}$  in MOF-74 (Ni) investigated by DFT calculations. Purple, red and black spheres represent Ni, O, and C atoms in the MOF, and blue and yellow represent Li and S.<sup>323</sup> (a–d) Reproduced with permission from ref. 323. Copyright 2017, American Chemical Society.



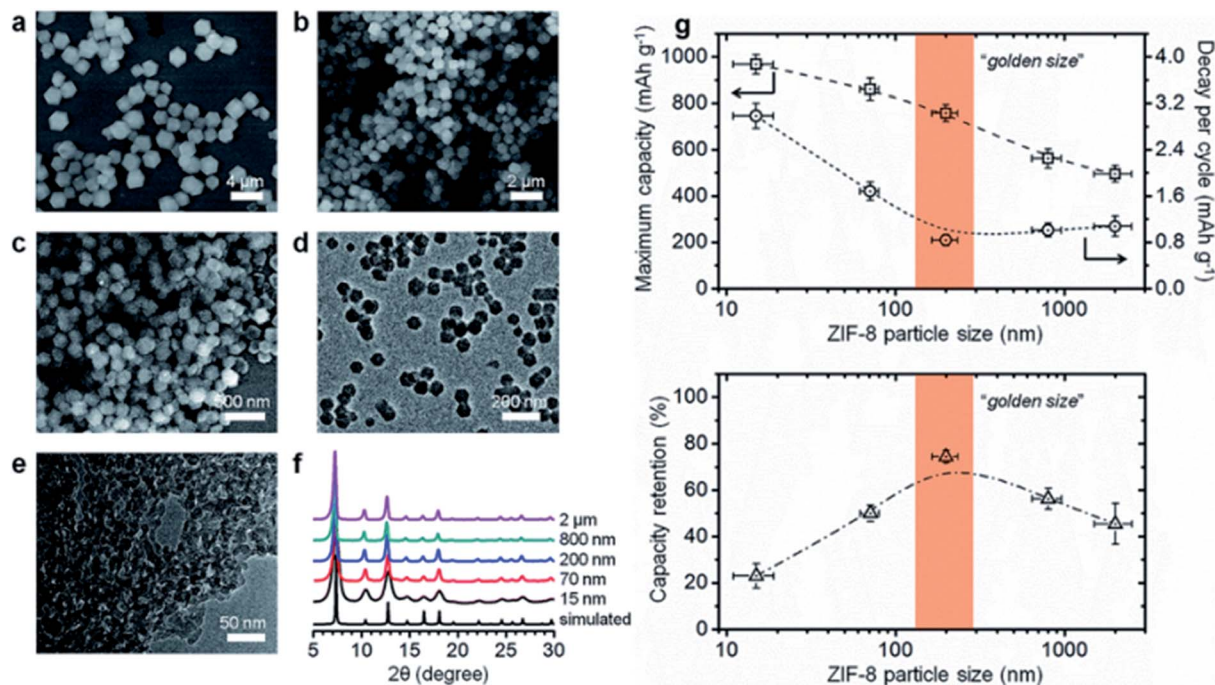


Fig. 13 ZIF-8 (Zn) samples with different crystal sizes displaying (a–e) SEM images, (f) XRD patterns and (g) statistical results of the performance as a sulfur host material in Li–S batteries at 0.5C.<sup>320</sup> Reproduced with permission from ref. 320. Copyright 2015, The Royal Society of Chemistry.

of 0.08% per cycle over 500 cycles and excellent recovery to 1102 mA h g<sup>−1</sup> after applying current rates up to 10C. For increased electrode thickness leading to a sulfur amount of 11.33 mg cm<sup>−2</sup> (68 wt%), the areal capacity equals 7.45 mA h cm<sup>−2</sup> corresponding to a gravimetric capacity of 658 mA h g<sup>−1</sup>. As also observed for a ZIF-8(Zn)/MWCNT electrode,<sup>316</sup> the conjunction provided between the MOF crystals and interpenetrating CNTs is a key feature of this kind of composite allowing for high battery performance due to proper adhesion and a large number of connection points.

Another successful strategy to increase the area for interfacial charge transfer is to wrap MOF particles with conductive materials.<sup>305,315,318,324,332–334</sup> At the same time, this approach may further hinder the leaching of LiPSs and thus improve the cycling stability.<sup>324,332</sup> Zhao *et al.* wrapped MIL-101 (Cr) crystals with graphene sheets achieving higher discharge capacity with smaller polarization.<sup>332</sup> For MIL-100 (V)/rGO nanosheets, the main advantage of the composite compared to MIL-100 (V) is the rate performance.<sup>318</sup> By wrapping Na<sub>2</sub>Fe[Fe(CN)<sub>6</sub>] crystals with the conducting polymer PEDOT, the initial capacity at 0.1C increased from 1020 mA h g<sup>−1</sup> to 1291 mA h g<sup>−1</sup> with a degradation rate of 0.15% per cycle over 100 cycles for high sulfur loadings of 64–66 wt% in the electrode.<sup>324</sup> As investigated by EIS, the PEDOT coating reduces the charge transfer resistance, thus enabling high sulfur utilization even at high sulfur loading.

In conclusion, many MOFs and comparable coordination compounds exhibit exceptional ability to demobilize LiPSs because of high porosity in combination with small pore/window sizes as well as the Lewis acid function of open metal

sites and the Lewis base function of organic linker molecules. Thus, MOF materials applied in Li–S batteries can greatly enhance their cycle life and enable the further reduction of formed LiPS species during the discharge. Due to the low conductivity or rather the non-conductive nature of MOFs, the development of MOF/conductive network composite structures and the improvement of the interfacial processes between these two components are crucial to boost the cell capacity, especially at high sulfur loading, and rate capability. The combination of discussed approaches may represent a promising starting point for further progress in the field, respectively applying tailored MOFs with suitable linker and unsaturated metal center chemistry, wrapping MOF particles with conductive sheet materials and growing MOFs on conductive matrix materials—perhaps even beyond carbon. The suitability of certain MOFs to be used for sulfur electrodes is further related to the chemical and electrochemical stability of the respective MOF compound. Recently, a comprehensive study on MOF-5 as a sulfur host material revealed that a large decrease of the capacity during the first cycles is caused by an initial electrochemical process which irreversibly oxidizes part of the active sulfur *via* its reaction with carbonate groups to form passive sulfate species.<sup>317</sup> Similar large initial capacity decays and XPS signals corresponding to a sulfate-like environment were also reported for other MOFs based on carboxylate linkers.<sup>304,305,307</sup> In addition to performance enhancement, a decisive role for the potential commercial application of MOFs in Li–S batteries is expected for the development of cost-effective and scalable methods to produce MOF materials tightly adhering to conductive components, *e.g.*





electrodeposition<sup>335</sup> and *in situ* synthesis on metal oxide support surfaces under hydrothermal conditions.<sup>336</sup>

## 6. Metals

This section examines metallic components influencing the electrochemical performance of Li-S batteries. Metals as chemical elements, alloys or metallic allotropes of non-metals or metalloids are characterized by typical physical properties, such as high electrical and thermal conductivity, corresponding to a certain type of chemical bonding. Accordingly, metallic bonding is based on electrostatic forces between metal cations forming a metal lattice and delocalized electrons forming an electron cloud or, in a more detailed way, by the band model considering orbitals. Regarding their chemical properties, metals are able to form *e.g.* sulfidic metal compounds based on covalent bonds or coordination compounds like MOFs, which are already discussed in Section 5. Thus, the issue of the electrochemical stability of metals is important not only in regard of electrode stability, but also in regard of the possible formation of metal compounds due to side reactions during battery operation. For instance, metal sulfides on the surface of metal components may influence cycling stability, electrocatalytic activity and capacity contributions from corresponding side reactions.

The advantageous effects of metals on the performance of Li-S batteries are discussed to rely mainly on the electrocatalysis of the LiPS conversion as well as on the adsorption and confinement of LiPS.<sup>337–352</sup> Furthermore, the influence on the

morphology of insoluble Li<sub>2</sub>S deposits may play an important role in cathode stability.<sup>347,348,353</sup> Several studies on metal/carbon composite sulfur electrodes also address the significance of interactions of the carbon matrix with metallic parts *e.g.* in metal nanoparticle/graphene host materials.<sup>341,354,355</sup> Remarkably, Li-S batteries employing nickel with a high sulfur loading corresponding to 40 mg cm<sup>-2</sup> achieved a reversible capacity of about 670 mA h g<sup>-1</sup> after 100 cycles at 0.2C.<sup>356</sup> The positive electrode of the battery consists of a catalytic carbon-coated Ni foam current collector and a Li<sub>2</sub>S<sub>6</sub>-catholyte. Hence, the active material is initially present in the form of diluted LiPS subsequently taking part in the conversion reaction. Further concepts to apply metal components in sulfur electrodes comprise metal/carbon composite host materials and separator coatings, and metal additives along with metal in the form of electrode decoration or dopants. As summarized by Table 6, research activities include mainly nickel and cobalt-based materials as well as noble metals like platinum and metallic main group elements. Accordingly, in this section, the role of metal current collectors is described followed by metal components based on nickel, cobalt and further metals or metal alloys.

### 6.1 The role of metal current collectors in the positive electrode

In 2014, a detailed analysis of the literature on Li-S batteries revealed that only 6% of the publications deal with the issues of binder, separator or current collector materials while the vast majority of articles (64%) discuss thin film sulfur electrodes.<sup>364</sup> However, as summarized in this section, there is a huge

Table 6 Summary of selected studies researching metal components to enhance Li-S batteries

Way of metal employment	Initial capacity [mA h g <sup>-1</sup> ]	Reversible capacity [mA h g <sup>-1</sup> ]	Current rate <sup>a</sup>	Cycle number	Degradation rate per cycle [%]	Sulfur content <sup>b</sup> [wt%]	Sulfur loading [mg cm <sup>-2</sup> ]	Ref.
Ni foam current collector, Li <sub>2</sub> S <sub>8</sub> catholyte	≈ 1080 <sup>c</sup>	≈ 870 <sup>c</sup>	0.1C	50	≈ 0.39 <sup>c</sup>	N/A	0.152	337
C-coated Ni foam current collector, Li <sub>2</sub> S <sub>6</sub> catholyte	1024	669	0.2C	100	0.35	60 <sup>d</sup>	40	356
S-NP <sup>e</sup> on Ni foam current collector	≈ 990 <sup>c</sup>	775	0.5C	200	≈ 0.1 <sup>c</sup>	N/A	0.84	357
S/Ni composite as active material	1469	758	0.5C	200	0.24	29	0.8–1.1	358
NiS <sub>x</sub> -alloy-coated S/Ni on Ni foam current collector	1029	800	0.167C	100	0.22	N/A	3.68	359
Ni-NP/graphene/N-doped CNT <sup>f</sup> Li <sub>2</sub> S <sub>6</sub> catholyte	1150	908	0.5C	100	0.21	50	0.81	340
Ni-NP/graphene host material	1092	832	0.2C	500	0.05	49	1.0–1.5	354
Co-N-doped graphitic C host material	1137	930	0.2C	300	0.06	29	1.4	341
Cellular Co-NP/N-doped C host material	685	514	2C	850	0.03	94	3.6	345
Co/N-doped C nanofiber/rGO <sup>g</sup> separator coating	865	616	0.5C	500	0.05	78	1.0–1.2	350
Pt-NP/C host material	1158	575	0.5C	200	0.25	39	1.0	348
Pd <sub>3</sub> Co-NP cathode additive	648	544	1C	200	0.08	60	1.13	360
Ir/C separator coating	1508	689	0.2C	100	0.54	60	0.8	349
Fe-NP/graphitic C host material	980	500	0.8C <sup>h</sup>	450	0.11	56	1.2	361
Cu-NP/C host material	1050	630	0.06C	500	0.08	40	1.0	362
Au-NP/C host material	1107	771	0.1C	100	0.30	54	1.3	353
Ti-particle film on the cathode	1255	722	0.5C	100	0.42	56	N/A	363
Al-particle film on the cathode	1257	977	0.5C	100	0.22	56	N/A	363
Te-doped S	≈ 780 <sup>c</sup>	673	3C <sup>h</sup>	400	0.03	58	1.0–1.2	355

<sup>a</sup> 1C = 1674 mA g<sup>-1</sup>. <sup>b</sup> Mass percentage of sulfur on the whole cathode excluding the Al or Ni substrate. <sup>c</sup> The capacity/degradation rate is estimated from the figure since authors did not provide the specific number in the paper. <sup>d</sup> Mass percentage of sulfur on the cathode including the nickel foam current collector with a carbon shell. <sup>e</sup> NP = nanoparticle. <sup>f</sup> CNT = carbon nanotube. <sup>g</sup> rGO = reduced graphene oxide. <sup>h</sup> To activate the electrode, a lower C-rate was applied for a few initial cycles.



capability to increase the performance and the sulfur loading of Li-S batteries by using advanced metal current collectors for the positive electrodes.

Comparing different current collector materials (nickel foam, carbon foam, non-woven carbon, and vertically aligned carbon nanotubes), Barchasz *et al.* observed a significantly increased discharge capacity and cycle life for nickel foam and attributed the effect to the high specific surface area and the stable morphology of the current collector.<sup>365</sup> Following studies on nickel foam current collectors<sup>366</sup> and interlayers<sup>367</sup> also discussed the accommodation of active material and the corresponding internal electron transport network as well as the trapping of LiPS as reasons for the improvement. Similarly, the high relevance of the current collector morphology was demonstrated by Cheng *et al.* who realized increased sulfur loadings and improved sulfur utilization by using 3D aluminum foam/carbon nanotube scaffolds.<sup>368</sup> The sulfur composite achieved an initial discharge capacity of 860 mA h g<sup>-1</sup> with a sulfur loading of 7.0 mg cm<sup>-2</sup> at 0.1C, while the commonly sulfur-flat aluminum foil cathode yields only 534 mA h g<sup>-1</sup> for a mass loading of 4.61 mg cm<sup>-2</sup>. As a further current collector providing for an electron transport micro-network, interwoven stainless steel was investigated.<sup>369</sup> Introducing only sulfur with no additional carbon additive or host material, the corresponding Li-S batteries showed a reversible capacity of 420 mA h g<sup>-1</sup> after 250 cycles at 0.1C.

Regarding the metal used as a current collector material, Raguzin *et al.* found aluminum and platinum foils to be inert towards the electrochemical reactions in Li-S batteries with sulfur/carbon black cathode materials obtained by melt diffusion.<sup>370</sup> However, in the voltage range of 1.0–3.0 V, nickel foil is electrochemically active ( $\text{Ni}^{(0)} \rightarrow \text{Ni}_3^{(I/II)}\text{S}_2 \rightarrow \text{Ni}^{(III)}\text{S}$ ) and contributes to the measured capacity resulting in etching and therefore a lower cycling stability and a voltage drop for nickel current collectors. Consequently, after 30 cycles, the assembled cell predominantly behaves as a  $\text{Ni}_3\text{S}_2/\text{Li}$  battery supplying a voltage of 1.4 V. Earlier studies on nickel foam current collectors also indicated the involvement of Ni in the electrochemical conversion reaction observing  $\text{NiS}$  on the foam surface after several cycles when discharged below 1.5 V.<sup>371,372</sup> The effect of side reactions with nickel can be minimized by adding Si or  $\text{SiO}_2$  as dopants or narrowing the cut off voltage.<sup>370</sup> Zhao *et al.* potentiostatically electrodeposited sulfur nanodots from a 0.1 M  $\text{Na}_2\text{S}$  aqueous solution on a nickel foam and then applied the obtained composite as a positive electrode in Li-S batteries.<sup>357</sup> Such devices achieved a reversible capacity of 775 mA h g<sup>-1</sup> after 200 cycles at 0.5C in the smaller voltage range of 1.7–2.6 V for a comparably low sulfur loading of 0.84 mg cm<sup>-2</sup>.

A further important aspect of the role of metallic nickel in Li-S batteries was indicated by Hassoun *et al.* in 2012, when they reported enhanced electrode kinetics for thin nickel coatings on sulfur/carbon electrodes.<sup>373</sup> Later on, Babu *et al.* provided a comprehensive study on the electrocatalytic activity of metals to enhance the reaction kinetics of LiPS conversion.<sup>337</sup> For this purpose, 50 to 200 nm thick metal films of aluminum, gold, Ni or platinum were coated on stainless steel or aluminum foils by electron beam evaporation and employed as positive electrodes

in  $\text{Li}_2\text{S}_8$ -catholyte-based Li-S batteries. Such a battery design consists of a Li- or Li<sup>+</sup>-containing negative electrode and an electronically conductive positive metal electrode and comprises sulfur in the form of dissolved LiPS in the electrolyte. Thus, the positive electrode is made up of a bare current collector and the catholyte with an active S-containing redox species. While Al-coated foils were found to be inactive for LiPS conversion, Pt- and Ni-coated electrodes showed electrocatalytic properties with increasing peak currents and stable peak positions in cyclic voltammograms for increasing scan rates, as well as reduced peak separation. In the voltage range from 1.5 V to 3.0 V, the best performance was obtained for a macroporous 3D nickel foam current collector achieving a reversible capacity of  $\approx 900 \text{ mA h g}^{-1}$  after 50 cycles at 0.1C with a  $\text{Li}_2\text{S}_8$  concentration of 0.06 mol L<sup>-1</sup> corresponding to a sulfur loading of 0.152 mg cm<sup>-2</sup>.<sup>337</sup> Following studies on nickel foam current collector/LiPS catholyte electrodes demonstrated that the sulfur loading can be tremendously increased for such electrodes.<sup>356,374</sup> By incorporating nickel foam into a carbon shell of interwoven CNTs entangled with a carbon nanofiber network, a 6 M  $\text{Li}_2\text{S}_6$  catholyte corresponding to a sulfur mass loading of  $\approx 40 \text{ mg cm}^{-2}$  could be used to achieve an initial capacity of 1024 mA h g<sup>-1</sup> (41 mA h cm<sup>-2</sup>) and a reversible capacity of 669 mA h g<sup>-1</sup> (27 mA h cm<sup>-2</sup>) after 100 cycles at 0.2C in the voltage range of 1.7–2.8 V.<sup>356</sup>

In summary, metallic current collector materials for positive electrodes in Li-S batteries can enhance the performance and enable high sulfur loading mainly due to improved electron transport resulting from a suitable 3D morphology of highly conductive metals and electrocatalytic activity of certain metals, *e.g.* nickel, in LiPS conversion reactions. Possible side reactions with the metal may require to reduce the voltage range to achieve stable electrochemical characteristics over long cycle times. The possibly limited voltage range and larger mass of some metals have to be considered for the design of commercial Li-S batteries as they may cause a significant decrease in the energy density of the devices.

## 6.2 Metals as additives and metal/porous carbon hybrid scaffolds

**6.2.1 Nickel.** As described above, the electrocatalytic properties of metallic nickel towards the electrochemical conversion of LiPSs can be utilized by using a Li-S battery design, in which sulfur is included in the form of a LiPS-catholyte reacting at a nickel electrode, more specifically at a nickel current collector.<sup>337,356,365</sup> Besides, a thin nickel coating of a suitable thickness of 50 nm introduced by electron beam physical vapor deposition on a sulfur/carbon electrode was observed to improve electrode kinetics and electronic conductivity.<sup>373</sup> Sörgel *et al.* combined the approaches of using a nickel foam current collector and a further outer  $\text{NiS}_x$  alloy coating by co-electroplating polythiophene functionalized sulfur particles on nickel foam and subsequently electrodepositing an additional 50 nm Ni-alloy layer.<sup>359</sup> Nickel was also used as the metallic binder and hence electrochemically reduced from an inorganic nickel salt during the co-deposition process. The resulting S/Ni composite film consists of an outer nickel layer and an inner layer



containing nickel and sulfur while a 440 nm thick  $\text{NiS}_x$  alloy conversion layer is present between the Ni binding matrix and polythiophene-functionalized sulfur particles. The detected species of  $\text{NiS}$  and  $\text{Ni}_3\text{S}_2$  indicate the partial reduction of sulfur during the electroplating process. The prepared electrodes require a conditioning time of about 20 cycles and achieve a reversible capacity of  $800 \text{ mA h g}^{-1}$  after 100 cycles at  $0.167\text{C}$  with a sulfur loading of  $3.7 \text{ mg cm}^{-2}$ . The performance significantly depends on the additional  $\text{NiS}_x$  alloy layer electrodeposited after electroplating the S/Ni composite as this step seems to transform a large portion of elemental sulfur of the composite into nickel sulfides.

Former studies on S/Ni composites, in which the electrodes were prepared from binder- and conductive carbon-containing slurries, also showed that interactions of nickel and sulfur lead to the formation of sulfide species like  $\text{Ni}_2\text{S}_3$ .<sup>338,358</sup> Moreover, the presence of Ni fibers (3 wt%) changed the morphology of sulfur from smooth to rough agglomerated particles.<sup>338</sup> Zhu *et al.* obtained a reversible capacity of  $758 \text{ mA h g}^{-1}$  at  $0.5\text{C}$  after 200 cycles with a sulfur/RANEY® nickel alloy (incl.  $\text{Ni}_x\text{Al}_y\text{O}_z$ ) composite in the voltage range of 1.7–2.8 V, observing also better rate capability and subsequent capacity recovery as well as higher sulfur loading compared to a sulfur/carbon composite electrode.<sup>358</sup>

The electrocatalytic properties of metallic nickel have also been exploited by using Ni-decorated carbon materials as sulfur hosts in composites obtained by melt-diffusion.<sup>354,375</sup> The capacity achieved employing MWCNTs with 27 wt% of Ni is higher than that achieved for MWCNTs without nickel decoration, especially if the current rate is increased.<sup>375</sup> After 200 cycles at  $0.5\text{C}$  a capacity of  $545 \text{ mA h g}^{-1}$  remained for a sulfur loading of  $1.0 \text{ mg cm}^{-2}$ . It should be noted that metal residues and impurities caused by the synthesis of certain carbon materials, *e.g.* CNTs and MOF-derived carbons,<sup>376</sup> may account for a considerable part of the performance enhancement of the carbon materials by affecting electrode kinetics.

Moreover, for metal/carbon composites, the carbon matrix may have a significant influence on the interactions between the metallic component and LiPSs. According to DFT calculations published by Yao *et al.*,<sup>354</sup> the adsorption of sulfur clusters on nickel/graphene is stronger compared to a nickel slab surface while the adsorption on copper/graphene is weaker than that on copper, and the adsorption on tin/graphene is comparable to that on tin.<sup>354</sup>

As seen in Fig. 14, the graphene substrate can change the metal's valence band center by influencing the electron density distribution, thus tuning the metal–S interaction. While significantly affecting a transition metal with localized d states, the effect may be rather insignificant for a main group metal with extended p states. If defects are present in the graphene substrate, the metal–S interaction is more similar to that in a free-standing metal slab. Also, for such metal surfaces, the adsorption strength on Ni is higher than that on Cu or Sn. Smaller sulfur clusters show lower adsorption energies on all considered surfaces meaning that sulfur tends to form dispersive smaller clusters on metal surfaces rather than gathering into larger clusters. Experimentally, nickel nanoparticle

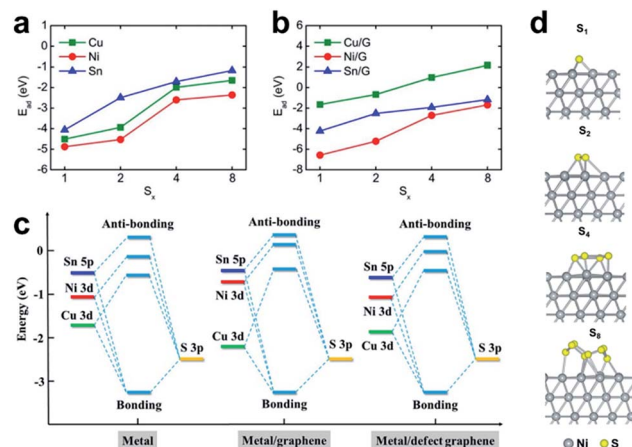


Fig. 14 Calculated adsorption energies of sulfur clusters  $\text{S}_x$  ( $x = 1, 2, 4$ , and  $8$ ) on the surfaces of (a) metals and (b) metal/graphene systems, (c) energy level interactions between metal surfaces and sulfur clusters (blue, red and green bars denote the d-band or p-band centers of the Ni d band, Cu d band, and Sn p band; yellow bars denote the p orbitals of sulfur clusters) and (d) the stable configurations of sulfur clusters adsorbed on a nickel surface.<sup>354</sup> (a–d) Reproduced with permission from ref. 354. Copyright 2018, American Chemical Society.

(10 at%)/graphene employed as a sulfur host material achieved an initial capacity of  $1092 \text{ mA h g}^{-1}$  degrading at a rate of only 0.05% per cycle to a reversible capacity of  $832 \text{ mA h g}^{-1}$  after 500 cycles at  $0.2\text{C}$  for a sulfur loading of  $1.0\text{--}1.5 \text{ mg cm}^{-2}$ . As predicted by the DFT calculations, the capacities and rate capabilities are advantageous for Ni/graphene compared to Sn and Cu, with all three metal/graphene composites showing better capacity retention than bare graphene. Nickel nanoparticle/graphene composites were also used for positive Li–S battery electrodes containing sulfur in the form of a LiPS-catholyte.<sup>339,340,377</sup> Mosavati *et al.* found higher discharging capacities for smaller nickel particles of 20 nm compared to 40 nm or 100 nm.<sup>377</sup> After the 40<sup>th</sup> cycle, a passivation layer was observed on the particle surface, which appears to be thinner for nickel particle sizes of 40 nm and 100 nm and may consist of  $\text{Li}_2\text{S}$  and  $\text{NiS}_x$ .

In summary, the performance enhancement obtained with metallic nickel components may be related to the electrocatalytic properties of Ni towards the liquid–solid conversion of LiPSs, improved electrical conductivity, and trapping of LiPSs due to chemical adsorption and porous morphologies. Accordingly, several research studies observed decreased charge transfer resistances for Ni-containing materials in EIS studies,<sup>338,339,358,359,375</sup> reduced polarization of Li–S batteries,<sup>339</sup> and the decoloring of an LiPS solution due to an added Ni/carbon composite.<sup>340</sup> Furthermore, we discussed several findings indicating the formation of nickel sulfides or alloys as an important aspect of the underlying mechanism of the improved nickel-based sulfur electrodes.

**6.2.2 Cobalt.** So far, cobalt-based nanostructured materials for Li–S batteries have comprised several Co/carbon composites obtained by thermolysis processes and have been used as either a sulfur host material<sup>341–346,351,352,378–381</sup> or an interlayer between the cathode and the separator.<sup>350,382,383</sup> Remarkably, for Co-





containing Li-S batteries, degradation rates lower than 0.1% per cycle were achieved. The discussion about the material properties enabling this great performance mainly focuses on the synergistic effects of cobalt and heteroatoms of the carbon matrices.

The majority of the materials is derived from the zeolitic imidazolate framework  $[\text{Co}(\text{MeIm})_2]_n$  (MeIm = 2-methylimidazole),<sup>341–343,345,346,351,383</sup> known as ZIF-67 (Co), a MOF with an open tetrahedral structure and a pore diameter of 11.6 Å.<sup>384</sup> The carbonization of chemically precipitated ZIF-67 (Co) is performed with temperatures of 500–900 °C either under an inert atmosphere ( $\text{N}_2$  or Ar)<sup>341,342,345,351,383</sup> or under reductive conditions ( $\text{H}_2/\text{Ar}$  mixture)<sup>343,346</sup> yielding composites of metallic cobalt nanoparticles and N-doped carbon matrices. After this pyrolysis step, the obtained composites show BET surface areas of around 200–300  $\text{m}^2 \text{g}^{-1}$ ,<sup>342,343,346,383</sup> pore volumes of around 0.3  $\text{cm}^3 \text{g}^{-1}$ ,<sup>343,346</sup> and a cobalt content of around 40 wt%,<sup>342,343,346</sup> which was further reduced by chemical etching in some of the studies.<sup>341,343,345,351,383</sup> He *et al.* reported etched uniform particles in a rhombic dodecahedral shape with sizes of around 350 nm which are made up of graphitic carbon co-doped with cobalt and nitrogen.<sup>341</sup> After liquid infiltration of  $\text{Li}_2\text{S}$  nanoparticles, a reversible capacity of 930  $\text{mA h g}^{-1}$  and a degradation rate of 0.06% per cycle were determined after 300 cycles at 0.2C for a sulfur loading of 1.4  $\text{mg cm}^{-2}$  and a sulfur content of 29 wt%. Li *et al.* achieved a capacity of 850  $\text{mA h g}^{-1}$  and a capacity loss of 0.21% per cycle after 200 cycles at also 0.2C for a sulfur loading of 1.0  $\text{mg cm}^{-2}$  and a sulfur content of 49 wt%.<sup>342</sup> In this study, the Co nanoparticles embedded in the N-doped carbon polyhedrons were not removed by etching and sulfur was introduced by melt diffusion. Wrapping etched ZIF-67(Co)-derived polyhedrons with rGO nanosheets yielded a host material delivering a capacity of 949  $\text{mA h g}^{-1}$  after 300 cycles at 0.18C corresponding to a degradation rate of 0.07% per cycle with 1.0  $\text{mg cm}^{-2}$  sulfur.<sup>343</sup> As extension to the combination with functional carbon materials, Liu *et al.* pyrolyzed and etched a bimetallic Co/Zn-ZIF assembled with GO sheets and poly(vinylpyrrolidone) (PVP) to synthesize N-doped porous carbon nanosheets with embedded cobalt nanoparticles (11 wt%) as

a host material for sulfur and lithium,<sup>341</sup> thus serving as both electrodes. With a specific surface area of 500  $\text{m}^2 \text{g}^{-1}$  and a pore volume of 1.0  $\text{cm}^3 \text{g}^{-1}$ , these materials in a Li-S battery showed reversible capacities of 633  $\text{mA h g}^{-1}$  and 619  $\text{mA h g}^{-1}$  after 200 cycles at 1C and 2C for a sulfur loading of 0.8–1.0  $\text{mg cm}^{-2}$ . The issue of quite low sulfur loadings was addressed by the direct formation of ZIF-67(Co) onto the surface of CoAl layered double hydroxide (LDH) *via in situ* nucleation and directed epitaxial growth followed by thermolysis and etching of this sacrificial template. The obtained Co-nanoparticle/N-doped carbon composite showed a cellular morphology with a hierarchical micro-mesoporous honeycomb-like architecture (see Fig. 15a) and a specific surface area of 460  $\text{m}^2 \text{g}^{-1}$ . For a sulfur loading of 3.6  $\text{mg cm}^{-2}$  and a high sulfur content of 94 wt%, this host material achieved 514  $\text{mA h g}^{-1}$  after 850 cycles at 2C corresponding to a degradation rate of only 0.03% per cycle. For a cathode with 7.5  $\text{mg cm}^{-2}$  of sulfur, still, a capacity of about 400  $\text{mA h g}^{-1}$  was achieved after 300 cycles at 1C, demonstrating high rate performance and cycling stability.<sup>345</sup> Wang *et al.* realized a capacity of 679  $\text{mA h g}^{-1}$  after 50 cycles at 0.5C for a sulfur loading of 5.2  $\text{mg cm}^{-2}$  by using a battery design with a 10  $\mu\text{m}$  ZIF-67(Co)-derived interlayer coated on the surface of the sulfur/carbon electrode.<sup>383</sup>

Besides ZIF-67(Co), other cobalt-containing precursors have been used to synthesize both sulfur host materials<sup>344,352,378</sup> and separator coatings.<sup>350</sup> Zhang *et al.* used a pyrolysis process to obtain a porous 3D-matrix consisting of graphene nanosheets and MWCNTs with Co-nanoparticles (36.5 wt%) wrapped on the top of the nanotubes or distributed randomly on the graphene sheets using GO, urea and  $\text{Co}(\text{NO}_3)_2$  salt as starting materials.<sup>378</sup> Li-S batteries employing this sulfur host material achieved an initial capacity of 1374  $\text{mA h g}^{-1}$ , which decreased to 837  $\text{mA h g}^{-1}$  over 200 cycles at 0.1C for a sulfur loading of 1.3–1.6  $\text{mg cm}^{-2}$ , and a reversible capacity of 336  $\text{mA h g}^{-1}$  for a sulfur loading of 4.7  $\text{mg cm}^{-2}$ .

The positive effect of the metallic cobalt components on the performance of Li-S batteries is mainly ascribed to the electrocatalytic properties of cobalt and enhanced LiPS adsorption.

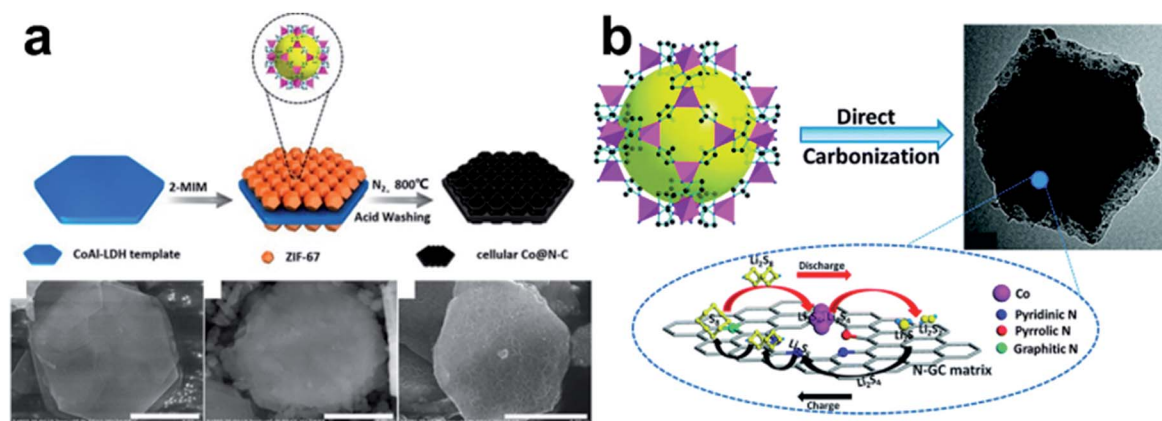


Fig. 15 (a) Schematic illustration and corresponding SEM images of the synthesis of cellular Co nanoparticle/N-doped carbon composites from CoAl-LDH templates and the ZIF-67 (Co) precursor,<sup>345</sup> and (b) schematic illustration and TEM image of a ZIF-67 (Co)-derived cobalt nanoparticle/N-doped carbon composite and its interaction with LiPSs during charging and discharging.<sup>342</sup> (a) Reproduced with permission from ref. 345. Copyright 2017, American Chemical Society. (b) Reproduced with permission from ref. 342. Copyright 2016, The Royal Society of Chemistry.



Most reported materials contain nitrogen as a doping heteroatom besides cobalt. Based on XPS measurements, several groups identified pyridinic, pyrrolic and graphitic nitrogen in carbon matrices and furthermore observed both metallic and divalent cobalt.<sup>342,350,378,383</sup> The thereby indicated interactions of Co, N and C atoms may strengthen the adsorption ability of the composites towards LiPSs and promote the conversion reaction as shown in Fig. 15b. According to DFT calculations, the adsorption energy for LiPSs follows the order C–Co–N > C–Co > C–N > C implying that C–Co–N serves as a conductive Lewis base matrix.<sup>341</sup> The incorporation of N atoms and Co nanoparticles modulates the electron density of a carbon surface through a displacement of charge from Co atoms to other atoms nearby.<sup>344</sup> The increased electron density of graphitic N atoms leads to the formation of bonds with Li atoms.<sup>351</sup> In line with these findings, the color of Li<sub>2</sub>S<sub>4</sub> or Li<sub>2</sub>S<sub>6</sub> solutions faded when adding the Co/N-doped carbon composite materials.<sup>346,350,352,378</sup> For a Co/N-doped carbon host material, Zhong *et al.* reported a degenerating rate performance of the corresponding Li–S batteries, if the Co/N ratio was higher or lower than 1 : 7.2.<sup>352</sup> Furthermore, possible O-functional groups<sup>343,346,350,352,378</sup> and cobalt sulfide layers<sup>343,346</sup> may also affect the adsorption of LiPSs. Regarding the electrocatalytic properties of cobalt components, lower overpotentials<sup>343,352,383</sup> and charge transfer resistances<sup>343,346,350,378</sup> for the conversion reactions as well as smaller peak separation in cyclic voltammograms<sup>352,383</sup> were observed for carbon materials with Co compared to similar materials without Co. It should be noted that the presence of cobalt during the thermolysis synthesis also affects the structure of the carbon component as it catalyzes graphitization. Therefore, the absence of cobalt components may not be the only difference in the resulting battery materials.

The performance achieved with cobalt composite materials can be further enhanced by using conductive scaffold materials like graphene and CNTs, which also additionally lowers the charge transfer resistance determined for the conversion reactions.<sup>343,344,351,379</sup> The synergistic effects of N-doped carbon matrices and metallic cobalt nanoparticles or doping atoms as well as enhanced charge transport enable exceptionally low capacity fading over many cycles due to LiPS-adsorption and electrocatalytic properties. By thermolysis of suitable precursors like ZIF-67 (Co) and sometimes chemical etching, Co/N-doped carbon composites in the form of polyhedrons, nanorods, nanofibers and nanosheets were obtained and used as a sulfur host material or separator coating. For a possible commercial application of such materials, increasing the sulfur loading seems to be a crucial next step.

**6.2.3 Other metals and metal alloys.** As Table 6 reveals, among the investigated metals (Al, Au, Cu, Fe, Ir, Ni, Co, Pd<sub>3</sub>Co, Pt, Ti, Te, and Se) for Li–S batteries, nickel and cobalt seem to be the most promising candidates. However, for example considering nickel in comparison to platinum, Babu *et al.*<sup>337</sup> found nickel to cause a greater performance enhancement while other researchers achieved higher capacities and stability with platinum.<sup>339,385</sup> Thus, the specific battery and material design may have a crucial impact on the specific influence of a certain metal and does not just depend on its chemical identity. When

comparing metals, attention should be also paid to their mass and the amount needed in the electrodes as well as to the processability and synthesis methods to obtain the functional nanostructured metal-based battery material. The metals discussed in this section are employed as a powder additive,<sup>347,360</sup> metal-nanoparticle/carbon composite host and metal-decorated host or interlayer material,<sup>348,349,353,361–363,386,387</sup> as well as metal-nanoparticle/sulfur composite<sup>385</sup> and metal-doped sulfur.<sup>355,388</sup>

Tao *et al.* used a wet chemical method to decorate sulfur with porous Pt structures which prevent sulfur microparticles from agglomeration and grain growth during long-term aging.<sup>385</sup> Due to the high morphological integrity and enhanced electrochemical reaction kinetics attributed to good electrical conductivity, a reversible capacity of 680 mA h g<sup>−1</sup> was obtained after 80 cycles at 0.1C. Furthermore, the Pt-decorated sulfur has a higher tap density than pristine sulfur enabling a higher volumetric capacity. The role of Pt in the mechanism of the sulfur electrode in Li–S batteries was investigated more in detail by Thangavel *et al.* using a Pt/conductive carbon positive electrode containing 80 wt% of platinum powder and a 2 mM Li<sub>2</sub>S<sub>8</sub>-catholyte.<sup>347</sup> The decreased overpotential and peak separation for the sulfur/sulfide conversion in cyclic voltammetry and reduced charge transfer resistance were attributed to the electrocatalytic function of platinum. Assumingly, the oxidation of the platinum surface encourages stronger interactions with LiPSs and involves Pt–S sulfidic bond formation. Potentiostatic chronocoulometric measurements accompanied by UV-Vis characterization show that the surface coverage on platinum is higher than that on carbon. Moreover, the Pt-catalyst leads to instantaneous nucleation and 3D growth, while progressive nucleation on carbon restricts to 2D growth of solid Li<sub>2</sub>S<sub>2</sub>/Li<sub>2</sub>S species as concluded from cyclic voltammograms and Avrami theory. Lin *et al.* obtained Li–S batteries with a reversible capacity of 503 mA h g<sup>−1</sup> after 200 cycles at 0.5C using a commercial platinum nanoparticle/carbon composite as a sulfur host with a rather low platinum content of 1 wt%.<sup>348</sup> XPS measurements proved chemisorptive interactions of platinum and LiPSs, while EIS investigations suggest that platinum promotes a more favorable deposition of Li<sub>2</sub>S<sub>2</sub> and Li<sub>2</sub>S as the charge transfer resistance in the mid-frequency region commonly assigned to the properties of the polymeric-like SEI is decreased.

Performance enhancement accompanied by electrochemical data indicating the improvement of the electrode kinetics was also achieved with further group 8–10 transition metals, such as the Pd<sub>3</sub>Co alloy (15 wt% nanoparticle additive),<sup>360</sup> iridium (10 wt% or 25 wt% nanoparticles on Ketjen black as a host or separator coating),<sup>349</sup> and iron (nanoparticles embedded in N-doped CNFs mixed with graphene as a separator coating<sup>387</sup> and Fe/Fe<sub>3</sub>C nanoparticles with a graphene shell on a cotton textile as a host).<sup>389</sup> Zhang *et al.* sputtered aluminum or titanium on the surfaces of sulfur/carbon electrodes to realize an improvement due to enhanced electrical conductivity, filled interspaces and related confinement as well as improved electrode kinetics.<sup>363</sup> As seen in Table 6, aluminium provided for better results than titanium, which might also be related to the higher amount of deposited aluminium. Magnetron sputtered



aluminium was also used to decorate functional carbon interlayers between the sulfur electrode and the separator.<sup>386</sup> 3 wt% of gold nanoparticles was decorated onto a sulfur/carbon electrode by a wet chemical method resulting in a capacity of 771 mA h g<sup>-1</sup> after 100 cycles at 0.1C.<sup>353</sup> Considering DFT calculations and XPS measurements, the improved electrochemical performance and kinetics are attributed to the controlled deposition of LiPSs by mediation of gold nanoparticles which suppress the formation of thick aggregates of thus less active materials.<sup>353</sup> For a carbon host decorated with 10 wt% of copper nanoparticles, the structural and binding energy data suggest the formation of copper sulfidic compounds as the underlying mechanism for the improvement of the corresponding Li-S batteries.<sup>362</sup>

In addition to metal additives and metal composite materials, another approach is to alter the electrochemical properties of sulfur by doping. Metallic tellurium powder was heated with sulfur in a sealed tube to establish 1–5 wt% Te-content changing the binding energy of sulfur and tellurium, shifting the TGA curve to higher temperatures but without affecting the XRD pattern and binding energy related to Te-Te bonds. The highly uniform doping is assumed to improve the electrical conductivity and redistribute the electron density of the sulfur sites to facilitate the lithiation/delithiation process, which was also demonstrated by first principles calculations. Te-doped sulfur/carbon electrodes provided a capacity of 673 mA h g<sup>-1</sup> after 400 cycles at 3C corresponding to a degradation rate of 0.026% per cycle for a sulfur loading of 1.0–1.2 mg cm<sup>-2</sup>.<sup>355</sup> Selenium also seems suitable as a doping element as a sulfur-rich S<sub>1-x</sub>Se<sub>x</sub>/carbon composite ( $x \leq 10$ ) delivered a capacity of 1090 mA h g<sup>-1</sup> after 200 cycles at 0.12C.<sup>388</sup>

In conclusion, several metals and alloys are suitable to catalyze the electrochemical conversion of sulfur or LiPSs to Li<sub>2</sub>S. The proper adsorption of LiPS intermediates on the surface of many metals constitutes an initial step of the electrocatalytic process and lessens the shuttle effect. For certain metals, the formation of metal compounds such as sulfides during charge and discharge may also significantly influence the surface electrochemistry of the metal-containing battery materials. There are several Li-S battery design concepts to involve metals as well as many synthetic approaches to obtain nanostructured metallic components and metal/carbon composites, making these materials very promising for high-performance electrodes in Li-S batteries.

## 7. Metal hydroxides

Nanostructured metal hydroxides with hydrophilic groups and a functional polar surface have been recently investigated as promising cathode host materials for Li-S batteries, such as Co(OH)<sub>2</sub> nanosheets,<sup>390</sup> Ni(OH)<sub>2</sub> nanoparticles,<sup>125,391,392</sup> Ni(OH)<sub>2</sub> hollow spheres,<sup>393</sup> Ni<sub>3</sub>(NO<sub>3</sub>)<sub>2</sub>(OH)<sub>4</sub> shells,<sup>394</sup> layered double hydroxides,<sup>395,396</sup> and so on. In 2015, Nie *et al.* reported Co(OH)<sub>2</sub> nanosheets as a conceptually new metal-containing nanostructured material to obstruct the LiPS shuttling and prolong the service life of Li-S cells.<sup>390</sup> The positive electrode consists of a sulfur/conductive carbon black (S/CB) composite uniformly

coated with Co(OH)<sub>2</sub> nanosheets (S/CB@Co(OH)<sub>2</sub>). This novel S/CB@Co(OH)<sub>2</sub> cathode with a protective Co(OH)<sub>2</sub> layer provided higher capacities and better capacity retention, especially at high current rates, compared with a S/CB cathode without a Co(OH)<sub>2</sub> coating used as a control cell (capacity retentions of, respectively, 71.2% and 20.2% after 200 cycles at 1C). The improved cell performance was attributed to the metal hydroxide coating which inhibits the shuttle diffusion of LiPS species by the effective entrapment/reutilization of the active material. Nie *et al.* also described a similar cathode concept but in this case the S/CCB composite surface was covered with Ni(OH)<sub>2</sub> nanoparticles (1–2 nm) instead of Co(OH)<sub>2</sub> nanosheets.<sup>391</sup> After 200 cycles at 1C, the prepared S/CB@Ni(OH)<sub>2</sub> cathode showed a capacity retention of around 70%, with the initial and ending capacities of, respectively, 810 and 590 mA h g<sup>-1</sup>. Interestingly, these values of specific capacities and capacity retention are very similar to those obtained previously with a S/CB@Co(OH)<sub>2</sub> cathode.<sup>390</sup> A particular effect of different metal atoms (*i.e.* Co or Ni) in the hydroxide nanomaterial may play a rather unspecific role in the interaction with sulfur-based species. Jiang *et al.* proposed a Ni<sub>3</sub>(NO<sub>3</sub>)<sub>2</sub>(OH)<sub>4</sub> shell to effectively encapsulate sulfur in the form of a S/CB composite and expand the lifespan of the cathode.<sup>394</sup> This thin-layered Ni-based hydroxide is able to irreversibly react with Li<sup>+</sup> ions during the initial discharge/charge cycles to further form a stable and shelly (Li, Ni)-mixed hydroxide protective film onto the S/CB composite (Fig. 16a). The formed thin film with functional polar/hydrophilic groups offers a good permeability to Li<sup>+</sup> and at the same time serves as a chemical anchor layer for LiPSs. As a result, an advanced hybrid cathode (sulfur content = 62.4%; sulfur loading = 1.8–2.5 mg cm<sup>-2</sup>) with a high reversible capacity of ≈1250 mA h g<sup>-1</sup> and a high coulombic efficiency of ≈98% after 500 cycles at 0.2C is achieved. In contrast, the S/CB composite in the absence of the Ni-based hydroxide exhibits both a low capacity and a low coulombic efficiency of, respectively, ≈200 mA h g<sup>-1</sup> and ≈52% after only 300 cycles (Fig. 16b). Lou's group suggested an interesting sulfur host based on double-shelled nanocages with Co(OH)<sub>2</sub> and Ni, Co-based layered double hydroxides as, respectively, inner and outer shells (denoted as CH@Ni,Co-LDH).<sup>395</sup> The outer LDH shell is a class of synthetic anionic clay with a 2D lamellar structure whose chemical formula, based on the used molar Ni/Co ratio of 1 : 2, is expressed as [Ni<sup>2+</sup><sub>1/3</sub>Co<sup>3+</sup><sub>2/3</sub>(OH)<sub>2</sub>][NO<sub>3</sub><sup>2-</sup><sub>1/3</sub>]·mH<sub>2</sub>O. The as-obtained CH@Ni,Co-LDH composite with a hollow polyhedral structure and a specific surface area of 117 m<sup>2</sup> g<sup>-1</sup> is able to accommodate a sulfur content of 75 wt%. The resulting cathode with a high sulfur loading of 3 mg cm<sup>-2</sup> (sulfur content of the whole cathode = 52.5 wt%) demonstrated stable cyclability at both 0.1 and 0.5C, with ending capacities of, respectively, 653 and 491 mA h g<sup>-1</sup> at the 100<sup>th</sup> cycle and corresponding capacity degradation rates of 0.356 and 0.343% per cycle. The good performance of the cathode was ascribed to the structure of the novel hydroxide-based host capable of accommodating a large amount of active sulfur material and its singular hydroxy-functionalized polar surfaces with strong binding affinity to LiPSs; however the latter was not experimentally demonstrated in this work. Recently, Zhang and co-





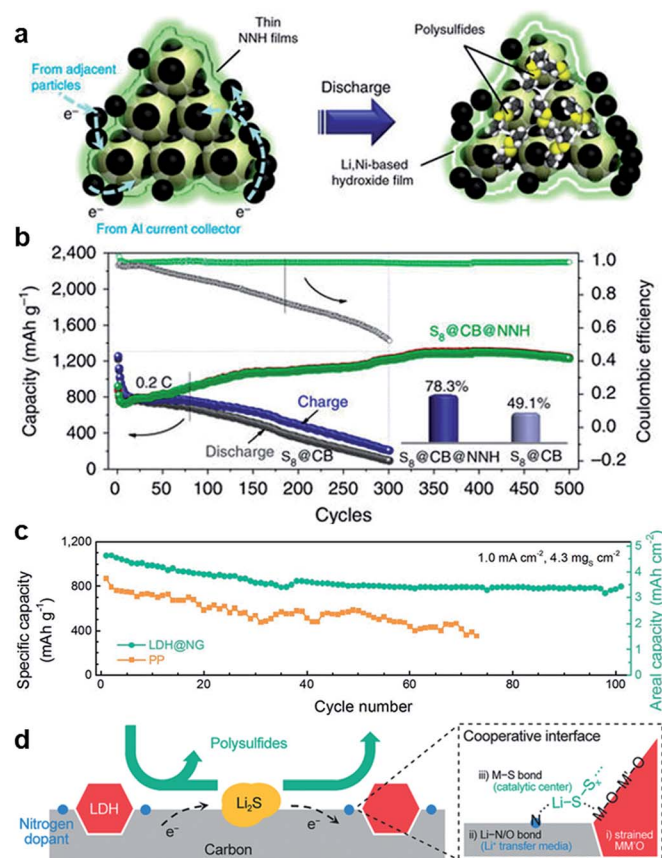


**Fig. 16** (a) A schematic illustration showing the working mechanisms of NNH in the sulfur cathodes. (b) Cycling performance of cathodes with and without the (Li, Ni)-mixed hydroxide denoted as S<sub>8</sub>@CB@NNH and S<sub>8</sub>@CB, respectively. The inset shows their utilization ratio of active sulfur.<sup>394</sup> (c) Cycling performance of cells with pristine and LDH@NG-coated separators. (d) A scheme showing the cooperative interface of LDH@NG, where the adsorption and redox of LiPSs are facilitated by the binding of Li and S surface species.<sup>396</sup> (a and b) Reproduced with permission from ref. 394. Creative Commons Attribution 4.0 International License (<http://creativecommons.org/licenses/by/4.0/>). (c and d) Reproduced with permission from ref. 396. Copyright 2016, Wiley-VCH.

workers also proposed the use of layered double hydroxides, but in this case the authors engineered Ni,Fe-layered double hydroxides (size < 5 nm) embedded in an N-doped mesoporous graphene framework (Ni,Fe-LDH@NG) serving as “sulfophilic” and “lithiophilic” components, respectively.<sup>396</sup> Interestingly, the subtle Ni,Fe-LDH@NG composite was coated on one side of a commercial polypropylene (Celgard 2400) separator instead of adding it to the sulfur cathode. Despite the use of a simple ball-milled sulfur/carbon cathode with a sulfur content of 63 wt% and a high areal sulfur loading of 4.3 mg cm<sup>-2</sup>, the cell with the Ni,Fe-LDH@NG-coated separator (added coating mass of 0.3 mg cm<sup>-2</sup>) revealed a high initial capacity of 1078 mA h g<sup>-1</sup> (areal capacity = 4.6 mA h cm<sup>-2</sup>) at a current density of 1 mA cm<sup>-2</sup>; while the reversible capacity, after 100 cycles, was sustained at 800 mA h g<sup>-1</sup> (3.4 mA h cm<sup>-2</sup>). In contrast, the reference cell with a pristine separator showed a capacity of 400 mA h g<sup>-1</sup> (1.5 mA h cm<sup>-2</sup>) after only 60 cycles, under similar cell conditions

(Fig. 16c). The stable cell operation at such a high sulfur loading was attributed to the cooperative “sulfophilic” and “lithiophilic” domains of the Ni,Fe-LDH@NG complex which cooperatively chemisorbs LiPS intermediates by either “lithiophilic” (via Li–N bonds) or “sulfophilic” (via S–Fe bonds) interactions and catalyzes efficiently interfacial redox reactions, as it was supported by XRD and XPS studies. The cooperative interface of Ni,Fe-LDH@NG is schematically illustrated in Fig. 16d. As a somewhat exotic system, a MgBO<sub>2</sub>(OH)/CNT composite was used to functionalize a usual Celgard 2400 separator and enabled high sulfur retention, rapid redox kinetics and Li<sup>+</sup> ion transport along with a high mechanical stability, especially at elevated temperatures of up to 140 °C.<sup>397</sup>

Nanostructured metal hydroxides with abundant functional polar/hydrophilic groups have proven to improve the cycling performance of Li–S batteries. However, the working mechanism of the metal hydroxide in the sulfur cathodes was not clearly explained. The interactions between LiPS species and metal hydroxides with different morphologies and chemical properties should be further examined by combining direct experimental investigations and theoretical studies. Only then we can gain new insights and identify the actual effect of the novel materials and whether the discussion on how the materials work is reasonable.

## 8. Future prospects and conclusions

In this condensed review, we handled numerous metal-based materials which have already proved their high impact on each part of the secondary Li–S battery cells. Their use as additives to improve cathodes, anodes or separators as well as the possibility to form an active material *in situ* inside a battery gives a large scope to optimize Li–S batteries to a certain extent and improve the possibility to be successfully introduced into the market.

Metal-based materials are typically polar, and they may effectively adsorb or even bind LiPS intermediates. However, the literature reports a huge number of metal-based compounds with different (nano)structures and surface chemistry to electrochemically convert LiPSs. It is a great challenge to figure out the most promising metal-based compounds to rationally design electrode materials for Li–S batteries since there are numerous key factors that influence the relationship between material properties and Li–S cell performance: (i) the surface polarity to adsorb/bind LiPS intermediates, (ii) the electrocatalytic effect of the material which may act as a redox mediator in the multielectron conversion chemistry of sulfur, (iii) the electrical conductivity of the material or the composite electrode, influencing the electron transport, the cell resistance and seemingly electron transfer, and (iv) the physical and morphological features (particle size, surface area, pore size, pore volume, *etc.*) that have a strong impact on the contact between the active phase and both the active material and the electrolyte as well as on LiPS confinement.

In each section we discussed concepts which show highly interesting results that, despite still being far away from the practical needs of a market-ready Li–S battery, are encouraging to go beyond classical concepts and try novel, innovative experiments that help to understand reaction and deactivation



mechanisms. Especially, the latter will allow us to overcome certain problems of Li-S batteries to expand the lifetime and to improve energy densities or to overcome safety and reliability concerns.

Of course, a large variety of individual materials does not facilitate an early application and market introduction of a new battery chemistry, as Li-S still is. With a powerful world's scientific community, this mega challenge will be solved with the desired outcome, affordable commercial Li-S batteries.

Many reports with outstanding and promising high-performance Li-S cells are far from practical applications. One of the issues is related to the complex multistep method used to prepare the metal-based material and/or sulfur composite cathode, making it unattractive in terms of cost-benefit for large-scale industrialization. The second concern is the low areal sulfur loading of  $0.5\text{--}2.0\text{ mg cm}^{-2}$  typically used in most of the publications. For practical Li-S cells, a cathode sulfur content  $> 80\text{ wt\%}$ , sulfur loadings  $> 6\text{ mg cm}^{-2}$  and an electrolyte/sulfur ratio  $< 2\text{ mL g}^{-1}$  are required to provide competitive specific energies ( $\approx 500\text{ W h kg}^{-1}$ ) compared to high-voltage Li-ion cells. It is highly important that Li-S batteries operate at low electrolyte amounts, which is one of the most crucial parameters to achieve high energy density. To make the big jump from lab-scale to industrial-scale fabrication of Li-S batteries, several critical parameters should be considered: (i) sulfur content, (ii) sulfur areal loading, (iii) electrolyte/sulfur ratio, (iv) used electrolyte, (v) utilization of additive(s) and its concentration in the electrolyte (e.g.:  $\text{LiNO}_3$ ), (vi) applied current density, (vii) voltage window, and (viii) cell configuration. Furthermore, other significant parameters which are often not addressed in detail in the academic literature but are crucial for practical aspects should be considered: e.g. electrode thickness, type and mass of the substrate, porosity and surface area of the substrate and mass of the interlayer/coating layer if any.

Beyond all positive arguments for Li-S on behalf of the possible high performance and low cost in production and sales, attention should also be paid to the end of the use of this battery type. At the moment we are starting to recognize which unexpected impacts on the environmental system are accompanying hazardous waste. We should pay attention to applying environmentally friendly and harmless substances. They should be somehow biocompatible or not bioavailable where the latter might be quite challenging if nanoscale materials are used in the battery. This consideration is additionally of great importance, when considering accidents and release of highly active nanoscale compounds, by fire, crashes or other incidents. As these materials can also largely affect the environment, before an application, we should be aware of what really happens to biology in case of accidents and whether we can avoid this by carefully choosing the right components.

Additionally, we should be able to recycle Li-S batteries on a large scale. With probably expectable low price of a Li-S battery, the recycling of sulfur-based batteries may be easier and consequently cheaper than for classical Li-ion batteries. Since a first incineration step will directly evolve carbon and sulfur compounds, sulfur in particular can be recovered by typical gas

scrubbing from the exhaust. The other residues are preserved in the incineration ash and can be, e.g., (electro)chemically and fractionally reprocessed.

## Conflicts of interest

There are no conflicts to declare.

## Acknowledgements

We acknowledge the Agencia Nacional de Promoción Científica y Tecnológica (FONCYT-PICT no. 2017-0824) and Secretaría de Ciencia y Técnica de la Universidad Nacional de Río Cuarto (SECYT-UNRC) and the German Federal Ministry of Education and Research (BMBF) through the Excellent Battery – WING center “Batteries – Mobility in Saxony” (grant no. 03X4637C) for partially funding this work. Additional funding is gratefully provided by the European Union/European Regional Development Fund and the Free State of Saxony via the NaSBattSy project (SAB grant no. 100234960).

## Notes and references

- 1 B. Dunn, H. Kamath and J.-M. Tarascon, *Science*, 2011, **334**, 928–935.
- 2 M. M. Thackeray, C. Wolverton and E. D. Isaacs, *Energy Environ. Sci.*, 2012, **5**, 7854–7863.
- 3 V. Etacheri, R. Marom, R. Elazari, G. Salitra and D. Aurbach, *Energy Environ. Sci.*, 2011, **4**, 3243–3262.
- 4 A. Manthiram, Y. Fu, S.-H. Chung, C. Zu and Y.-S. Su, *Chem. Rev.*, 2014, **114**, 11751–11787.
- 5 Z. W. Seh, Y. Sun, Q. Zhang and Y. Cui, *Chem. Soc. Rev.*, 2016, **45**, 5605–5634.
- 6 M. Hagen, D. Hanselmann, K. Ahlbrecht, R. Maça, D. Gerber and J. Tübke, *Adv. Energy Mater.*, 2015, **5**, 1401986.
- 7 P. Adelhelm, P. Hartmann, C. L. Bender, M. Busche, C. Eufinger and J. Janek, *Beilstein J. Nanotechnol.*, 2015, **6**, 1016–1055.
- 8 D. A. Boyd, *Angew. Chem., Int. Ed.*, 2016, **55**, 15486–15502.
- 9 I. Kovalev, Y. Mikhaylik and T. Weiß, *High energy rechargeable Li-S battery development at Sion Power and BASF, Li-S Workshop*, Dresden, 2013.
- 10 R. V. Noorden, *Nature*, 2014, **507**, 26–28.
- 11 Tesla Model S, <https://www.tesla.com/models>, accessed September 2018.
- 12 Audi e-tron, <https://www.audi.com/en/models/e-tron.html>, accessed September 2018.
- 13 D. Zheng, G. Wang, D. Liu, J. Si, T. Ding, D. Qu, X. Yang and D. Qu, *Adv. Mater. Technol.*, 2018, **3**, 1700233.
- 14 R. Xu, J. Lu and K. Amine, *Adv. Energy Mater.*, 2015, **5**, 1500408.
- 15 Q. Wang, J. Zheng, E. Walter, H. Pan, D. Lv, P. Zuo, H. Chen, Z. D. Deng, B. Y. Liaw, X. Yu, X. Yang, J.-G. Zhang, J. Liu and J. Xiao, *J. Electrochem. Soc.*, 2015, **162**, A474–A478.
- 16 Y. V. Mikhaylik and J. R. Akridge, *J. Electrochem. Soc.*, 2004, **151**, A1969–A1976.



- 17 M. R. Busche, P. Adelhelm, H. Sommer, H. Schneider, K. Leitner and J. Janek, *J. Power Sources*, 2014, **259**, 289–299.
- 18 Y. Yang, G. Zheng and Y. Cui, *Chem. Soc. Rev.*, 2013, **42**, 3018–3032.
- 19 X. Ji, K. T. Lee and L. F. Nazar, *Nat. Mater.*, 2009, **8**, 500–506.
- 20 H. Kim, H.-D. Lim, J. Kim and K. Kang, *J. Mater. Chem. A*, 2014, **2**, 33–47.
- 21 Z. Li, Y. Huang, L. Yuan, Z. Hao and Y. Huang, *Carbon*, 2015, **92**, 41–63.
- 22 J.-G. Wang, K. Xie and B. Wei, *Nano Energy*, 2015, **15**, 413–444.
- 23 S. Wu, R. Ge, M. Lu, R. Xu and Z. Zhang, *Nano Energy*, 2015, **15**, 379–405.
- 24 S. Rehman, K. Khan, Y. Zhao and Y. Hou, *J. Mater. Chem. A*, 2017, **5**, 3014–3038.
- 25 H.-J. Peng, J.-Q. Huang, X.-B. Cheng and Q. Zhang, *Adv. Energy Mater.*, 2017, **7**, 1700260.
- 26 R. Fang, S. Zhao, Z. Sun, D.-W. Wang, H.-M. Cheng and F. Li, *Adv. Mater.*, 2017, **29**, 1606823.
- 27 X. Chen, T. Hou, K. A. Persson and Q. Zhang, *Mater. Today*, 2018, DOI: 10.1016/j.mattod.2018.04.007.
- 28 L. Kong, H.-J. Peng, J.-Q. Huang and Q. Zhang, *Nano Res.*, 2017, **10**, 4027–4054.
- 29 J.-Q. Huang, Q. Zhang and F. Wei, *Energy Storage Mater.*, 2015, **1**, 127–145.
- 30 L. Borchardt, M. Oschatz and S. Kaskel, *Chem.–Eur. J.*, 2016, **22**, 7324–7351.
- 31 S. S. Zhang, *J. Electrochem. Soc.*, 2012, **159**, A920–A923.
- 32 S. S. Zhang, *Electrochim. Acta*, 2012, **70**, 344–348.
- 33 Y. Yang, G. Yu, J. J. Cha, H. Wu, M. Vosgueritchian, Y. Yao, Z. Bao and Y. Cui, *ACS Nano*, 2011, **5**, 9187–9193.
- 34 Y. Fu and A. Manthiram, *Chem. Mater.*, 2012, **24**, 3081–3087.
- 35 W. Zhou, Y. Yu, H. Chen, F. J. DiSalvo and H. D. Abruña, *J. Am. Chem. Soc.*, 2013, **135**, 16736–16743.
- 36 J.-Q. Huang, Q. Zhang and F. Wei, *Energy Storage Mater.*, 2015, **1**, 127–145.
- 37 X. Liu, J.-Q. Huang, Q. Zhang and L. Mai, *Adv. Mater.*, 2017, **29**, 1601759.
- 38 H. J. Peng, J. Q. Huang and Q. Zhang, *Chem. Soc. Rev.*, 2017, **46**, 5237–5288.
- 39 D. Liu, C. Zhang, G. Zhou, W. Lv, G. Ling, L. Zhi and Q.-H. Yang, *Adv. Sci.*, 2017, **5**, 1700270.
- 40 Z.-W. Zhang, H.-J. Peng, M. Zhao and J.-Q. Huang, *Adv. Funct. Mater.*, 2018, **28**, 1707536.
- 41 M.-S. Song, S.-C. Han, H.-S. Kim, J.-H. Kim, K.-T. Kim, Y.-M. Kang, H.-J. Ahn, S. Dou and J.-Y. Lee, *J. Electrochem. Soc.*, 2004, **151**, A791–A795.
- 42 Y. J. Choi, B. S. Jung, D. J. Lee, J. H. Jeong, K. W. Kim, H. J. Ahn, K. K. Cho and H. B. Gu, *Phys. Scr.*, 2007, **2007**, 62.
- 43 Y. Zhang, X. Wu, H. Feng, L. Wang, A. Zhang, T. Xia and H. Dong, *Int. J. Hydrogen Energy*, 2009, **34**, 1556–1559.
- 44 X. Ji, S. Evers, R. Black and L. F. Nazar, *Nat. Commun.*, 2011, **2**, 325.
- 45 S. Evers, T. Yim and L. F. Nazar, *J. Phys. Chem. C*, 2012, **116**, 19653–19658.
- 46 V. Lapornik, N. N. Tutar, A. Ristic, R. K. Chellappan, D. Foix, R. Dedryvère, M. Gaberscek and R. Dominko, *J. Power Sources*, 2015, **274**, 1239–1248.
- 47 R. Ponraj, A. G. Kannan, J. H. Ahn and D.-W. Kim, *ACS Appl. Mater. Interfaces*, 2016, **8**, 4000–4006.
- 48 K. Xie, Y. You, K. Yuan, W. Lu, K. Zhang, F. Xu, M. Ye, S. Ke, C. Shen and X. Zeng, *Adv. Mater.*, 2017, **29**, 1604724.
- 49 Z. W. Seh, W. Li, J. J. Cha, G. Zheng, Y. Yang, M. T. McDowell, P.-C. Hsu and Y. Cui, *Nat. Commun.*, 2013, **4**, 1331.
- 50 Z. Liang, G. Zheng, W. Li, Z. W. Seh, H. Yao, K. Yan, D. Kong and Y. Cui, *ACS Nano*, 2014, **8**, 5249–5256.
- 51 Z.-Z. Yang, H.-Y. Wang, L. Lu, C. Wang, X.-B. Zhong, J.-G. Wang and Q.-C. Jiang, *Sci. Rep.*, 2016, **6**, 22990.
- 52 Q. Sun, K. Chen, Y. Liu, Y. Li and M. Wei, *Chem.–Eur. J.*, 2017, **23**, 16312–16318.
- 53 K. Xie, Y. Han, W. Wei, H. Yu, C. Zhang, J.-G. Wang, W. Lu and B. Wei, *RSC Adv.*, 2015, **5**, 77348–77353.
- 54 Q. Pang, D. Kundu, M. Cuisinier and L. Nazar, *Nat. Commun.*, 2014, **5**, 4759.
- 55 X. Tao, J. Wang, Z. Ying, Q. Cai, G. Zheng, Y. Gan, H. Huang, Y. Xia, C. Liang, W. Zhang and Y. Cui, *Nano Lett.*, 2014, **14**, 5288–5294.
- 56 J. Smith, F. Walsh and R. Clarke, *J. Appl. Electrochem.*, 1998, **28**, 1021–1033.
- 57 T. Lei, W. Chen, J. Huang, C. Yan, H. Sun, C. Wang, W. Zhang, Y. Li and J. Xiong, *Adv. Energy Mater.*, 2017, **7**, 1601843.
- 58 Q. Fan, W. Liu, Z. Weng, Y. Sun and H. Wang, *J. Am. Chem. Soc.*, 2015, **137**, 12946–12953.
- 59 J. Guo, X. Zhang, X. Du and F. Zhang, *J. Mater. Chem. A*, 2017, **5**, 6447–6454.
- 60 H. Wei, E. F. Rodriguez, A. S. Best, A. F. Hollenkamp, D. Chen and R. A. Caruso, *Adv. Energy Mater.*, 2017, **7**, 1601616.
- 61 X. Liang, C. Hart, Q. Pang, A. Garsuch, T. Weiss and L. F. Nazar, *Nat. Commun.*, 2015, **6**, 5682.
- 62 N. Wiberg, A. Holleman and E. Wiberg, *Inorganic Chemistry*, Academic Press, San Diego, 101<sup>st</sup> edn, 2001.
- 63 Q. Pang, X. Liang, C. Y. Kwok and L. F. Nazar, *J. Electrochem. Soc.*, 2015, **162**, A2567–A2576.
- 64 X. Liang and L. F. Nazar, *ACS Nano*, 2016, **10**, 4192–4198.
- 65 X. Wang, G. Li, J. Li, Y. Zhang, A. Wook, A. Yu and Z. Chen, *Energy Environ. Sci.*, 2016, **9**, 2533–2538.
- 66 X. Liang, C. Y. Kwok, F. Lodi-Marzano, Q. Pang, M. Cuisinier, H. Huang, C. J. Hart, D. Houtarde, K. Kaup, H. Sommer, T. Brezesinski, J. Janek and L. F. Nazar, *Adv. Energy Mater.*, 2016, **6**, 1501636.
- 67 Q. Zhang, Y. Wang, Z. W. Seh, Z. Fu, R. Zhang and Y. Cui, *Nano Lett.*, 2015, **15**, 3780–3786.
- 68 K. Luan, S. Yao, Y. Zhang, R. Zhuang, J. Xiang, X. Shen, T. Li, K. Xiao and S. Qin, *Electrochim. Acta*, 2017, **252**, 461–469.
- 69 L. Ni, Z. Wu, G. Zhao, C. Sun, C. Zhou, X. Gong and G. Diao, *Small*, 2017, **13**, 1603466.
- 70 K. Cao, H. Liu, Y. Li, Y. Wang and L. Jiao, *Energy Storage Mater.*, 2017, **9**, 78–84.
- 71 G. Radhika, R. Subadevi, K. Krishnaveni, W.-R. Liu and M. Sivakumar, *J. Nanosci. Nanotechnol.*, 2018, **18**, 127–131.





- 72 B. Campbell, J. Bell, H. Hosseini Bay, Z. Favors, R. Ionescu, C. S. Ozkan and M. Ozkan, *Nanoscale*, 2015, **7**, 7051–7055.
- 73 M. Xue, Y. Zhou, J. Geng, P. Zeng, Y. Xu, Y. Wang, W. Tang, P. Wu, S. Wei and Y. Zhou, *RSC Adv.*, 2016, **6**, 91179–91184.
- 74 H. Tang, S. Yao, M. Jing, X. Wu, J. Hou, X. Qian, D. Rao, X. Shen, X. Xi and K. Xiao, *J. Alloys Compd.*, 2015, **650**, 351–356.
- 75 Y. Zhang, Y. Zhao, A. Yermukhambetova, Z. Bakenov and P. Chen, *J. Mater. Chem. A*, 2013, **1**, 295–301.
- 76 S. Wu, Y. Wang, S. Na, C. Chen, T. Yu, H. Wang and H. Zang, *J. Mater. Chem. A*, 2017, **5**, 17352–17359.
- 77 H. Cheng, S. Wang, D. Tao and M. Wang, *Funct. Mater. Lett.*, 2014, **07**, 1450020.
- 78 H. Wang, T. Zhou, D. Li, H. Gao, G. Gao, A. Du, H. Liu and Z. Guo, *ACS Appl. Mater. Interfaces*, 2017, **9**, 4320–4325.
- 79 A. Iqbal, Z. Ali Ghazi, A. Muqsit Khattak and A. Ahmad, *J. Solid State Chem.*, 2017, **256**, 189–195.
- 80 Q. Qu, T. Gao, H. Zheng, Y. Wang, X. Li, X. Li, J. Chen, Y. Han, J. Shao and H. Zheng, *Adv. Mater. Interfaces*, 2015, **2**, 1500048.
- 81 B. Hu, L. Mai, W. Chen and F. Yang, *ACS Nano*, 2009, **3**, 478–482.
- 82 L. Zhang, Y. Wang, Z. Niu and J. Chen, *Carbon*, 2019, **141**, 400–416.
- 83 F. Sun, J. Wang, D. Long, W. Qiao, L. Ling, C. Lv and R. Cai, *J. Mater. Chem. A*, 2013, **1**, 13283–13289.
- 84 X. Tao, J. Wang, C. Liu, H. Wang, H. Yao, G. Zheng, Z. W. Seh, Q. Cai, W. Li, G. Zhou, C. Zu and Y. Cui, *Nat. Commun.*, 2016, **7**, 11203.
- 85 R. Wang, K. Wang, S. Gao, M. Jiang, M. Zhou, S. Cheng and K. Jiang, *Nanoscale*, 2017, **9**, 14881–14887.
- 86 H. Wu, Q. Tang, H. Fan, Z. Liu, A. Hu, S. Zhang, W. Deng and X. Chen, *Electrochim. Acta*, 2017, **255**, 179–186.
- 87 Z. Li, N. Zhang, Y. Sun, H. Ke and H. Cheng, *J. Energy Chem.*, 2017, **26**, 1267–1275.
- 88 H. Yao, G. Zheng, P.-C. Hsu, D. Kong, J. J. Cha, W. Li, Z. W. Seh, M. T. McDowell, K. Yan, Z. Liang, V. K. Narasimhan and Y. Cui, *Nat. Commun.*, 2014, **5**, 3943.
- 89 G. Zhou, Y. Zhao, C. Zu and A. Manthiram, *Nano Energy*, 2015, **12**, 240–249.
- 90 Z. Zhang, Q. Li, S. Jiang, K. Zhang, Y. Lai and J. Li, *Chem.–Eur. J.*, 2015, **21**, 1343–1349.
- 91 L. Gao, M. Cao, Y. Q. Fu, Z. Zhong, Y. Shen and M. Wang, *J. Mater. Chem. A*, 2016, **4**, 16454–16461.
- 92 M. Yu, J. Ma, H. Song, A. Wang, F. Tian, Y. Wang, H. Qiu and R. Wang, *Energy Environ. Sci.*, 2016, **9**, 1495–1503.
- 93 S. R. Azari, M. S. Rahmanifar, M. F. El-Kady, A. Noori, M. F. Mousavi and R. B. Kaner, *J. Iran. Chem. Soc.*, 2017, **14**, 2579–2590.
- 94 J.-Y. Hwang, H. M. Kim, S.-K. Lee, J.-H. Lee, A. Abouimrane, M. A. Khaleel, I. Belharouak, A. Manthiram and Y.-K. Sun, *Adv. Energy Mater.*, 2016, **6**, 1501480.
- 95 G. D. Park, J. Lee, Y. Piao and Y. C. Kang, *Chem. Eng. J.*, 2018, **335**, 600–611.
- 96 J. Song, J. Zheng, S. Feng, C. Zhu, S. Fu, W. Zhao, D. Du and Y. Lin, *Carbon*, 2018, **128**, 63–69.
- 97 M. Fang, Z. Chen, Y. Liu, J. Quan, C. Yang, L. Zhu, Q. Xu and Q. Xu, *J. Mater. Chem. A*, 2018, **6**, 1630–1638.
- 98 X. Shang, P. Guo, T. Qin, M. Liu, M. Lv, D. Liu and D. He, *Adv. Mater. Interfaces*, 2018, **5**, 1701602.
- 99 X. Zhao, Q. Li, T. Yu, M. Yang, K. Fink and X. Shen, *Sci. Rep.*, 2016, **6**, 19448.
- 100 Y. Chen, S. Choi, D. Su, X. Gao and G. Wang, *Nano Energy*, 2018, **47**, 331–339.
- 101 H. Tang, S. Yao, S. Xue, M. Liu, L. Chen, M. Jing, X. Shen, T. Li, K. Xiao and S. Qin, *Electrochim. Acta*, 2018, **268**, 158–167.
- 102 Z. Li, J. Zhang and X. W. D. Lou, *Angew. Chem., Int. Ed.*, 2015, **54**, 12886–12890.
- 103 J. Zhang, Y. Shi, Y. Ding, W. Zhang and G. Yu, *Nano Lett.*, 2016, **16**, 7276–7281.
- 104 Y. Li, D. Ye, W. Liu, B. Shi, R. Guo, H. Zhao, H. Pei, J. Xu and J. Xie, *ACS Appl. Mater. Interfaces*, 2016, **8**, 28566–28573.
- 105 W. Sun, X. Ou, X. Yue, Y. Yang, Z. Wang, D. Rooney and K. Sun, *Electrochim. Acta*, 2016, **207**, 198–206.
- 106 Y. Guo, N. T. Wu and Y. Zhang, *ECS Trans.*, 2017, **75**, 141–150.
- 107 L. Ni, G. Zhao, G. Yang, G. Niu, M. Chen and G. Diao, *ACS Appl. Mater. Interfaces*, 2017, **9**, 34793–34803.
- 108 G. Yuan, H. Jin, Y. Jin and L. Wu, *J. Solid State Electrochem.*, 2017, **22**, 693–703.
- 109 Y. Li, B. Shi, W. Liu, R. Guo, H. Pei, D. Ye, J. Xie and J. Kong, *Electrochim. Acta*, 2018, **260**, 912–920.
- 110 M. He, P. Zuo, H. Zhang, J. Hua, Y. Ma, C. Du, X. Cheng, Y. Gao and G. Yin, *Electrochim. Acta*, 2018, **259**, 440–448.
- 111 M. Chen, Q. Lu, S. Jiang, C. Huang, X. Wang, B. Wu, K. Xiang and Y. Wu, *Chem. Eng. J.*, 2018, **335**, 831–842.
- 112 Z. Li, *R. Soc. Open Sci.*, 2018, **5**, 171824.
- 113 X. Chen, L. Yuan, Z. Hao, X. Liu, J. Xiang, Z. Zhang, Y. Huang and J. Xie, *ACS Appl. Mater. Interfaces*, 2018, **10**, 13406–13412.
- 114 M. Xiang, H. Wu, H. Liu, J. Huang, Y. Zheng, L. Yang, P. Jing, Y. Zhang, S. Dou and H. Liu, *Adv. Funct. Mater.*, 2017, **27**, 1702573.
- 115 Y. Song, W. Zhao, X. Zhu, L. Zhang, Q. Li, F. Ding, Z. Liu and J. Sun, *ACS Appl. Mater. Interfaces*, 2018, **10**, 15733–15741.
- 116 R. Tang, X. Li, Z. Ding and L. Zhang, *RSC Adv.*, 2016, **6**, 65162–65170.
- 117 L. Liu, Q. Yang, M. Jiang, S. Wang, B. Liu, D. Fang, J. Huang, Q. Wang, L. Dong and C. Xiong, *J. Mater. Res.*, 2017, **33**, 1226–1235.
- 118 X. Qian, L. Jin, L. Zhu, S. Yao, D. Rao, X. Shen, X. Xi, K. Xiao and S. Qin, *RSC Adv.*, 2016, **6**, 111190–111196.
- 119 L. Ma, R. Chen, G. Zhu, Y. Hu, Y. Wang, T. Chen, J. Liu and Z. Jin, *ACS Nano*, 2017, **11**, 7274–7283.
- 120 C. Wan, W. Wu, C. Wu, J. Xu and L. Guan, *RSC Adv.*, 2015, **5**, 5102–5106.
- 121 Y. Zhou, C. Zhou, Q. Li, C. Yan, B. Han, K. Xia, Q. Gao and J. Wu, *Adv. Mater.*, 2015, **27**, 3774–3781.
- 122 Y. Li, J. Zhu, R. Shi, M. Dirican, P. Zhu, C. Yan, H. Jia, J. Zang, J. He and X. Zhang, *Chem. Eng. J.*, 2018, **349**, 376–387.



- 123 Y. Tao, Y. Wei, Y. Liu, J. Wang, W. Qiao, L. Ling and D. Long, *Energy Environ. Sci.*, 2016, **9**, 3230–3239.
- 124 M. Wang, L. Fan, X. Wu, D. Tian, J. Cheng, Y. Qiu, H. Wu, B. Guan, N. Zhang, K. Sun and Y. Wang, *J. Mater. Chem. A*, 2017, **5**, 19613–19618.
- 125 X. Gu, C.-J. Tong, B. Wen, L.-M. Liu, C. Lai and S. Zhang, *Electrochim. Acta*, 2016, **196**, 369–376.
- 126 Y. Kong, J. Luo, C. Jin, H. Yuan, O. Sheng, L. Zhang, C. Fang, W. Zhang, H. Huang, Y. Xia, C. Liang, J. Zhang, Y. Gan and X. Tao, *Nano Res.*, 2017, **11**, 477–489.
- 127 C. Zheng, S. Niu, W. Lv, G. Zhou, J. Li, S. Fan, Y. Deng, Z. Pan, B. Li, F. Kang and Q.-H. Yang, *Nano Energy*, 2017, **33**, 306–312.
- 128 J. He, L. Luo, Y. Chen and A. Manthiram, *Adv. Mater.*, 2017, **29**, 1702707.
- 129 L. Hu, C. Dai, H. Liu, Y. Li, B. Shen, Y. Chen, S. J. Bao and M. Xu, *Adv. Energy Mater.*, 2018, **8**, 1800709.
- 130 X. Wu, Y. Du, P. Wang, L. Fan, J. Cheng, M. Wang, Y. Qiu, B. Guan, H. Wu and N. Zhang, *J. Mater. Chem. A*, 2017, **5**, 25187–25192.
- 131 L. Luo, X. Qin, J. Wu, G. Liang, Q. Li, M. Liu, F. Kang, G. Chen and B. Li, *J. Mater. Chem. A*, 2018, **6**, 8612–8619.
- 132 L. Zhou, N. Ding, J. Yang, L. Yang, Y. Zong, Z. Liu and A. Yu, *ACS Sustainable Chem. Eng.*, 2016, **4**, 3679–3687.
- 133 Z. Ding, X. Li, P. Zhang, J. Yu and Y. Hua, *New J. Chem.*, 2017, **41**, 12726–12735.
- 134 X. Li, L. Zhang, Z. Ding and Y. He, *J. Electroanal. Chem.*, 2017, **799**, 617–624.
- 135 L. Kong, X. Chen, B.-Q. Li, H.-J. Peng, J.-Q. Huang, J. Xie and Q. Zhang, *Adv. Mater.*, 2017, **30**, 1705219.
- 136 Y. Fu, Y.-S. Su and A. Manthiram, *Angew. Chem.*, 2013, **125**, 7068–7073.
- 137 C. Zu, Y. Fu and A. Manthiram, *J. Mater. Chem. A*, 2013, **1**, 10362–10367.
- 138 K. Han, J. Shen, S. Hao, H. Ye, C. Wolverton, M. C. Kung and H. H. Kung, *ChemSusChem*, 2014, **7**, 2545–2553.
- 139 S. D. Shenoy, P. A. Joy and M. R. Anantharaman, *J. Magn. Magn. Mater.*, 2004, **269**, 217–226.
- 140 C. Vidal-Abarca, P. Lavela and J. L. Tirado, *J. Phys. Chem. C*, 2010, **114**, 12828–12832.
- 141 S. Yuan, Z. Guo, L. Wang, S. Hu, Y. Wang and Y. Xia, *Adv. Sci.*, 2015, **2**, 1500071.
- 142 W. Kong, L. Yan, Y. Luo, D. Wang, K. Jiang, Q. Li, S. Fan and J. Wang, *Adv. Funct. Mater.*, 2017, **27**, 1606663.
- 143 X. Fang and H. Peng, *Small*, 2015, **11**, 1488–1511.
- 144 R. Chen, T. Zhao and F. Wu, *Chem. Commun.*, 2015, **51**, 18–33.
- 145 R. Demir-Cakan, *Li-S Batteries*, World Scientific Publishing Co., New Jersey, 2017.
- 146 Y.-S. Su and A. Manthiram, *Nat. Commun.*, 2012, **3**, 1166.
- 147 Y.-S. Su and A. Manthiram, *Chem. Commun.*, 2012, **48**, 8817–8819.
- 148 J. Balach, T. Jaumann, M. Klose, S. Oswald, J. Eckert and L. Giebeler, *J. Phys. Chem. C*, 2015, **119**, 4580–4587.
- 149 S.-H. Chung and A. Manthiram, *J. Phys. Chem. Lett.*, 2014, **5**, 1978–1983.
- 150 S.-H. Chung and A. Manthiram, *Adv. Funct. Mater.*, 2014, **24**, 5299–5306.
- 151 S.-H. Chung and A. Manthiram, *Adv. Mater.*, 2014, **26**, 7352–7357.
- 152 J.-Q. Huang, Z.-L. Xu, S. Abouali, M. Akbari Garakani and J.-K. Kim, *Carbon*, 2016, **99**, 624–632.
- 153 H.-S. Kang and Y.-K. Sun, *Adv. Funct. Mater.*, 2016, **26**, 1225–1232.
- 154 H. J. Peng, D. W. Wang, J. Q. Huang, X. B. Cheng, Z. Yuan, F. Wei and Q. Zhang, *Adv. Sci.*, 2016, **3**, 1500268.
- 155 J. Sun, Y. Sun, M. Pasta, G. Zhou, Y. Li, W. Liu, F. Xiong and Y. Cui, *Adv. Mater.*, 2016, **28**, 9797–9803.
- 156 H. Yao, K. Yan, W. Li, G. Zheng, D. Kong, Z. W. Seh, V. K. Narasimhan, Z. Liang and Y. Cui, *Energy Environ. Sci.*, 2014, **7**, 3381–3390.
- 157 Z. Zhang, G. Wang, Y. Lai, J. Li, Z. Zhang and W. Chen, *J. Power Sources*, 2015, **300**, 157–163.
- 158 J. Balach, T. Jaumann, M. Klose, S. Oswald, J. Eckert and L. Giebeler, *Adv. Funct. Mater.*, 2015, **25**, 5285–5291.
- 159 J. Balach, T. Jaumann, M. Klose, S. Oswald, J. Eckert and L. Giebeler, *J. Power Sources*, 2016, **303**, 317–324.
- 160 J. Song, Z. Yu, M. L. Gordin and D. Wang, *Nano Lett.*, 2016, **16**, 864–870.
- 161 J. Balach, H. K. Singh, S. Gomoll, T. Jaumann, M. Klose, S. Oswald, M. Richter, J. Eckert and L. Giebeler, *ACS Appl. Mater. Interfaces*, 2016, **8**, 14586–14595.
- 162 C. Jin, W. Zhang, Z. Zhuang, J. Wang, H. Huang, Y. Gan, Y. Xia, C. Liang, J. Zhang and X. Tao, *J. Mater. Chem. A*, 2017, **5**, 632–640.
- 163 S. H. Chung and A. Manthiram, *Adv. Mater.*, 2014, **26**, 7352–7357.
- 164 I. Bauer, S. Thieme, J. Brückner, H. Althues and S. Kaskel, *J. Power Sources*, 2014, **251**, 417–422.
- 165 J.-Q. Huang, Q. Zhang, H.-J. Peng, X.-Y. Liu, W.-Z. Qian and F. Wei, *Energy Environ. Sci.*, 2014, **7**, 347–353.
- 166 Y. Chen, N. Liu, H. Shao, W. Wang, M. Gao, C. Li, H. Zhang, A. Wang and Y. Huang, *J. Mater. Chem. A*, 2015, **3**, 15235–15240.
- 167 Z. Zhang, Z. Zhang, J. Li and Y. Lai, *J. Solid State Electrochem.*, 2015, **19**, 1709–1715.
- 168 Z. Xiao, Z. Yang, L. Wang, H. Nie, M. e. Zhong, Q. Lai, X. Xu, L. Zhang and S. Huang, *Adv. Mater.*, 2015, **27**, 2891–2898.
- 169 G. Liang, J. Wu, X. Qin, M. Liu, Q. Li, Y.-B. He, J.-K. Kim, B. Li and F. Kang, *ACS Appl. Mater. Interfaces*, 2016, **8**, 23105–23113.
- 170 G. Xu, J. Yuan, X. Tao, B. Ding, H. Dou, X. Yan, Y. Xiao and X. Zhang, *Nano Res.*, 2015, **8**, 3066–3074.
- 171 F. Li, G. Wang, P. Wang, J. Yang, K. Zhang, Y. Liu and Y. Lai, *J. Electroanal. Chem.*, 2017, **788**, 150–155.
- 172 Y. An, Z. Zhang, H. Fei, S. Xiong, B. Ji and J. Feng, *ACS Appl. Mater. Interfaces*, 2017, **9**, 12400–12407.
- 173 L. Yang, G. Li, X. Jiang, T. Zhang, H. Lin and J. Y. Lee, *J. Mater. Chem. A*, 2017, **5**, 12506–12512.
- 174 T. Zhao, Y. Ye, C.-Y. Lao, G. Divitini, P. R. Coxon, X. Peng, X. He, H.-K. Kim, K. Xi, C. Ducati, R. Chen, Y. Liu, S. Ramakrishna and R. V. Kumar, *Small*, 2017, **13**, 1700357.
- 175 J. Liu, L. Yuan, K. Yuan, Z. Li, Z. Hao, J. Xiang and Y. Huang, *Nanoscale*, 2016, **8**, 13638–13645.



- 176 N. Hu, X. Lv, Y. Dai, L. Fan, D. Xiong and X. Li, *ACS Appl. Mater. Interfaces*, 2018, **10**, 18665–18674.
- 177 Y. Lai, P. Wang, F. Qin, M. Xu, J. Li, K. Zhang and Z. Zhang, *Energy Storage Mater.*, 2017, **9**, 179–187.
- 178 X. Qian, L. Jin, D. Zhao, X. Yang, S. Wang, X. Shen, D. Rao, S. Yao, Y. Zhou and X. Xi, *Electrochim. Acta*, 2016, **192**, 346–356.
- 179 T. Yim, S. H. Han, N. H. Park, M.-S. Park, J. H. Lee, J. Shin, J. W. Choi, Y. Jung, Y. N. Jo, J.-S. Yu and K. J. Kim, *Adv. Funct. Mater.*, 2016, **26**, 7817–7823.
- 180 J. Balach, T. Jaumann, S. Muhlenhoff, J. Eckert and L. Giebeler, *Chem. Commun.*, 2016, **52**, 8134–8137.
- 181 X. Qian, D. Zhao, L. Jin, S. Yao, D. Rao, X. Shen, Y. Zhou and X. Xi, *RSC Adv.*, 2016, **6**, 114989–114996.
- 182 H. Tang, S. Yao, J. Mi, X. Wu, J. Hou and X. Shen, *Mater. Lett.*, 2017, **186**, 127–130.
- 183 D. An, L. Shen, D. Lei, L. Wang, H. Ye, B. Li, F. Kang and Y.-B. He, *J. Energy Chem.*, 2018, DOI: 10.1016/j.jechem.2018.05.002.
- 184 F. Li, F. Qin, G. Wang, K. Zhang, P. Wang, Z. Zhang and Y. Lai, *RSC Adv.*, 2018, **8**, 1632–1637.
- 185 W. Li, J. Hicks-Garner, J. Wang, J. Liu, A. F. Gross, E. Sherman, J. Graetz, J. J. Vajo and P. Liu, *Chem. Mater.*, 2014, **26**, 3403–3410.
- 186 M. Liu, Q. Li, X. Qin, G. Liang, W. Han, D. Zhou, Y.-B. He, B. Li and F. Kang, *Small*, 2017, **13**, 1602539.
- 187 J. Li, Y. Huang, S. Zhang, W. Jia, X. Wang, Y. Guo, D. Jia and L. Wang, *ACS Appl. Mater. Interfaces*, 2017, **9**, 7499–7504.
- 188 X. Qian, D. Zhao, L. Jin, X. Shen, S. Yao, D. Rao, Y. Zhou and X. m. Xi, *Mater. Res. Bull.*, 2017, **94**, 104–112.
- 189 S. Wang, X. Qian, L. Jin, D. Rao, S. Yao, X. Shen, K. Xiao and S. Qin, *J. Solid State Electrochem.*, 2017, **21**, 3229–3236.
- 190 C. Li, S. Dong, D. Guo, Z. Zhang, M. Wang and L. Yin, *Electrochim. Acta*, 2017, **251**, 43–50.
- 191 E. J. Berg and S. Trabesinger, *J. Electrochem. Soc.*, 2018, **165**, A5001–A5005.
- 192 E. M. Fernández, P. G. Moses, A. Toftelund, H. A. Hansen, J. I. Martínez, F. Abild-Pedersen, J. Kleis, B. Hinnemann, J. Rossmeisl, T. Bligaard and J. K. Nørskov, *Angew. Chem., Int. Ed.*, 2008, **47**, 4683–4686.
- 193 Y. Du, X. Zhu, L. Si, Y. Li, X. Zhou and J. Bao, *J. Phys. Chem. C*, 2015, **119**, 15874–15881.
- 194 V. V. T. Doan-Nguyen, K. S. Subrahmanyam, M. M. Butala, J. A. Gerbec, S. M. Islam, K. N. Kanipe, C. E. Wilson, M. Balasubramanian, K. M. Wiaderek, O. J. Borkiewicz, K. W. Chapman, P. J. Chupas, M. Moskovits, B. S. Dunn, M. G. Kanatzidis and R. Seshadri, *Chem. Mater.*, 2016, **28**, 8357–8365.
- 195 N. Nitta, F. Wu, J. T. Lee and G. Yushin, *Mater. Today*, 2015, **18**, 252–264.
- 196 M.-R. Gao, Y.-F. Xu, J. Jiang and S.-H. Yu, *Chem. Soc. Rev.*, 2013, **42**, 2986–3017.
- 197 J. Cabana, L. Monconduit, D. Larcher and M. R. Palacín, *Adv. Mater.*, 2010, **22**, E170–E192.
- 198 Z. Yuan, H.-J. Peng, T.-Z. Hou, J.-Q. Huang, C.-M. Chen, D.-W. Wang, X.-B. Cheng, F. Wei and Q. Zhang, *Nano Lett.*, 2016, **16**, 519–527.
- 199 G. Zhou, H. Tian, Y. Jin, X. Tao, B. Liu, R. Zhang, Z. W. Seh, D. Zhuo, Y. Liu, J. Sun, J. Zhao, C. Zu, D. S. Wu, Q. Zhang and Y. Cui, *Proc. Natl. Acad. Sci. U. S. A.*, 2017, **114**, 840–845.
- 200 Q. Pang, D. Kundu and L. F. Nazar, *Mater. Horiz.*, 2016, **3**, 130–136.
- 201 X. Chen, H.-J. Peng, R. Zhang, T.-Z. Hou, J.-Q. Huang, B. Li and Q. Zhang, *ACS Energy Lett.*, 2017, **2**, 795–801.
- 202 H. Wang, Q. Zhang, H. Yao, Z. Liang, H.-W. Lee, P.-C. Hsu, G. Zheng and Y. Cui, *Nano Lett.*, 2014, **14**, 7138–7144.
- 203 J. Zhou, N. Lin, W. I. Cai, C. Guo, K. Zhang, J. Zhou, Y. Zhu and Y. Qian, *Electrochim. Acta*, 2016, **218**, 243–251.
- 204 Y. Yamaguchi, T. Takeuchi, H. Sakaebe, H. Kageyama, H. Senoh, T. Sakai and K. Tatsumi, *J. Electrochem. Soc.*, 2010, **157**, A630–A635.
- 205 U. K. Sen, P. Johari, S. Basu, C. Nayak and S. Mitra, *Nanoscale*, 2014, **6**, 10243–10254.
- 206 J. Balach, T. Jaumann and L. Giebeler, *Energy Storage Mater.*, 2017, **8**, 209–216.
- 207 J. W. Seo, Y. W. Jun, S. W. Park, H. Nah, T. Moon, B. Park, J. G. Kim, Y. J. Kim and J. Cheon, *Angew. Chem., Int. Ed.*, 2007, **46**, 8828–8831.
- 208 Y. Wang, J. Wu, Y. Tang, X. Lü, C. Yang, M. Qin, F. Huang, X. Li and X. Zhang, *ACS Appl. Mater. Interfaces*, 2012, **4**, 4246–4250.
- 209 N. Deprez and D. S. McLachlan, *J. Phys. D: Appl. Phys.*, 1988, **21**, 101–107.
- 210 G. Zheng, Q. Zhang, J. J. Cha, Y. Yang, W. Li, Z. W. Seh and Y. Cui, *Nano Lett.*, 2013, **13**, 1265–1270.
- 211 W. Ki, X. Huang, J. Li, D. L. Young and Y. Zhang, *J. Mater. Res.*, 2007, **22**, 1390–1395.
- 212 Y. Lu, X. Li, J. Liang, L. Hu, Y. Zhu and Y. Qian, *Nanoscale*, 2016, **8**, 17616–17622.
- 213 B. Liu, J. Yang, Y. Han, T. Hu, W. Ren, C. Liu, Y. Ma and C. Gao, *J. Appl. Phys.*, 2011, **109**, 053717.
- 214 Z. W. Seh, J. H. Yu, W. Li, P.-C. Hsu, H. Wang, Y. Sun, H. Yao, Q. Zhang and Y. Cui, *Nat. Commun.*, 2014, **5**, 5017.
- 215 L. E. Conroy and K. C. Park, *Inorg. Chem.*, 1968, **7**, 459–463.
- 216 A. V. Murugan, M. Quintin, M.-H. Delville, G. Campet and K. Vijayamohan, *J. Mater. Chem.*, 2005, **15**, 902–909.
- 217 T. A. Bither, R. Bouchard, W. Cloud, P. Donohue and W. Siemons, *Inorg. Chem.*, 1968, **7**, 2208–2220.
- 218 A. Voznyi, V. Kosyak, A. Opanasyuk, N. Tirkusova, L. Grase, A. Medvids and G. Mezinskis, *Mater. Chem. Phys.*, 2016, **173**, 52–61.
- 219 X. Li, Y. Lu, Z. Hou, W. Zhang, Y. Zhu, Y. Qian, J. Liang and Y. Qian, *ACS Appl. Mater. Interfaces*, 2016, **8**, 19550–19557.
- 220 C. I. Pearce, R. A. D. Patrick and D. J. Vaughan, *Rev. Mineral. Geochem.*, 2006, **61**, 127–180.
- 221 X. Li, J. Liang, Y. Lu, Z. Hou, W. Zhang, Y. Zhu and Y. Qian, *J. Power Sources*, 2016, **329**, 379–386.
- 222 N. Kumar, N. Raman and A. Sundaresan, *Z. Anorg. Allg. Chem.*, 2014, **640**, 1069–1074.
- 223 K. Sun, D. Su, Q. Zhang, D. C. Bock, A. C. Marschilok, K. J. Takeuchi, E. S. Takeuchi and H. Gan, *J. Electrochem. Soc.*, 2015, **162**, A2834–A2839.
- 224 R. C. Hoodless, R. B. Moyes and P. B. Wells, *Catal. Today*, 2006, **114**, 377–382.





- 225 L. Zhu, D. Susac, M. Teo, K. C. Wong, P. C. Wong, R. R. Parsons, D. Bizzotto, K. A. R. Mitchell and S. A. Campbell, *J. Catal.*, 2008, **258**, 235–242.
- 226 Z. Luo, C. Tan, X. Zhang, J. Chen, X. Cao, B. Li, Y. Zong, L. Huang, X. Huang, L. Wang, W. Huang and H. Zhang, *Small*, 2016, **12**, 5920–5926.
- 227 Z. Ma, Z. Li, K. Hu, D. Liu, J. Huo and S. Wang, *J. Power Sources*, 2016, **325**, 71–78.
- 228 H. Xu and A. Manthiram, *Nano Energy*, 2017, **33**, 124–129.
- 229 J. Pu, Z. Shen, J. Zheng, W. Wu, C. Zhu, Q. Zhou, H. Zhang and F. Pan, *Nano Energy*, 2017, **37**, 7–14.
- 230 T. Chen, Z. Zhang, B. Cheng, R. Chen, Y. Hu, L. Ma, G. Zhu, J. Liu and Z. Jin, *J. Am. Chem. Soc.*, 2017, **139**, 12710–12715.
- 231 T. Chen, L. Ma, B. Cheng, R. Chen, Y. Hu, G. Zhu, Y. Wang, J. Liang, Z. Tie, J. Liu and Z. Jin, *Nano Energy*, 2017, **38**, 239–248.
- 232 C. Dai, J. M. Lim, M. Wang, L. Hu, Y. Chen, Z. Chen, H. Chen, S. J. Bao, B. Shen and Y. Li, *Adv. Funct. Mater.*, 2018, **28**, 1704443.
- 233 J. He, Y. Chen and A. Manthiram, *Energy Environ. Sci.*, 2018, **11**, 2560–2568.
- 234 J. Song, T. Xu, M. L. Gordin, P. Zhu, D. Lv, Y. B. Jiang, Y. Chen, Y. Duan and D. Wang, *Adv. Funct. Mater.*, 2014, **24**, 1243–1250.
- 235 A. Garsuch, S. Herzog, L. Montag, A. Krebs and K. Leitner, *ECS Electrochem. Lett.*, 2012, **1**, A24–A26.
- 236 M. S. Whittingham and J. A. Panella, *Mater. Res. Bull.*, 1981, **16**, 37–45.
- 237 M. S. Whittingham, *Chem. Rev.*, 2004, **104**, 4271–4302.
- 238 Y.-S. Su and A. Manthiram, *J. Power Sources*, 2014, **270**, 101–105.
- 239 L. Ma, S. Wei, H. L. Zhuang, K. E. Hendrickson, R. G. Hennig and L. A. Archer, *J. Mater. Chem. A*, 2015, **3**, 19857–19866.
- 240 T. Matsuyama, A. Hayashi, C. J. Hart, L. F. Nazar and M. Tatsumisago, *J. Electrochem. Soc.*, 2016, **163**, A1730–A1735.
- 241 H. Lin, L. Yang, X. Jiang, G. Li, T. Zhang, Q. Yao, G. W. Zheng and J. Y. Lee, *Energy Environ. Sci.*, 2017, **10**, 1476–1486.
- 242 Z. Li, S. Deng, R. Xu, L. Wei, X. Su and M. Wu, *Electrochim. Acta*, 2017, **252**, 200–207.
- 243 P. Guo, D. Liu, Z. Liu, X. Shang, Q. Liu and D. He, *Electrochim. Acta*, 2017, **256**, 28–36.
- 244 F. Sun, H. Tang, B. Zhang, X. Li, C. Yin, Z. Yue, L. Zhou, Y. Li and J. Shi, *ACS Sustainable Chem. Eng.*, 2018, **6**, 974–982.
- 245 L. Yan, N. Luo, W. Kong, S. Luo, H. Wu, K. Jiang, Q. Li, S. Fan, W. Duan and J. Wang, *J. Power Sources*, 2018, **389**, 169–177.
- 246 P. T. Dirlam, J. Park, A. G. Simmonds, K. Domanik, C. B. Arrington, J. L. Schaefer, V. P. Oleshko, T. S. Kleine, K. Char, R. S. Glass, C. L. Soles, C. Kim, N. Pinna, Y.-E. Sung and J. Pyun, *ACS Appl. Mater. Interfaces*, 2016, **8**, 13437–13448.
- 247 Z. A. Ghazi, X. He, A. M. Khattak, N. A. Khan, B. Liang, A. Iqbal, J. Wang, H. Sin, L. Li and Z. Tang, *Adv. Mater.*, 2017, **29**, 1606817.
- 248 M. Li, J. Zhou, J. Zhou, C. Guo, Y. Han, Y. Zhu, G. Wang and Y. Qian, *Mater. Res. Bull.*, 2017, **96**, 509–515.
- 249 X. Li, L. Chu, Y. Wang and L. Pan, *Mater. Sci. Eng., B*, 2016, **205**, 46–54.
- 250 S. S. Zhang and D. T. Tran, *J. Mater. Chem. A*, 2016, **4**, 4371–4374.
- 251 Z. Liu, X. Zheng, S.-l. Luo, S.-q. Xu, N.-y. Yuan and J.-n. Ding, *J. Mater. Chem. A*, 2016, **4**, 13395–13399.
- 252 M. Lao, G. Zhao, X. Li, Y. Chen, S. X. Dou and W. Sun, *ACS Appl. Energy Mater.*, 2018, **1**, 167–172.
- 253 Z. Xiao, Z. Yang, L. Zhang, H. Pan and R. Wang, *ACS Nano*, 2017, **11**, 8488–8498.
- 254 J. Park, B. C. Yu, J. S. Park, J. W. Choi, C. Kim, Y. E. Sung and J. B. Goodenough, *Adv. Energy Mater.*, 2017, **7**, 1602567.
- 255 J. D. Liu, X. S. Zheng, Z. F. Shi and S. Q. Zhang, *Ionics*, 2014, **20**, 659–664.
- 256 Z. Cheng, Z. Xiao, H. Pan, S. Wang and R. Wang, *Adv. Energy Mater.*, 2017, **8**, 1702337.
- 257 X. Zhu, W. Zhao, Y. Song, Q. Li, F. Ding, J. Sun, L. Zhang and Z. Liu, *Adv. Energy Mater.*, 2018, **8**, 1800201.
- 258 L. Chen, J.-D. Liu and S.-Q. Zhang, *J. Inorg. Mater.*, 2013, **28**, 1127–1131.
- 259 H. J. Peng, G. Zhang, X. Chen, Z. W. Zhang, W. T. Xu, J. Q. Huang and Q. Zhang, *Angew. Chem., Int. Ed.*, 2016, **55**, 12990–12995.
- 260 B. Cao, Y. Chen, D. Li, L. Yin and Y. Mo, *ChemSusChem*, 2016, **9**, 3338–3344.
- 261 H. Al Salem, V. R. Chitturi, G. Babu, J. A. Santana, D. Gopalakrishnan and L. M. R. Arava, *RSC Adv.*, 2016, **6**, 110301–110306.
- 262 F. Zhou, L. T. Song, L. L. Lu, H. B. Yao and S. H. Yu, *ChemNanoMat*, 2016, **2**, 937–941.
- 263 H. Huang, J. Liu, Y. Xia, C. Cheng, C. Liang, Y. Gan, J. Zhang, X. Tao and W. Zhang, *J. Alloys Compd.*, 2017, **706**, 227–233.
- 264 T. Zhou, Y. Zhao, G. Zhou, W. Lv, P. Sun, F. Kang, B. Li and Q.-H. Yang, *Nano Energy*, 2017, **39**, 291–296.
- 265 F. Zhou, Z. Li, X. Luo, T. Wu, B. Jiang, L.-L. Lu, H.-B. Yao, M. Antonietti and S.-H. Yu, *Nano Lett.*, 2018, **18**, 1035–1043.
- 266 J. Choi, T.-G. Jeong, B. W. Cho, Y. Jung, S. H. Oh and Y.-T. Kim, *J. Phys. Chem. C*, 2018, **122**, 7664–7669.
- 267 W. Cai, G. Li, K. Zhang, G. Xiao, C. Wang, K. Ye, Z. Chen, Y. Zhu and Y. Qian, *Adv. Funct. Mater.*, 2018, **28**, 1704865.
- 268 B. Anasori, M. R. Lukatskaya and Y. Gogotsi, *Nat. Rev. Mater.*, 2017, **2**, 16098.
- 269 M. Alhabeb, K. Maleski, B. Anasori, P. Lelyukh, L. Clark, S. Sin and Y. Gogotsi, *Chem. Mater.*, 2017, **29**, 7633–7644.
- 270 X. Liang, A. Garsuch and L. F. Nazar, *Angew. Chem., Int. Ed.*, 2015, **54**, 3907–3911.
- 271 W. Bao, D. Su, W. Zhang, X. Guo and G. Wang, *Adv. Funct. Mater.*, 2016, **26**, 8746–8756.
- 272 W. Bao, L. Liu, C. Wang, S. Choi, D. Wang and G. Wang, *Adv. Energy Mater.*, 2018, **8**, 1702485.
- 273 W. Bao, X. Xie, J. Xu, X. Guo, J. Song, W. Wu, D. Su and G. Wang, *Chem.-Eur. J.*, 2017, **23**, 12613–12619.
- 274 X. Liang, Y. Rangom, C. Y. Kwok, Q. Pang and L. F. Nazar, *Adv. Mater.*, 2017, **29**, 1603040.



- 275 C. Lin, W. Zhang, L. Wang, Z. Wang, W. Zhao, W. Duan, Z. Zhao, B. Liu and J. Jin, *J. Mater. Chem. A*, 2016, **4**, 5993–5998.
- 276 J. Song, D. Su, X. Xie, X. Guo, W. Bao, G. Shao and G. Wang, *ACS Appl. Mater. Interfaces*, 2016, **8**, 29427–29433.
- 277 Y. Dong, S. Zheng, J. Qin, X. Zhao, H. Shi, X. Wang, J. Chen and Z.-S. Wu, *ACS Nano*, 2018, **12**, 2381–2388.
- 278 D. Rao, L. Zhang, Y. Wang, Z. Meng, X. Qian, J. Liu, X. Shen, G. Qiao and R. Lu, *J. Phys. Chem. C*, 2017, **121**, 11047–11054.
- 279 E. S. Sim, G. S. Yi, M. Je, Y. Lee and Y.-C. Chung, *J. Power Sources*, 2017, **342**, 64–69.
- 280 E. S. Sim and Y.-C. Chung, *Appl. Surf. Sci.*, 2018, **435**, 210–215.
- 281 Y. Zhao and J. Zhao, *Appl. Surf. Sci.*, 2017, **412**, 591–598.
- 282 X. Liu, X. Shao, F. Li and M. Zhao, *Appl. Surf. Sci.*, 2018, **455**, 522–526.
- 283 N. Mosavati, V. R. Chitturi, S. O. Salley and K. S. Ng, *J. Power Sources*, 2016, **321**, 87–93.
- 284 Z. Cui, C. Zu, W. Zhou, A. Manthiram and J. B. Goodenough, *Adv. Mater.*, 2016, **28**, 6926–6931.
- 285 D.-R. Deng, T.-H. An, Y.-J. Li, Q.-H. Wu, M.-S. Zheng and Q.-F. Dong, *J. Mater. Chem. A*, 2016, **4**, 16184–16190.
- 286 Z. Hao, L. Yuan, C. Chen, J. Xiang, Y. Li, Z. Huang, P. Hu and Y. Huang, *J. Mater. Chem. A*, 2016, **4**, 17711–17717.
- 287 D.-R. Deng, J. Lei, F. Xue, C.-D. Bai, X.-D. Lin, J.-C. Ye, M.-S. Zheng and Q.-F. Dong, *J. Mater. Chem. A*, 2017, **5**, 23497–23505.
- 288 T.-G. Jeong, D. S. Choi, H. Song, J. Choi, S.-A. Park, S. H. Oh, H. Kim, Y. Jung and Y.-T. Kim, *ACS Energy Lett.*, 2017, **2**, 327–333.
- 289 J. Zhang, C. You, W. Zhang, J. Wang, S. Guo, R. Yang and Y. Xu, *Electrochim. Acta*, 2017, **250**, 159–166.
- 290 T. Zhou, W. Lv, J. Li, G. Zhou, Y. Zhao, S. Fan, B. Liu, B. Li, F. Kang and Q.-H. Yang, *Energy Environ. Sci.*, 2017, **10**, 1694–1703.
- 291 X. He, Y. Shuai, L. Na, K. Chen, Y. Zhang, Z. Zhang and F. Gan, *Mater. Lett.*, 2018, **215**, 91–94.
- 292 W. Zeng, Z. Wang, M. M.-C. Cheng and K. S. Ng, *J. Electrochem. Soc.*, 2018, **165**, A1011–A1018.
- 293 L. Chen, W. Yang, H. Zhang, J. Liu and Y. Zhou, *J. Mater. Sci.*, 2018, **53**, 10363–10371.
- 294 Y. Wang, R. Zhang, Y.-C. Pang, X. Chen, J. Lang, J. Xu, C. Xiao, H. Li, K. Xi and S. Ding, *Energy Storage Mater.*, 2018, **16**, 228–235.
- 295 Z. Sun, J. Zhang, L. Yin, G. Hu, R. Fang, H.-M. Cheng and F. Li, *Nat. Commun.*, 2017, **8**, 14627.
- 296 N. Mosavati, S. O. Salley and K. S. Ng, *J. Power Sources*, 2017, **340**, 210–216.
- 297 X. Li, K. Ding, B. Gao, Q. Li, Y. Li, J. Fu, X. Zhang, P. K. Chu and K. Huo, *Nano Energy*, 2017, **40**, 655–662.
- 298 L. Ma, H. Yuan, W. Zhang, G. Zhu, Y. Wang, Y. Hu, P. Zhao, R. Chen, T. Chen and J. Liu, *Nano Lett.*, 2017, **17**, 7839–7846.
- 299 W. Ren, L. Xu, L. Zhu, X. Wang, X. Ma and D. Wang, *ACS Appl. Mater. Interfaces*, 2018, **10**, 11642–11651.
- 300 Y. Zhong, D. Chao, S. Deng, J. Zhan, R. Fang, Y. Xia, Y. Wang, X. Wang, X. Xia and J. Tu, *Adv. Funct. Mater.*, 2018, **28**, 1706391.
- 301 L. Zhu, C. Li, W. Ren, M. Qin and L. Xu, *New J. Chem.*, 2018, **42**, 5109–5116.
- 302 D.-R. Deng, F. Xue, Y.-J. Jia, J.-C. Ye, C.-D. Bai, M.-S. Zheng and Q.-F. Dong, *ACS Nano*, 2017, **11**, 6031–6039.
- 303 S. R. Batten, N. R. Champness, X.-M. Chen, J. Garcia-Martinez, S. Kitagawa, L. Öhrström, M. O’Keeffe, M. P. Suh and J. Reedijk, *Pure Appl. Chem.*, 2013, **85**, 1715–1724.
- 304 R. Demir-Cakan, M. Morcrette, F. Nouar, C. Davoisne, T. Devic, D. Gonbeau, R. Dominko, C. Serre, G. Férey and J.-M. Tarascon, *J. Am. Chem. Soc.*, 2011, **133**, 16154–16160.
- 305 Z. Wang, X. Li, Y. Cui, Y. Yang, H. Pan, Z. Wang, C. Wu, B. Chen and G. Qian, *Cryst. Growth Des.*, 2013, **13**, 5116–5120.
- 306 J. Zheng, J. Tian, D. Wu, M. Gu, W. Xu, C. Wang, F. Gao, M. H. Engelhard, J.-G. Zhang, J. Liu and J. Xiao, *Nano Lett.*, 2014, **14**, 2345–2352.
- 307 Z. Wang, B. Wang, Y. Yang, Y. Cui, Z. Wang, B. Chen and G. Qian, *ACS Appl. Mater. Interfaces*, 2015, **7**, 20999–21004.
- 308 X.-J. Hong, T.-X. Tan, Y.-K. Guo, X.-Y. Tang, J.-Y. Wang, W. Qin and Y.-P. Cai, *Nanoscale*, 2018, **10**, 2774–2780.
- 309 J. Xu, T. Lawson, H. Fan, D. Su and G. Wang, *Adv. Energy Mater.*, 2018, **8**, 1702607.
- 310 J. H. Park, K. M. Choi, D. K. Lee, B. C. Moon, S. R. Shin, M.-K. Song and J. K. Kang, *Sci. Rep.*, 2016, **6**, 25555.
- 311 P. Chiochan, S. Kaewruang, N. Phattharasupakun, J. Wutthiprom, T. Maihom, J. Limtrakul, S. S. Nagarkar, S. Horike and M. Sawangphruk, *Sci. Rep.*, 2017, **7**, 17703.
- 312 J. Zhou, R. Li, X. Fan, Y. Chen, R. Han, W. Li, J. Zheng, B. Wang and X. Li, *Energy Environ. Sci.*, 2014, **7**, 2715–2724.
- 313 Y. Mao, G. Li, Y. Guo, Z. Li, C. Liang, X. Peng and Z. Lin, *Nat. Commun.*, 2017, **8**, 14628.
- 314 L. Bai, D. Chao, P. Xing, L. J. Tou, Z. Chen, A. Jana, Z. X. Shen and Y. Zhao, *ACS Appl. Mater. Interfaces*, 2016, **8**, 14328–14333.
- 315 Z. Wang, Z. Dou, Y. Cui, Y. Yang, Z. Wang and G. Qian, *Microporous Mesoporous Mater.*, 2014, **185**, 92–96.
- 316 Y. Yue, B. Guo, Z.-A. Qiao, P. F. Fulvio, J. Chen, A. J. Binder, C. Tian and S. Dai, *Microporous Mesoporous Mater.*, 2014, **198**, 139–143.
- 317 P. M. Shanthi, P. J. Hanumantha, B. Gattu, M. Sweeney, M. K. Datta and P. N. Kumta, *Electrochim. Acta*, 2017, **229**, 208–218.
- 318 Y. Hou, H. Mao and L. Xu, *Nano Res.*, 2017, **10**, 344–353.
- 319 Y.-C. Lu, Q. He and H. A. Gasteiger, *J. Phys. Chem. C*, 2014, **118**, 5733–5741.
- 320 J. Zhou, X. Yu, X. Fan, X. Wang, H. Li, Y. Zhang, W. Li, J. Zheng, B. Wang and X. Li, *J. Mater. Chem. A*, 2015, **3**, 8272–8275.
- 321 M.-T. Li, Y. Sun, K.-S. Zhao, Z. Wang, X.-L. Wang, Z.-M. Su and H.-M. Xie, *ACS Appl. Mater. Interfaces*, 2016, **8**, 33183–33188.



- 322 A. E. Baumann, G. E. Aversa, A. Roy, M. L. Falk, N. M. Bedford and V. S. Thoi, *J. Mater. Chem. A*, 2018, **6**, 4811–4821.
- 323 H. Park and D. J. Siegel, *Chem. Mater.*, 2017, **29**, 4932–4939.
- 324 D. Su, M. Cortie, H. Fan and G. Wang, *Adv. Mater.*, 2017, **29**, 1700587.
- 325 Z. Zhang, Y. Wang, J. Liu, D. Sun, X. Ma, Y. Jin and Y. Cui, *Electrochim. Acta*, 2018, **271**, 58–66.
- 326 S. Bai, X. Liu, K. Zhu, S. Wu and H. Zhou, *Nat. Energy*, 2016, **1**, 16094.
- 327 H. Zhang, C. Lin, X. Hu, B. Zhu and D. Yu, *ACS Appl. Mater. Interfaces*, 2018, **10**, 12708–12715.
- 328 Q. Shi, Z. Chen, Z. Song, J. Li and J. Dong, *Angew. Chem., Int. Ed.*, 2011, **50**, 672–675.
- 329 Z. Zhao, X. Ma, A. Kasik, Z. Li and Y. S. Lin, *Ind. Eng. Chem. Res.*, 2013, **52**, 1102–1108.
- 330 T. Loiseau, C. Serre, C. Huguenard, G. Fink, F. Taulelle, M. Henry, T. Bataille and G. Férey, *Chem.–Eur. J.*, 2004, **10**, 1373–1382.
- 331 T. R. C. Van Assche, T. Duerinck, S. Van der Perre, G. V. Baron and J. F. M. Denayer, *Langmuir*, 2014, **30**, 7878–7883.
- 332 Z. Zhao, S. Wang, R. Liang, Z. Li, Z. Shi and G. Chen, *J. Mater. Chem. A*, 2014, **2**, 13509–13512.
- 333 W.-W. Jin, H.-J. Li, J.-Z. Zou, S.-Z. Zeng, Q.-D. Li, G.-Z. Xu, H.-C. Sheng, B.-B. Wang, Y.-H. Si, L. Yu and X.-R. Zeng, *RSC Adv.*, 2018, **8**, 4786–4793.
- 334 X.-C. Liu, Y. Yang, J. Wu, M. Liu, S. P. Zhou, B. D. A. Levin, X.-D. Zhou, H. Cong, D. A. Muller, P. M. Ajayan, H. D. Abruña and F.-S. Ke, *ACS Energy Lett.*, 2018, **3**, 1325–1330.
- 335 J. Linnemann, L. Taudien, M. Klose and L. Giebeler, *J. Mater. Chem. A*, 2017, **5**, 18420–18428.
- 336 S. Aguado, J. Canivet and D. Farrusseng, *J. Mater. Chem.*, 2011, **21**, 7582–7588.
- 337 G. Babu, K. Ababtain, K. Y. S. Ng and L. M. R. Arava, *Sci. Rep.*, 2015, **5**, 8763.
- 338 H. Tang, S. Yao, M. Jing, X. Wu, J. Hou, X. Qian, D. Rao, X. Shen, X. Xi and K. Xiao, *Electrochim. Acta*, 2015, **176**, 442–447.
- 339 H. Al Salem, G. Babu, C. V. Rao and L. M. R. Arava, *J. Am. Chem. Soc.*, 2015, **137**, 11542–11545.
- 340 R. Fang, S. Zhao, S. Pei, Y. Cheng, P. Hou, M. Liu, H.-M. Cheng, C. Liu and F. Li, *Carbon*, 2016, **109**, 719–726.
- 341 J. He, Y. Chen, W. Lv, K. Wen, C. Xu, W. Zhang, Y. Li, W. Qin and W. He, *ACS Nano*, 2016, **10**, 10981–10987.
- 342 Y.-J. Li, J.-M. Fan, M.-S. Zheng and Q.-F. Dong, *Energy Environ. Sci.*, 2016, **9**, 1998–2004.
- 343 Z. Li, C. Li, X. Ge, J. Ma, Z. Zhang, Q. Li, C. Wang and L. Yin, *Nano Energy*, 2016, **23**, 15–26.
- 344 M. Zhang, C. Yu, C. Zhao, X. Song, X. Han, S. Liu, C. Hao and J. Qiu, *Energy Storage Mater.*, 2016, **5**, 223–229.
- 345 Y. Li, J. Fan, J. Zhang, J. Yang, R. Yuan, J. Chang, M. Zheng and Q. Dong, *ACS Nano*, 2017, **11**, 11417–11424.
- 346 D. Xiao, Q. Li, H. Zhang, Y. Ma, C. Lu, C. Chen, Y. Liu and S. Yuan, *J. Mater. Chem. A*, 2017, **5**, 24901–24908.
- 347 N. K. Thangavel, D. Gopalakrishnan and L. M. R. Arava, *J. Phys. Chem. C*, 2017, **121**, 12718–12725.
- 348 Z. Lin, X. Li, W. Huang, X. Zhu, Y. Wang and Z. Shan, *ChemElectroChem*, 2017, **4**, 2577–2582.
- 349 P. Zuo, J. Hua, M. He, H. Zhang, Z. Qian, Y. Ma, C. Du, X. Cheng, Y. Gao and G. Yin, *J. Mater. Chem. A*, 2017, **5**, 10936–10945.
- 350 G. Chen, X. Song, S. Wang, Y. Wang, T. Gao, L.-X. Ding and H. Wang, *J. Membr. Sci.*, 2018, **548**, 247–253.
- 351 S. Liu, J. Li, X. Yan, Q. Su, Y. Lu, J. Qiu, Z. Wang, X. Lin, J. Huang, R. Liu, B. Zheng, L. Chen, R. Fu and D. Wu, *Adv. Mater.*, 2018, **30**, 1706895.
- 352 M.-e. Zhong, J. Guan, Q. Feng, X. Wu, Z. Xiao, W. Zhang, S. Tong, N. Zhou and D. Gong, *Carbon*, 2018, **128**, 86–96.
- 353 C.-Y. Fan, P. Xiao, H.-H. Li, H.-F. Wang, L.-L. Zhang, H.-Z. Sun, X.-L. Wu, H.-M. Xie and J.-P. Zhang, *ACS Appl. Mater. Interfaces*, 2015, **7**, 27959–27967.
- 354 X. Yao, J. Xu, Z. Hong, G. Li, X. Wang, F. Lu, W. Wang, H. Liu, C. Liang, Z. Lin and W. Wang, *J. Phys. Chem. C*, 2018, **122**, 3263–3272.
- 355 K. Xu, X. Liu, J. Liang, J. Cai, K. Zhang, Y. Lu, X. Wu, M. Zhu, Y. Liu, Y. Zhu, G. Wang and Y. Qian, *ACS Energy Lett.*, 2018, **3**, 420–427.
- 356 L. Luo, S.-H. Chung, C.-H. Chang and A. Manthiram, *J. Mater. Chem. A*, 2017, **5**, 15002–15007.
- 357 Q. Zhao, X. Hu, K. Zhang, N. Zhang, Y. Hu and J. Chen, *Nano Lett.*, 2015, **15**, 721–726.
- 358 X. Zhu, J. Tian, X. Liu, W. Huang, D. Luo, Z. Wang and Z. Shan, *RSC Adv.*, 2017, **7**, 35482–35489.
- 359 Ş. Sörgel, O. Kesten, A. Wengel and T. Sörgel, *Energy Storage Mater.*, 2018, **10**, 223–232.
- 360 J. H. Yom, S. M. Cho, S. W. Hwang and W. Y. Yoon, *J. Electrochem. Soc.*, 2016, **163**, A2179–A2184.
- 361 Y. J. Hong, K. C. Roh and Y. C. Kang, *Carbon*, 2018, **126**, 394–403.
- 362 S. Zheng, F. Yi, Z. Li, Y. Zhu, Y. Xu, C. Luo, J. Yang and C. Wang, *Adv. Funct. Mater.*, 2014, **24**, 4156–4163.
- 363 J. Zhang, H. Li, Q. Tang, P. Bai, Y. Pan and Z. Lin, *RSC Adv.*, 2016, **6**, 114447–114452.
- 364 J. Xiao, *Adv. Energy Mater.*, 2015, **5**, 1501102.
- 365 C. Barchasz, F. Mesguich, J. Dijon, J.-C. Leprêtre, S. Patoux and F. Alloin, *J. Power Sources*, 2012, **211**, 19–26.
- 366 S.-H. Chung and A. Manthiram, *Electrochim. Acta*, 2013, **107**, 569–576.
- 367 K. Zhang, F. Qin, J. Fang, Q. Li, M. Jia, Y. Lai, Z. Zhang and J. Li, *J. Solid State Electrochem.*, 2014, **18**, 1025–1029.
- 368 X.-B. Cheng, H.-J. Peng, J.-Q. Huang, L. Zhu, S.-H. Yang, Y. Liu, H.-W. Zhang, W. Zhu, F. Wei and Q. Zhang, *J. Power Sources*, 2014, **261**, 264–270.
- 369 J. X. Zhang, Z. S. Ma, J. J. Cheng, Y. Wang, C. Wu, Y. Pan and C. Lu, *J. Electroanal. Chem.*, 2015, **738**, 184–187.
- 370 I. Raguzin, S. Choudhury, F. Simon, M. Stamm and L. Ionov, *Adv. Mater. Interfaces*, 2017, **4**, 1600811.
- 371 J. J. Cheng, J. T. Zhu, Y. Pan, Z. S. Ma, H. J. Song, J. A. Pan, Z. Z. Li and C. Lu, *ECS Electrochem. Lett.*, 2015, **4**, A19–A21.
- 372 L.-J. Liu, Y. Chen, Z.-F. Zhang, X.-L. You, M. D. Walle, Y.-J. Li and Y.-N. Liu, *J. Power Sources*, 2016, **325**, 301–305.





- 373 J. Hassoun, M. Agostini, A. Latini, S. Panero, Y.-K. Sun and B. Scrosati, *J. Electrochem. Soc.*, 2012, **159**, A390–A395.
- 374 Z. Liu, X. Zheng, N.-Y. Yuan and J.-N. Ding, *J. Mater. Chem. A*, 2017, **5**, 942–946.
- 375 X. Wu, S. Yao, J. Hou, M. Jing, X. Qian, X. Shen, J. Xiang and X. Xi, *J. Nanosci. Nanotechnol.*, 2017, **17**, 2482–2487.
- 376 P. Zuo, H. Zhang, M. He, Q. Li, Y. Ma, C. Du, X. Cheng, H. Huo, Y. Gao and G. Yin, *Carbon*, 2017, **122**, 635–642.
- 377 N. Mosavati, V. R. Chitturi, L. M. R. Arava, S. O. Salley and K. Y. S. Ng, *Electrochim. Acta*, 2015, **185**, 297–303.
- 378 Z. Zhang, L. L. Kong, S. Liu, G. R. Li and X. P. Gao, *Adv. Energy Mater.*, 2017, **7**, 1602543.
- 379 S.-K. Park, J.-K. Lee and Y. C. Kang, *Adv. Funct. Mater.*, 2017, **28**, 1705264.
- 380 Y.-Q. Lu, Y.-J. Wu, T. Sheng, X.-X. Peng, Z.-G. Gao, S.-J. Zhang, L. Deng, R. Nie, J. Światowska, J.-T. Li, Y. Zhou, L. Huang, X.-D. Zhou and S.-G. Sun, *ACS Appl. Mater. Interfaces*, 2018, **10**, 13499–13508.
- 381 H. Yu, B. Zhang, F. Sun, G. Jiang, N. Zheng, C. Xu and Y. Li, *Appl. Surf. Sci.*, 2018, **450**, 364–371.
- 382 W. Hu, Y. Hirota, Y. Zhu, N. Yoshida, M. Miyamoto, T. Zheng and N. Nishiyama, *ChemSusChem*, 2017, **10**, 3557–3564.
- 383 J. Wang, T. Wu, S. Zhang, S. Gu, J. Jin and Z. Wen, *Chem. Eng. J.*, 2018, **334**, 2356–2362.
- 384 R. Banerjee, A. Phan, B. Wang, C. Knobler, H. Furukawa, M. O'Keeffe and O. M. Yaghi, *Science*, 2008, **319**, 939–943.
- 385 X. Tao, F. Chen, Y. Xia, H. Huang, Y. Gan, X. Chen and W. Zhang, *Chem. Commun.*, 2013, **49**, 4513–4515.
- 386 J. Zhang, H. Li, Z. Lin, Q. Tang, W. Qi, L. Wang, H. Zheng and K. Zhou, *RSC Adv.*, 2017, **7**, 39172–39177.
- 387 X. Song, S. Wang, G. Chen, T. Gao, Y. Bao, L.-X. Ding and H. Wang, *Chem. Eng. J.*, 2018, **333**, 564–571.
- 388 X. Li, J. Liang, K. Zhang, Z. Hou, W. Zhang, Y. Zhu and Y. Qian, *Energy Environ. Sci.*, 2015, **8**, 3181–3186.
- 389 Z. Gao, Y. Schwab, Y. Zhang, N. Song and X. Li, *Adv. Funct. Mater.*, 2018, **28**, 1800563.
- 390 X.-Q. Niu, X.-L. Wang, D.-H. Wang, Y. Li, Y.-J. Zhang, Y.-D. Zhang, T. Yang, T. Yu and J.-P. Tu, *J. Mater. Chem. A*, 2015, **3**, 17106–17112.
- 391 X.-Q. Niu, X.-L. Wang, D. Xie, D.-H. Wang, Y.-D. Zhang, Y. Li, T. Yu and J.-P. Tu, *ACS Appl. Mater. Interfaces*, 2015, **7**, 16715–16722.
- 392 S. Gope and A. J. Bhattacharyya, *ACS Appl. Energy Mater.*, 2018, **1**, 2942–2954.
- 393 C. Dai, L. Hu, M.-Q. Wang, Y. Chen, J. Han, J. Jiang, Y. Zhang, B. Shen, Y. Niu, S.-J. Bao and M. Xu, *Energy Storage Mater.*, 2017, **8**, 202–208.
- 394 J. Jiang, J. Zhu, W. Ai, X. Wang, Y. Wang, C. Zou, W. Huang and T. Yu, *Nat. Commun.*, 2015, **6**, 8622.
- 395 J. Zhang, H. Hu, Z. Li and X. W. Lou, *Angew. Chem., Int. Ed.*, 2016, **55**, 3982–3986.
- 396 H.-J. Peng, Z.-W. Zhang, J.-Q. Huang, G. Zhang, J. Xie, W.-T. Xu, J.-L. Shi, X. Chen, X.-B. Cheng and Q. Zhang, *Adv. Mater.*, 2016, **28**, 9551–9558.
- 397 L. Kong, H.-J. Peng, J.-Q. Huang, W. Zhu, G. Zhang, Z.-W. Zhang, P.-Y. Zhai, P. Sun, J. Xie and Q. Zhang, *Energy Storage Mater.*, 2017, **8**, 153–160.

